MICROCOPY RESOLUTION TEST CHART
NATIONAL BUREAU OF STANDARDS-1963-A

AR○ 21187.3-EC

AD-A184 335

Investigation of Hexagonal Ferrite Film Growth Techniques for Millimeter-Wave Systems Applications,

W. E. Kramer, K. C. Yoo, and R. H. Hopkins
Crystal Science Technology

March 2, 1987

Westinghouse Research and Development Center
1310 Beulah Road, Pgh., PA 15235

SEP 1 1 1937

87 9 9 131

Investigation of Hexagonal Ferrite Film Growth Techniques for Millimeter-Wave Systems Applications

W. E. Kramer, K. C. Yoo, and R. H. Hopkins
Crystal Science Technology

March 2, 1987

Westinghouse Research and Development Center
1310 Beulah Road, Pgh., PA 15235

REPORT DOCUMENTATION PAGE

1a. REPORT SECURITY CLASSIFICATION Unclassified	1b. RESTRICTIVE MARKINGS
2a SECURITY CLASSIFICATION AUTHORITY	3 DISTRIBUTION / AVAILABILITY OF REPORT Approved for public release; distribution unlimited.
2b. DECLASSIFICATION / DOWNGRADING SCHEDULE	

4 PERFORMING ORGANIZATION REPORT NUMBER(S) 87-9F4-HEXAF-R1	5 MONITORING ORGANIZATION REPORT NUMBER(S) ARO 21187.3-EL

6a. NAME OF PERFORMING ORGANIZATION Westinghouse Electric Corp. Research & Development Center	6b OFFICE SYMBOL (If applicable)	7a. NAME OF MONITORING ORGANIZATION U. S. Army Research Office
6c. ADDRESS (City, State, and ZIP Code) 1310 Beulah Road Pittsburgh, PA 15235		7b. ADDRESS (City, State, and ZIP Code) P. O. Box 12211 Research Triangle Park, NC 27709-2211

8a. NAME OF FUNDING / SPONSORING ORGANIZATION U. S. Army Research Office	8b. OFFICE SYMBOL (If applicable)	9. PROCUREMENT INSTRUMENT IDENTIFICATION NUMBER DAAG29-84-C-0012

8c ADDRESS (City, State, and ZIP Code) P. O. Box 12211 Research Triangle Park, NC 27709-2211	10. SOURCE OF FUNDING NUMBERS			
	PROGRAM ELEMENT NO	PROJECT NO.	TASK NO.	WORK UNIT ACCESSION NO

11 TITLE (Include Security Classification)   *Use cover / title page*

12 PERSONAL AUTHOR(S)

Kramer, William; Yoo, Kee-Chang; Kun, Zoltan; Hopkins, Richard; Daniel, Michael; Adam, Douglas

13a. TYPE OF REPORT Final	13b. TIME COVERED FROM 6/85 TO 1/87	14. DATE OF REPORT (Year, Month, Day) 87 March 15	15 PAGE COUNT

16 SUPPLEMENTARY NOTATION

The view, opinions and/or findings contained in this report are those of the author(s) and should not be construed as an official Department of the Army position, policy, or decision, unless so designated by other documentation.

17	COSATI CODES		18. SUBJECT TERMS (Continue on reverse if necessary and identify by block number)
FIELD	GROUP	SUB-GROUP	hexaferrites, epitaxy, film, substrate, flux, mm-wave, magnetic resonance, crystal, flux, growth, lattice match

19 ABSTRACT (Continue on reverse if necessary and identify by block number)

During this program we surveyed a number of new substrate and solvent solution systems for epitaxial ferrite growth. The growth of single crystals of two new materials, cobalt gallate and Ta-substituted barium vanadate, was successfully demonstrated. Compositions lattice-matched to the ferrites were demonstrated, and ferrite films were grown on cobalt gallate. Interdiffusion of barium hexaferrite and barium vanadate prevented high-quality hexaferrite film growth on the latter substrate.

20 DISTRIBUTION / AVAILABILITY OF ABSTRACT ☐ UNCLASSIFIED/UNLIMITED ☐ SAME AS RPT ☐ DTIC USERS	21 ABSTRACT SECURITY CLASSIFICATION Unclassified
22a NAME OF RESPONSIBLE INDIVIDUAL Dr. John Zavada	22b TELEPHONE (Include Area Code) 22c OFFICE SYMBOL

CONTENTS

$A1$

LIST OF FIGURES

LIST OF TABLES

ABSTRACT

Hexagonal ferrites—magnetic insulators with large anisotropy
fields and $4\pi M$ values—are extremely attractive candidates for mm-wave
devices such as circulators, phase shifters, tunable filters, and oscil-
lators. The application of these materials in thin film form has been
hindered by the lack of lattice-matched substrate materials for film
growth and because the epitaxy process itself is only partially under-
stood. The objectives of this program were to develop improved
substrate materials and a more detailed knowledge of conditions favoring
epitaxial growth of hexagonal ferrites.

During this program we surveyed a number of new substrate and
solvent solution systems for epitaxial ferrite growth. The growth of
single crystals of two new materials, cobalt gallate and Ta-substituted
barium vanadate, was successfully demonstrated. Compositions lattice-
matched to the ferrites were demonstrated, and ferrite films were grown
on cobalt gallate. Interdiffusion of barium hexaferrite and barium
vanadate prevented high-quality hexaferrite film growth on the latter
substrate.

A new ternary flux for barium hexaferrite film growth, Bi_2O_3-
BaO-B_2O_3, was identified. Liquidus curves were developed for the BaO-
Ba_2O_3 join and for ferrite-saturated ternary solutions. Using this
flux, smooth, low defect density films of Al-doped barium hexaferrite
were grown on Mg,Zr-substituted strontium hexagallate substrates. The
lattice mismatch between the film and substrate was reduced to 0.37% and
0.36% for the $\underline{a}$ and $\underline{c}$ directions, respectively. X-ray reflection topo-
graphs for the films indicate that the lowest defect densities were
achieved for 5 to 10 μm thick layers.

FMR linewidths measured at 50 GHz indicated generally broad resonances. The lowest values were 280 Oe and 550 Oe for pure barium ferrite films grown on cobalt gallate and strontium gallate, respectively. While these values compare favorably with those in the literature, they indicate that further improvements in substrate-film matching are required to provide device-quality films. Further substrate development studies, improvements in flux-substrate compatibility, and the use of other epitaxial techniques seem warranted.

1. INTRODUCTION

1.1 OBJECTIVE

The objective of this program was to study and advance the understanding of the heteroepitaxial growth of hexagonal ferrite compounds. The approach was twofold: to synthesize lattice-matched substrate materials and to explore epitaxial growth methods which yield ferrite thin films with uniaxial anisotropy fields of up to 35 kOe and narrow resonance linewidths.

1.2 FERRITE APPLICATIONS

Today, single and poly-crystal garnet or spinel ferrites find widespread use as tunable microwave filters and resonators in applications ranging from test equipment to radar and ECM systems. They are also used as nonlinear devices (e.g., in power limiters) and are employed extensively in microwave systems—radar, satellites, communication, ECM, etc.—as circulators, isolators, and phase shifters. Increasingly, however, emphasis is being focused on the development of millimeter-wave devices for many of these applications. Systems in this frequency range have wide bandwidths and a narrow beamwidth for a given antenna size. In addition, mm-wave systems can be small in size and light in weight.

To operate close to resonance at such high frequencies in magnetic devices requires extraordinarily high magnetic fields which are extremely difficult to attain with a compact permanent magnet or electromagnet when materials like garnets with sm ll internal crystalline anisotropy fields are used.

Hexagonal ferrites with their large anisotropy fields—~17 kOe for M-type $BaFe_{12}O_{19}$, for example—offer an attractive alternative for mm-wave systems operating close to resonance with relatively small (0 to 5 kG) fields. These devices could match future needs for small, low-cost, millimeter-wave ferrite control components such as circulators, phase shifters, isolators, limiters, and switches, as well as for tunable filters and oscillators.

2. RESEARCH APPROACH

Devices using hexagonal ferrites were demonstrated more than 20 years ago; however, their systems implementation has long been hampered by difficulties in reproducibly growing high-quality crystals, and by the difficulties encountered when processing the bulk crystals into the desired device geometry [1-7]. Epitaxial hexagonal ferrite films are, however, compatible with planar transmission lines such as dielectric waveguides and allow the use of photolithography to define the ferrite device geometry.

The lack of a suitable low defect density lattice-matched single-crystal substrate has been a crucial limitation to growing smooth, chemically homogeneous hexaferrite layers [8-17]. In addition, typical flux systems are not always compatible with available substrates. Thus, two requirements must be met before hexagonal ferrites can become successful candidates for mm-wave devices in epitaxial film form: (1) improved substrate materials must be synthesized and grown as single crystals, and (2) the epitaxial growth must be better understood and perfected. Research in each of these topics formed major activities in this program. The results of the research in each follows.

3. SUBSTRATE MATERIAL STUDIES

3.1 SUBSTRATE CRITERIA

The growth of good-quality hexaferrite epitaxial films has been dominated by the search for suitable substrate materials and studies to define growth conditions which produce crystals of suitable size and quality. A survey of the pertinent literature [8-17,18,19] indicates that improvements in ferrite film quality result from improvements in the preparation of the substrate material, but that no truly lattice-matched compound has been grown as large, low defect density, single crystals. Criteria for selecting a substrate material can be summarized as follows:

- Growth of large, homogeneous, high-quality single crystals.
- Cell dimension and thermal expansion coefficient similar to those of the hexaferrite film.
- Paramagnetic or diamagnetic, and a good insulator.
- Low dielectric losses at microwave frequencies.
- Mechanically strong, and chemically and thermally stable.

The two promising approaches for substrate development were:

1. To find compounds which display lattice symmetries and interatomic distances similar to those of the hexaferrites along specific crystallographic planes, e.g., (111) of cubic spinels [8-12].

2. To find compounds with comparable lattice dimensions in crystal systems of the same material class as the hexaferrites, e.g., hexagallates [16,17,21,22]. Investigations of each approach were carried out.

The search for new substrate was guided by the known crystallographic relations between the hexaferrites and potential substrate candidates. $BaFe_{12}O_{19}$ is a prototype of the hexaferrite compounds desired as epitaxial films. It displays hexagonal symmetry with lattice dimensions $\underline{a}$ = 5.89 Å and $\underline{c}$ = 23.20 Å. The hexaferrites share a

4

crystallographic kinship with the cubic spinel family. The cubic spinels can be visualized as layers of close-packed oxygen ions stacked along the <111> cube direction (the smaller metal ions completing the structures fit in the interstices between the oxygen ions) [20]. In contrast, the hexaferrites (and their aluminum and gallium analogs) are formed by stacking the oxygen layers along the hexagonal $\underline{c}$ direction. Distributed periodically in the hexagonal structure are layers in which one-quarter of the oxygen ions are replaced by the alkaline earth atoms, for example, Ba or Sr (Figure 1).

The crystallographic relationships between the two families can be expressed as

<101> spinel parallel to <10$\bar{1}$0> hexagonal ferrite

(111) spinel parallel to (0001) hexagonal ferrite

Dwg. 7770A62
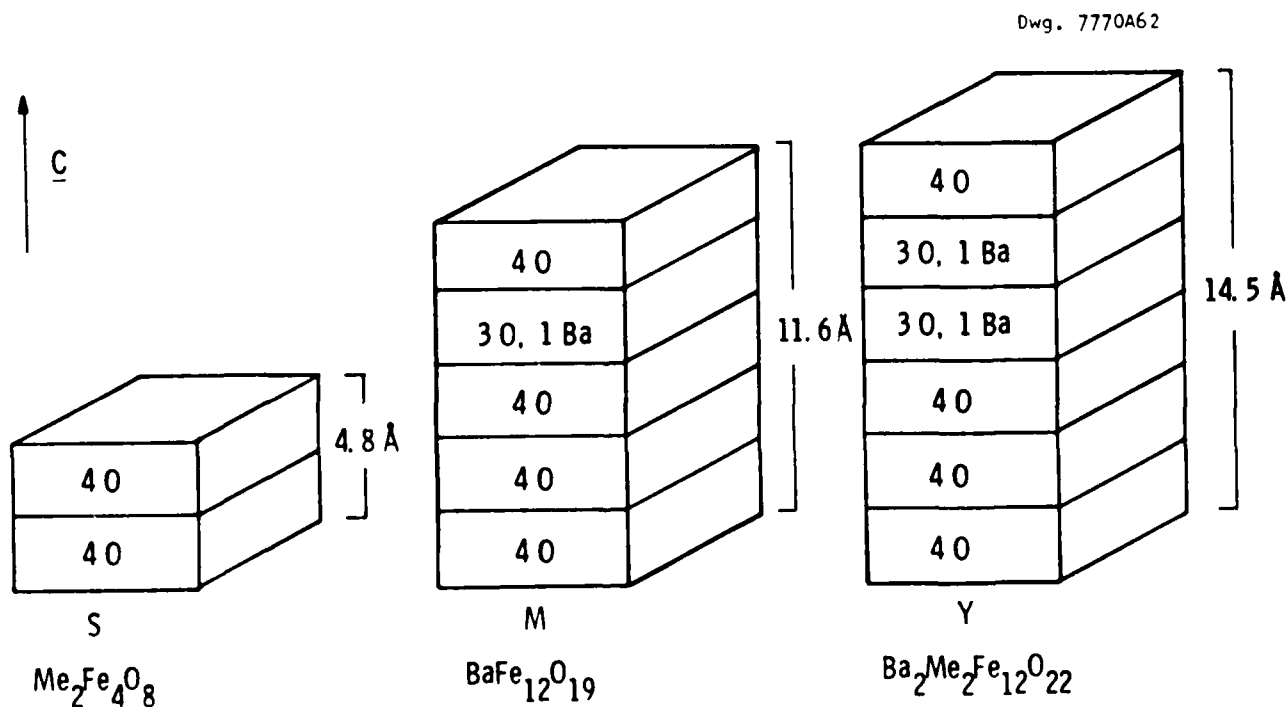
Figure 1 — Oxygen layer stacking in cubic spinel and hexagonal M and Y ferrites (after Reference 23).

5

Clearly, the nonmagnetic spinels can serve as substrates for magnetic hexaferrite layers (or vice versa) if the appropriate lattice matching between the cube face diagonal and hexagonal $\underline{a}$ dimension exists; that is, if $\underline{a}/\sqrt{2}$ spinel = $\underline{a}$ hexagonal. For barium ferrite, $\underline{a} \simeq$ 5.89 Å so that a spinel substrate with a cube edge of 8.33 Å is required. Alternatively, a nonmagnetic hexagallate or hexaluminate with $\underline{a} \simeq$ 5.89 Å would be suitable for epitaxial film growth.

Based on the above relationships, we focused our studies in two areas: (1) identification of new nonmagnetic spinel or hexagonal compounds which lattice-match barium ferrite (or lithium ferrite, also of interest for advanced device applications) and (2) extension of our previously developed YIG liquid phase epitaxial (LPE) growth techniques to ferrite films, using as test vehicles substrates which previously had been investigated by others. This step was then followed by film growth on the new substrate materials as they were identified, and the exploration of new oxide solvents which offered advantages for hexaferrite LPE over those previously reported in the literature.

3.2 SUBSTRATE MATERIAL SURVEY

A preliminary survey was conducted to identify likely compounds from which single crystals could be grown for epitaxial substrates. The survey was conducted first by searching for nonmagnetic analogs that exhibited lattice size close to that of the hexaferrites and for cubic materials displaying a cell diagonal close in size to the hexagonal $\underline{a}$ direction, as noted above.

Components of each candidate compound were weighed to stoichiometric proportions, mixed in a ball mill, and fired at a temperature compatible with solid state reaction. X-ray powder diffraction patterns of reacted samples verified both the completeness of the reaction and confirmed the crystal structure. Diffraction patterns for melted samples were employed to evaluate phase stability, structure, and cell dimension.

Table 1 is the result of the compound survey; it lists the candidate compound name, crystal structure, cell dimension, and comments

6

Table 1 — Compound Survey

Compound	Structure	Cell Dimension	Results
$ZnGa_2O_4$	Cubic-Spinel	8.33	Decomposes.
$CoGa_2O_4$	Cubic-Spinel	8.326	
$MgGa_2O_4$	Cubic-Spinel	8.28	Decomposes.
$NiGa_2O_4$	Cubic-Spinel	8.25	
$CuGa_2O_4$	Cubic-Spinel	8.39	*Too large.
$CdGa_2O_4$	Cubic-Spinel	8.59	Too large.
$NiCr_2O_4$	Cubic-Spinel	8.32	High melting.
$MgCr_2O_4$	Cubic-Spinel	8.32	High melting.
$LiMg_5Ti_{1.5}O$	Cubic-Spinel	8.37	Decomposes.
$LiMnTiO_4$	Cubic-Spinel	8.30	Decomposes.
$LiGaTiO_4$	Cubic-Spinel		Two phases.
$LiAlTiO_4$	Cubic-Spinel	8.34	Two phases.
$LiCrTiO_4$	Cubic-Spinel	8.32	Two phases.
Co_2GeO_4	Inverse-Spinel	8.32	Decomposes.
Co_2SnO_4	Inverse-Spinel	8.63	Too large.
Co_2TiO_4	Inverse-Spinel	8.445	Too large.
Co_2VO_4	Inverse-Spinel	8.328	
Mg_2GeO_4	Inverse-Spinel	8.245	Decomposes.
Mg_2SnO_4	Inverse-Spinel	8.60	Too large.
Mg_2TiO_4	Inverse-Spinel	8.44	Too large.
Mg_2VO_4	Inverse-Spinel	8.403	Too large.
Mn_2VO_4	Inverse-Spinel	8.575	Too large.
$KGa_{11}O_{19}$	Hexagonal	a=5.800	*Too small.
$BaAl_{12}O_{19}$	Hexagonal	a=5.587	Too small.
$SrGa_{12}O_{19}$	Hexagonal	a=5.794	Too small.
$BaGa_{12}O_{19}$	Hexagonal	a=5.850	Too small.
$Sr(Ga,Mg,Zr)_{12}O_{19}$	Hexagonal	a=5.82	Too small.
$Ba_3(VO_4)_2$	R-Hexagonal	a=5.78	Too small.
$Ba_3(VO_4)_{1.2}(TaO_4)_{.8}$	R-Hexagonal	a=5.893	Exact match for barium ferrite.

*Cell dimension too great (small) for effective epitaxy.

7

on properties. The table includes hexaferrite analogs, cubic spinels, and inverse spinel compounds. Some of the materials, such as $ZnGa_2O_4$ and Co_2GeO_4, decompose at their melting points while some exhibit such high melting points that crystal growth is difficult ($NiCr_2O_4$ and $MgCr_2O_4$). Some, when synthesized as powders, have the proper structure, e.g., $LiCrTiO_4$ and $LiGaTiO_4$, but when melted decompose to two phases. From this survey, four promising candidates based on structure, cell dimension, and melting behavior were selected for crystal growth experiments: barium aluminate, strontium hexagallate, cobalt gallate, and barium vanadate.

3.3 SUBSTRATE CRYSTAL GROWTH AND CHARACTERIZATION

3.3.1 Barium Aluminate

Barium aluminate ($BaAl_{12}O_{19}$) is the aluminum analog of barium hexaferrite. Its cell dimensions are $\underline{a}$ = 5.587 Å and $\underline{c}$ = 22.68 Å. Figure 2 illustrates the partial phase diagram of the $BaO-Al_2O_3$ system [23]. It shows that the hexaluminate melts noncongruently and that growth takes place in a phase field bounded by a eutectic (B) and a peritectic (A). Attempts to increase the cell dimensions by chemical substitution to more closely match that of barium ferrite ($\underline{a}$ = 5.893 Å; $\underline{c}$ = 23.194 Å) were unsuccessful.
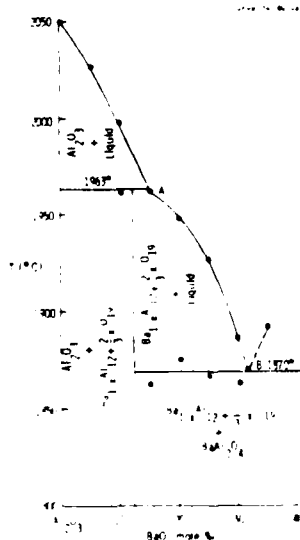
Figure 2 — Partial phase diagram of $BaO-Al_2O_3$ (Reference 23).

8

Figure 3 — Barium hexaluminate single crystal.
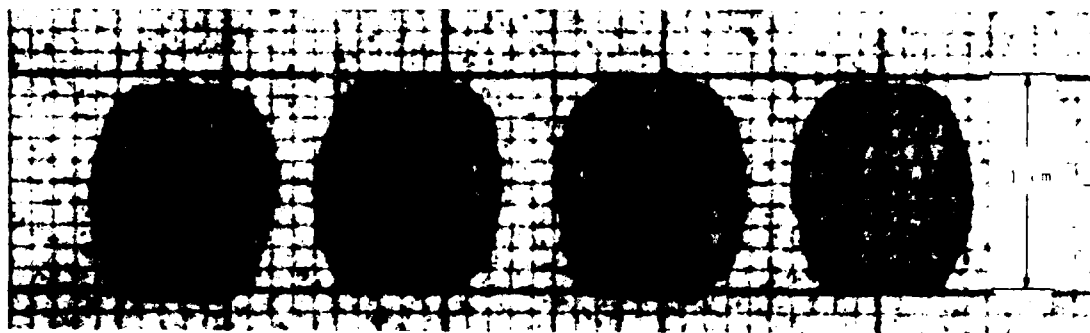
Figure 4 — $BaAl_{12}O_{19}$ substrates.

Unsubstituted crystals of barium aluminate were successfully grown by the Czochralski technique in an iridium crucible at a temperature of 1950 ± 25°C. The growth rate was 1 mm/hr and rotation rate was 100 rpm. Figure 3 shows a boule of $BaAl_{12}O_{19}$, and Figure 4 shows substrates cut from it. The substrates were polished with Syton on a politex pad. The substrates have a very low defect density as measured by etchpit density techniques.

3.3.2 Strontium Hexagallate

Early attempts to grow $SrGa_{12}O_{19}$ crystals met with limited success because of incongruent melting of the compound and small solid solution range. Figure 5 shows the phase diagram of the $SrO-Ga_2O_3$ system in which $SrGa_{12}O_{19}$ crystallizes. From it we see an even narrower phase field than $BaAl_{12}O_{19}$. By adopting the strategy of Mateika and Laurien [24] and substituting magnesium and zirconium to broaden the gallate stability region, we were able to grow small crystals using a conventional crystal puller with pyrometer temperature control. Figure 6 is a ternary phase diagram of the $SrO-Ga_2O_3-(Mg,Zr)$ oxide system showing the boundaries of the hexagallate growth. Compositions marked a, b, and c were used for crystal growth by us. Composition c was most successful.

The Mg,Zr-substituted strontium hexagallate composition was successfully grown as single crystals using an Autox automated crystal-growth furnace. This system controls crystal diameter by the crystal-weighing technique. With this system growth could be continued at slow rates for several days, thus minimizing interface instability associated with solid solution melts. Crystals to 7 cm in length and 1.5 cm in diameter have been grown, as in Figure 7 for example. Growth parameters were 1 mm/hr growth rate and 10 rpm rotation rate. The growth direction was perpendicular to [0001] to avoid $\underline{c}$ face cleavages.

The crystals as grown were greenish in color and had specks of iridium metal on their surfaces. Some polished slices from some portions of the crystals contained white, dendritic inclusions but did not contain iridium particles. Cell dimensions measured on samples taken from both ends of a crystal show little difference (Table 2).

10
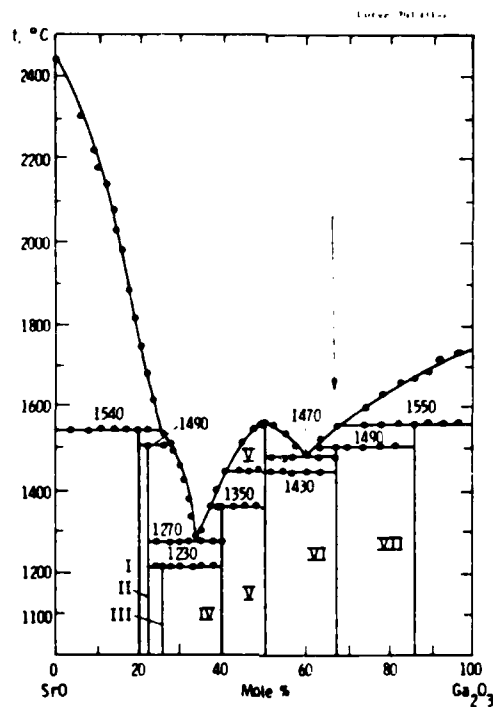
Figure 5 — Phase diagram of $SrO\text{-}Ga_2O_3$ (Reference 25).
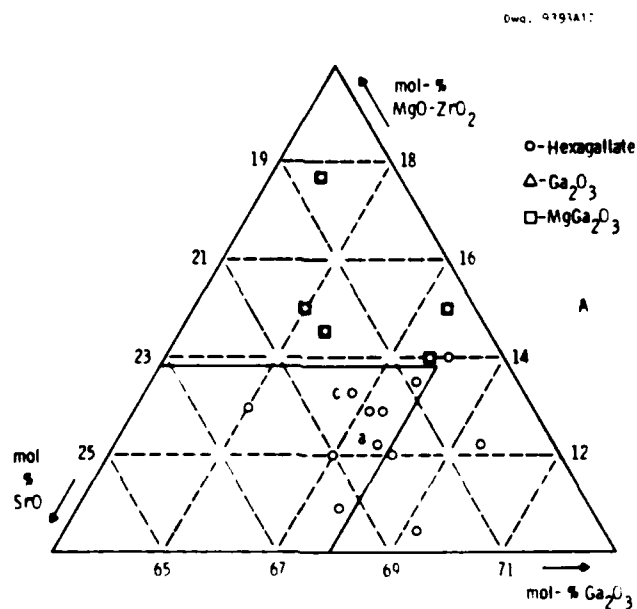
Figure 6 — A portion of the pseudo-ternary system $SrO\text{-}Ga_2O_3\text{-}(MgO\text{-}ZrO_2)$.
After reference 24.

11

Table 2

Cell Dimensions for the Top and
Bottom of a Strontium Gallate Crystal

	a, Å	c, Å
Top	5.8199	23.060
Bottom	5.8205	23.059

3.3.3 Cobalt Gallate

Cobalt gallate [26] is a congruently melting, cubic material
with a spinel structure having a cell dimension of 8.326 Å. The melting
point is 1825 ± 5°C requiring that an iridium crucible be used for
crystal growth. The crystals are deep blue due to their high cobalt
concentration (see Appendix I for details).

Two difficulties were overcome in developing a successful crys-
tal growth technique. (1) Because of its strong optical absorption,
heat is not readily dissipated through cobalt gallate crystals. As a
result, the solid-liquid interface was concave under most conditions of
pull and rotation rate. (2) Significant loss of cobalt gallate can
occur by evaporation from the melt.

To minimize melt evaporation, growth was accomplished in an ADL
model MP pressurized Czochralski puller. Overpressures of 50 psi argon
significantly reduced the loss of cobalt gallate from the melt during
growth. In general, we found empirically that slow growth and rotation
rates, coupled with the use of a water-cooled pull rod and the position-
ing of the top heat reflector 2 to 3 inches from the melt surface,
produced flat to convex crystal-liquid interfaces. Under these condi-
tions, we achieved improved diameter stability. Crystals up to 2.5 cm
long by 1 cm diameter were grown.

A number of the properties of $CoGa_2O_4$ were measured to charac-
terize its suitability as a substrate. The measured cell dimension of

12

METRIC 1 2 3 4 5 6 7

$SrGa_{12}O_{19}-(Mg,Zr)$

Figure 7 — A single crystal of Mg,Zr-substituted strontium gallate.

undoped $CoGa_2O_4$ is 8.323 ± .005 Å, slightly smaller than the value required for hexaferrite epitaxy, 8.336 Å. Figure 8 shows that the cell dimension can be increased to produce lattice matching by the replacement of gallium with indium.

The average thermal expansion coefficient for cobalt gallate measured by quartz tube dilatometry was 9×10^{-6}. This is comparable to that of the hexaferrites.

The dielectric constant and loss tangent were measured on samples of $CoGa_2O_4$ (see Table 3). The relative permittivity of cobalt

Table 3

Dielectric Constant and Loss Tangent
of $CoGa_2O_4$ Crystals

Sample	Dimensions (mm)	Frequency (GHz)	E_r	Tan δ_e
1	1.15 x 0.8 x 14.1	9.169	9.24	0.0030
2	1.15 x 0.7 x 14.1	9.173	9.08	0.0024
3	1.15 x 0.7 x 14.1	9.178	9.26	0.0015

gallate, about 9.2, is comparable to values for other nonmagnetic insulators like alumina or gadolinium garnet. The tan δ_e values 0.0015 to 0.003 are higher than the value of <0.001 desired for a millimeter-wave ferrite in order to minimize device losses.

The optical transmission between 0.3 and 1.5 μm is virtually featureless, showing almost no transmission at any wavelength except between 0.7 and 0.9 μm, where the transmission peaks at 50%, then falls back to zero. The spectrum between 1.5 and 12 μm is illustrated in Figure 8. Again, the material transmits relatively poorly except for a window between about 3 and 5 μm.

Further details of the cobalt gallate growth and properties are given in Appendix I and reference 26.

3.3.4 Barium Vanadate

Barium vanadate is a congruently melting compound which can be lattice-matched to barium ferrite by substitution of vanadium by tantalum. The compound is synthesized by weighing stoichiometric portions of barium carbonate and vanadium oxide, then mixing and firing the powders at 600°C for 12 hours. Crystals are grown by the Czochralski technique. The melting temperature of barium vanadate is 1625 ± 25°C. Typical growth parameters are 1 to 6 mm/hr withdrawal rates and between 20 and 60 rpm rotation rate. Figure 10 is a sectional view of the growth furnace configuration we employed (see Appendix II for details).

As-grown crystals varied in color from smokey to rose. Figure 11 illustrates a crack-free, tantalum-substituted barium vanadate crystal, 5 cm long by 2 cm in diameter.

A number of physical properties were measured to characterize the crystals. Cell dimensions of the unsubstituted barium vanadate were $\underline{a}$ = 5.790 ± .001 Å and $\underline{c}$ = 23.340 ± .001 Å, which poorly match those of barium ferrite ($\underline{a}$ = 5.893 Å, $\underline{c}$ = 23.194 Å). When 40% of the vanadium is replaced by tantalum, the "a" parameter then exactly matches the ferrite. Table 4 shows the variation of cell dimension with tantalum substitution.

15
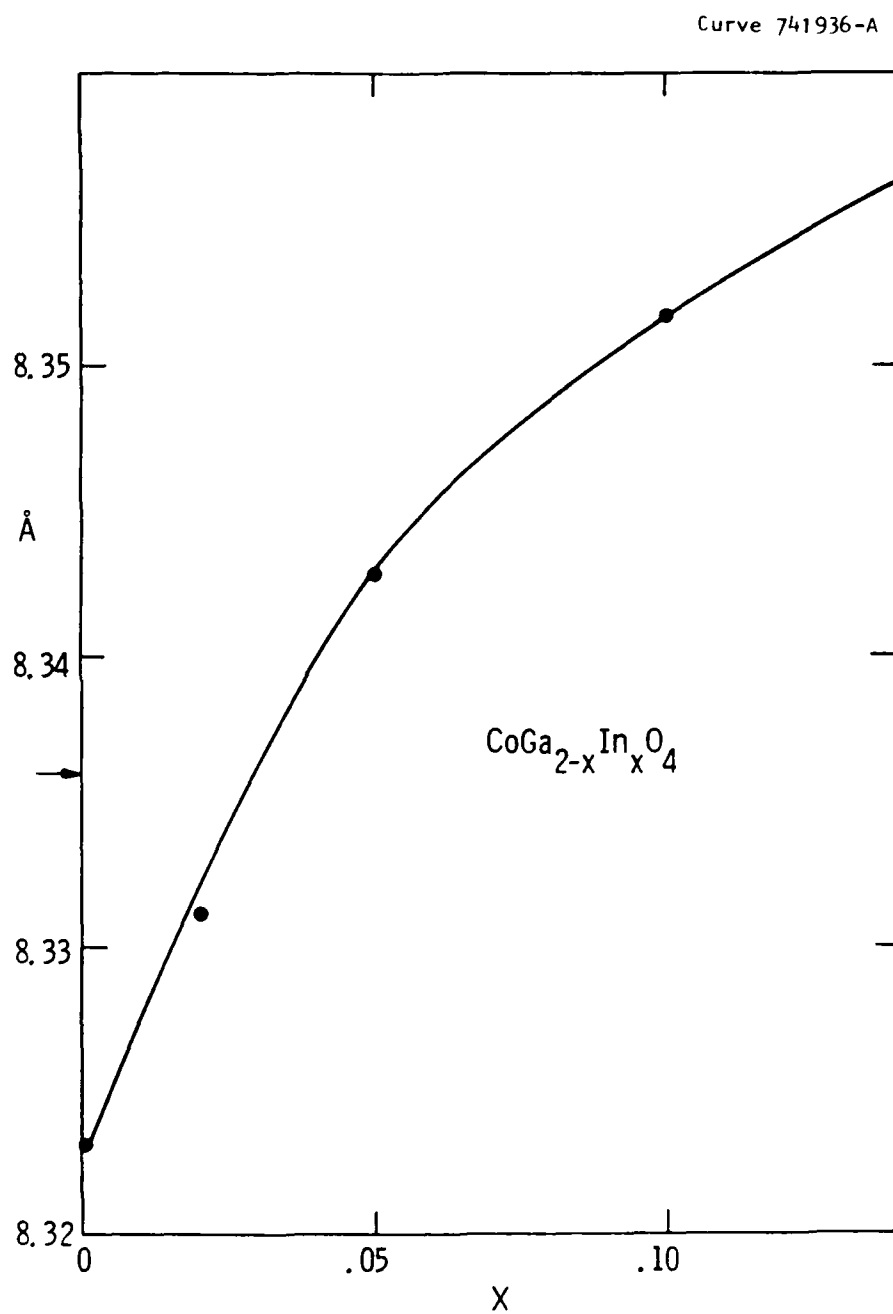
Figure 8 — Lattice parameter versus composition for $CoGa_{2-x}In_xO_4$.

Curve 746496-A
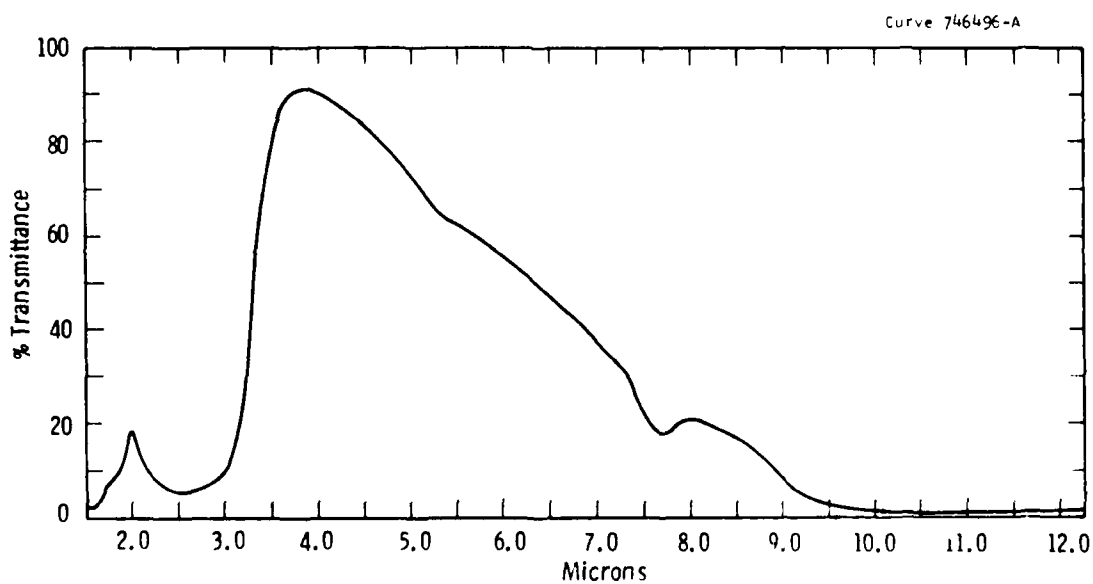
Figure 9 — Optical transmittance of $CoGa_2O_4$ crystal from 1.5 to 12 μm.

17
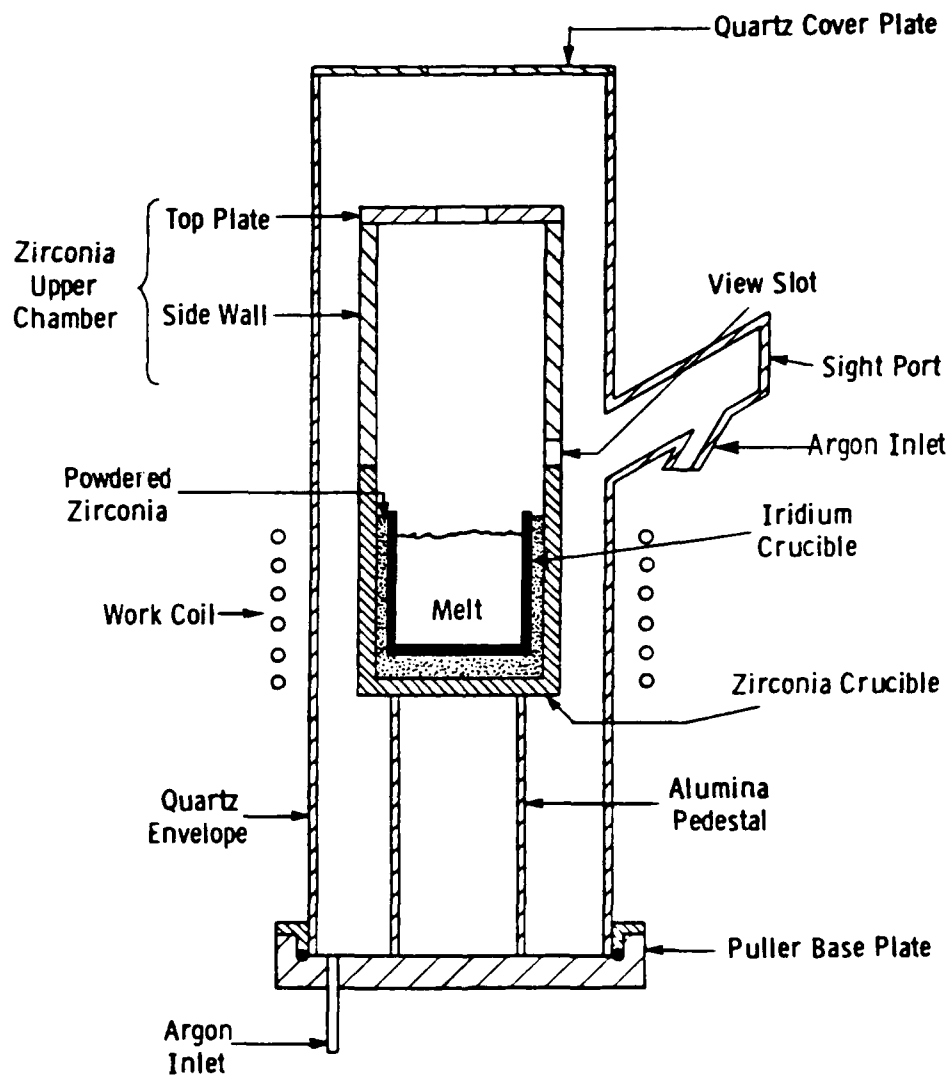
Figure 10 — Sectional view of crystal-growing furnace (schematic).

18

$$Ba_3(VO_4)_{1.2}(TaO_4)_{.8}$$
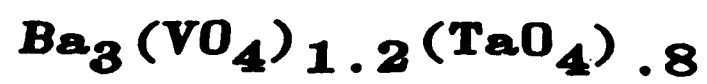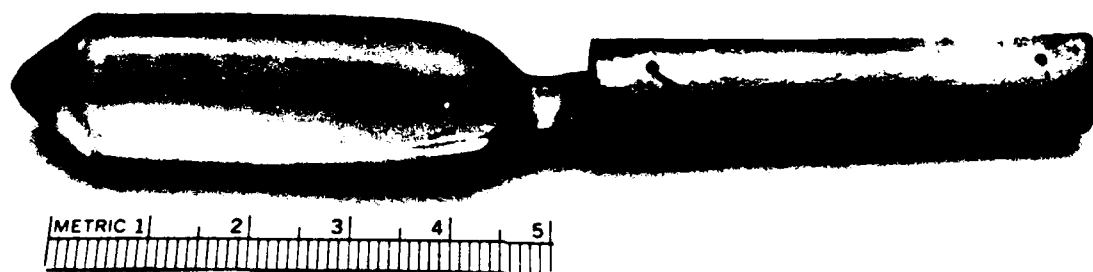
Figure 11 — Czochralski crystal.

Table 4

Variation in Cell Dimensions of Barium Vanadate with Tantalum Substitution

$$Ba_3(VO_4)_{2-x}(TaO_4)_x$$
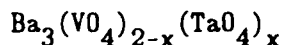
x	a	c
0	5.790	21.340
.2	5.810	32.430
.4	5.838	21.315
.6	5.865	21.306
.8	5.893	21.303
1.0	5.920	21.302*
1.2		*

*Presence of extra lines on the x-ray pattern indicating that a phase transformation or phase separation takes place.

Thermal expansion measurements on $Ba_3(VO_4)_2$ illustrate the material's anisotropy. The average thermal expansion parallel to the "c" axis is 10×10^{-6} $°C^{-1}$; perpendicular to the "c" axis it is 19×10^{-6} $°C^{-1}$. The exact value depends on temperature. These values are comparable to those measured for hexaferrites. Figures 12 and 13 are plots of the thermal expansion from room temperature to 1000°C for directions parallel and perpendicular to the "c" axis.

Measurements of the dielectric constant, loss tangent, and magnetization were made on samples of $Ba_3(VO_4)_2$; Table 5 presents the results of the determination. The magnetization is lower than that of gadolinium gallium garnet (+49 G), which is the standard substrate for yttrium iron garnet epitaxial film growth. The dielectric constant is slightly larger than values for standard insulators such as alumina (about 9), and the loss tangent is also higher than that of alumina (0.0001).
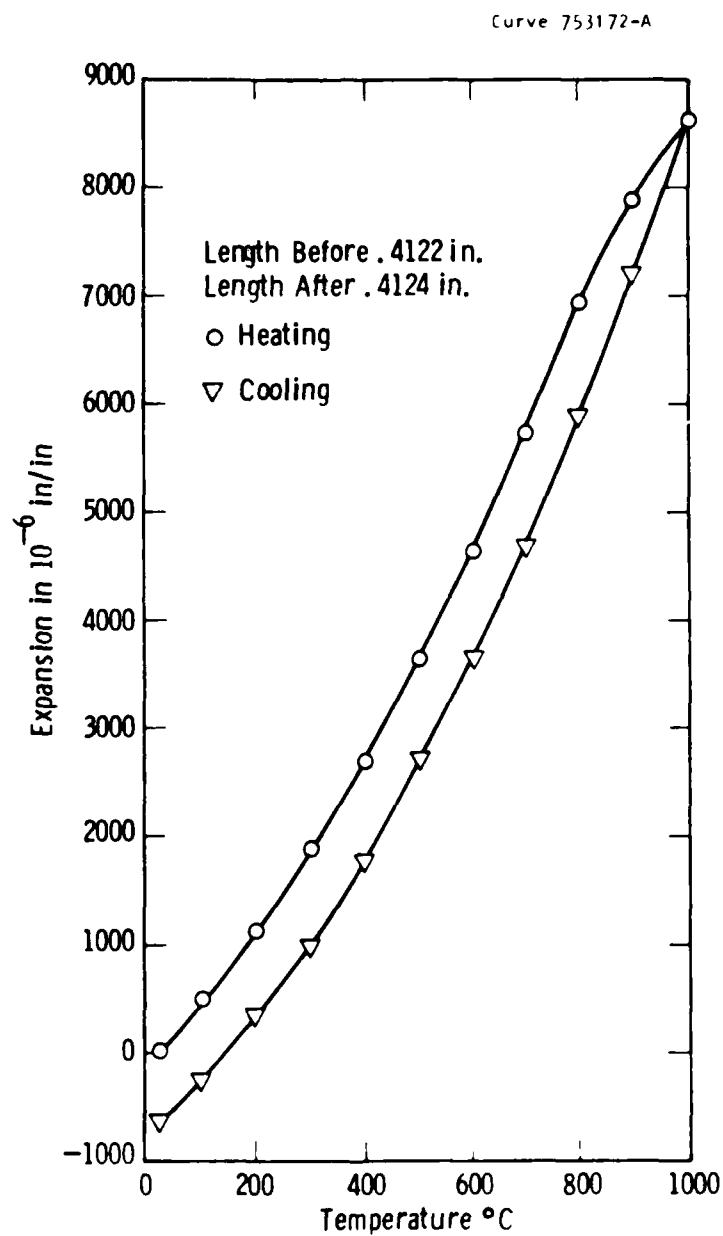
Figure 12 — Thermal expansion of barium vanadate parallel to "c" direction cycled from RT to 1000°C to RT in air.
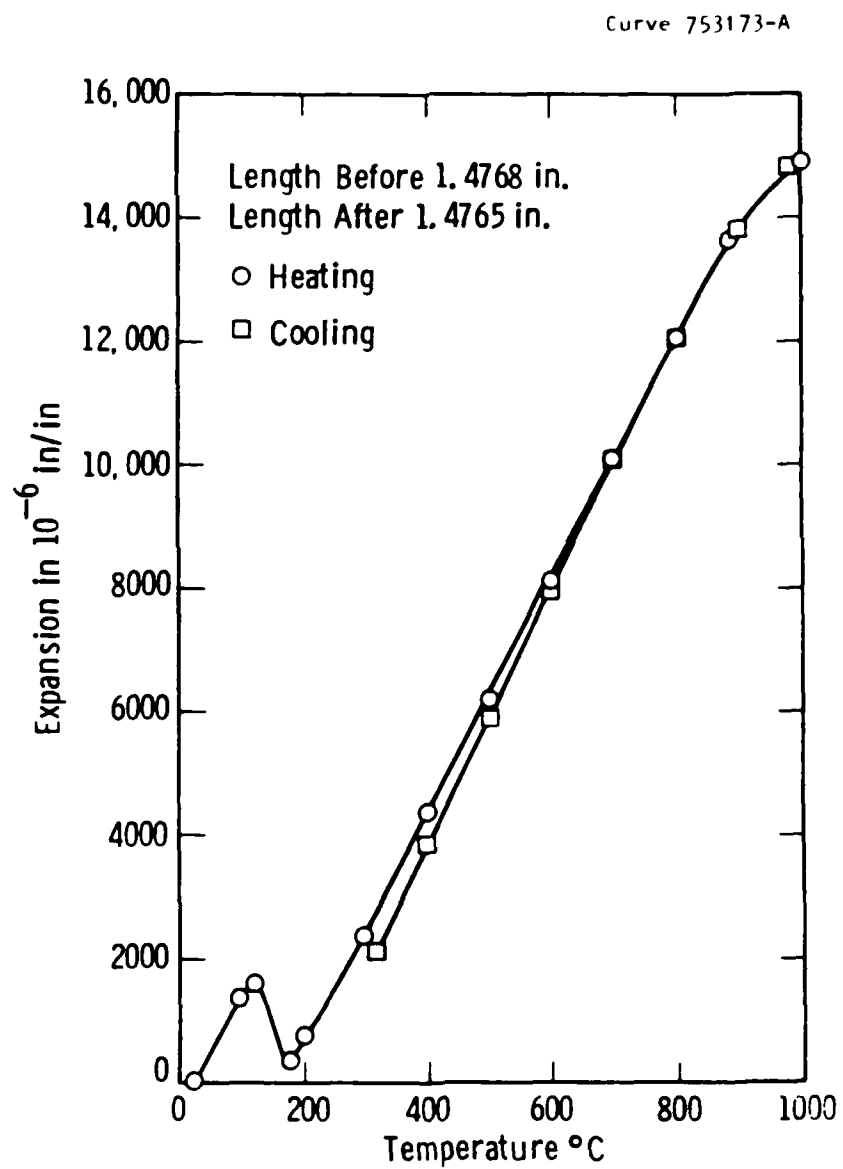
Figure 13 — Thermal expansion of barium vanadate perpendicular to "c"
direction cycled from RT to 1000°C to RT in air.

Table 5

Dielectric and Magnetic Properties
of Unsubstituted Barium Vanadate

Dielectric Constant E_r	Loss Tangent $\tan \delta$	Magnetization $4\pi M$ (G)
12.0	0.0016	+3.8

As noted, we found variations in the color of crystals grown from melts of the same nominal composition and produced with the same growth conditions. To gain insight into this phenomena, optical trans mission measurements were made on polished, 1 mm thick crystal slices. The transmission spectrum between 0.3 to 1.5 μm was featureless with transmission (uncorrected for reflection) of about 80%. Figure 14 illustrates the transmission spectra between 2.5 and 10 μm. Spectra of other crystals were similar, and the origin of the color variation was not clearly resolved.
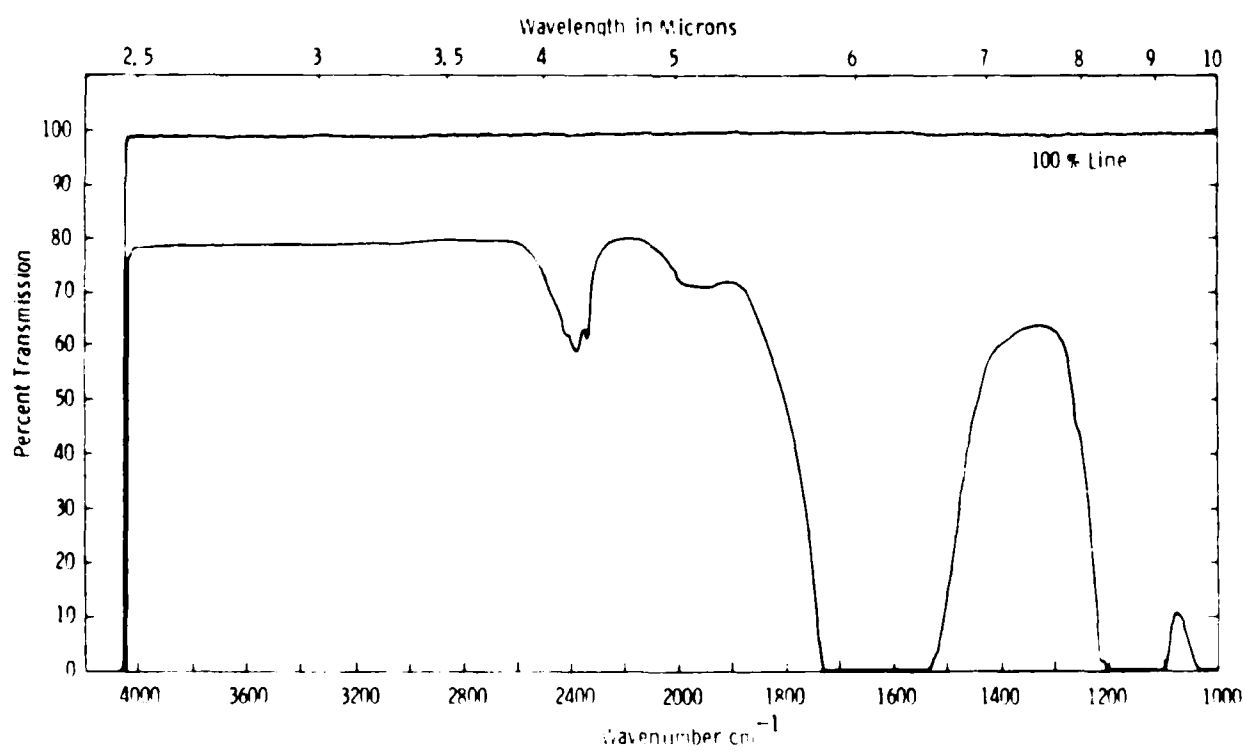
Figure 14 — Optical transmittance of $Ba_3(VO_4)_2$ crystal, 2.5-10 μm.

24

4. LIQUID PHASE EPITAXY
OF HEXAFERRITE FILMS

Previous sections of this report describe the synthesis and crystal growth of new substrate materials such as $CoGa_2O_4$, $Ba_3(VO_2)_4$, the solid solution $Ba_3(VO_4)_{1.2}(TaO_4)_{0.8}$, and $Sr(Ga,Mg,Zr)_{12}O_{19}$. A number of initial tests were also done on readily available MgO substrates. These helped to identify the breadth of growth conditions. Here we summarize the liquid phase epitaxy (LPE) experiments performed on these substrates under various growth conditions. Details are given in Appendices III and IV.

4.1 INTRODUCTION

In LPE, a small lattice mismatch between film and substrate is crucial to grow good-quality films. However, it is also important to choose a flux system which is chemically and thermally compatible with those substrates. Most of the reported work on the LPE growth of hexaferrite films employs flux systems similar to those which have been used for LPE garnet (YIG) film growth. However, in the present investigation, we found that the conventional fluxes were not satisfactory for some of the new substrates, resulting either in chemical attack of the substrates or restricted film nucleation. Therefore, emphasis was placed on identifying solutions which favor chemical and thermal compatibility with the substrate materials, as well as facilitating hexaferrite film growth.

We initially surveyed substrate behavior during the LPE growth of barium hexaferrite films from a variety of flux systems. The results are summarized in Table 6. During these preliminary studies of the solvents, the Bi_2O_3-BaO-B_2O_3 flux system emerged with the best overall combination of properties.

Table 6

Survey of Hexaferrite Growth for Various
Substrate and Flux Systems Studied

Flux Constituents	Mole % Solute	Growth Temp. (°C)	MgO	CoGa$_2$O$_4$	Ba$_3$(VO$_4$)$_2$	Ba$_3$(VO$_4$)$_{1.2}$(TaO$_4$)$_{0.8}$	SrGa$_{12}$O$_{19}$
PbO PbF$_2$	13.5	928	Weight loss. Vigorous reaction.		No film.		
BaCO$_3$(BaO) B$_2$O$_3$	19.0	900 1082	Weight loss.		Substrate dissolved.		
BaCO$_3$(BaO) BaF$_2$ B$_2$O$_3$	23.2 24.8	1007 971 1025 1000		Film grown matt surface.	No film.		
Bi$_2$O$_3$	29.5	922-932	Very thin film grown.	Film grown.	Substrate dissolved.		Best film grown.
B$_2$O$_3$	32.2	967-989	Slow growth rate.				
BaO V$_2$O$_5$		727			Substrate dissolved.		
Na$_2$O B$_2$O$_3$		834			Substrate dissolved.		
BaO Bi$_2$O$_3$ B$_2$O$_3$		911 1008	Very thin orthoferrite film grown.		No film.	Orthoferrite film grown with inter-diffusion between substrate and film.	Best film grown.

26

Qualitative measurements of the melting temperature and the degree of supercooling of the various hexaferrite-solvent solutions were performed by observing the appearance and disappearance of spontaneously nucleated crystallites in each melt during repeated slow cooling and heating cycles. Crystallites were then collected from each melt using a platinum basket in order to facilitate the analysis of their phase composition by x-ray diffraction measurements. The phases identified in the collected crystals, the liquidus temperature, and the degree of supercooling for each solution composition were tabulated. As an example, data for the Bi_2O_3-BaO-B_2O_3 system are shown in Figure 15. The barium hexaferrite-saturated solutions based on this latter solvent exhibited relatively larger degrees of supercooling than the other systems, e.g., up to 65°C. Thus, it was possible to choose a low growth temperature below 1000°C without any spontaneous nucleation.

We were able to grow hexaferrite films successfully on three substrates: $Sr(Ga,Mg,Zr)_{12}O_{19}$, $CoGa_2O_4$, and $Ba_3(VO_4)_{1.2}(TaO_4)O_{0.8}$. Table 7 summarizes the typical film growth conditions on these substrates. The films were grown by two different methods: (1) vertically dipped, stationary substrate; and (2) horizontally dipped, rotated substrate. The hexaferrite films were characterized for surface structure, composition, cell dimensions, and interface behavior. The hexaferrite film composition was also adjusted in some cases by replacing Fe by Al in order to reduce lattice mismatch between the film and substrates. Table 8 shows the cell dimensions of three different film compositions measured by x-ray diffraction.

4.2 FILM CHARACTERISTICS

4.2.1 Growth on $CoGa_2O_4$

Hexaferrite films were produced on $CoGa_2O_4$ substrates from a conventional BaF_2-BaO-B_2O_3 flux, from Bi_2O_3-B_2O_3, and from the new Bi_2O_3 BaO B_2O_3 flux. In general, the results were similar. The films exhibited patches of matte finish and smooth regions to the unaided eye.

27

	COMPOSITION (MOLE %)			L.T. (°C)	ΔT (°C)	CRYSTALLITE
	Bi_2O_3	BaO	Fe_2O_3			
A	67.3	14.9	17.8	874	36	$BaFeO_{2.8}$
B	60	15	25	973	58	$BaFeO2.8$
C	55	15	30	1035	65	$BaFe_{12}O_{19}$, $BaFeO_{2.8}$
D	50	15	35	1113	58	$BaFe_{12}O_{19}$
E	35	25	40	1136	27	$BaFe_{12}O_{19}$, Fe_3O_4
F	50	20	30	1010	38	$BaFe_{12}O_{19}$
G	68.5	4.5	27	960	45	$BaFe_{12}O_{19}$, $BiFeO_3$
H	69.7	4.3	26	938	50	$BaFe_{12}O_{19}$, $BiFeO_3$

L.T. : Liquidus Temperature

ΔT : Degree of Supercooling

Figure 15 — Observed behavior of hexaferrite-$(Bi_2O_3$-BaO-B_2O) solutions

Table 7

LPE Growth Condition and Characteristics
of Barium Hexaferrite Films

Flux: Bi_2O_3-B_2O_3 and Bi_2O_3-BaO-B_2O_3

Substrate	Sample Desig-nation	Super Cool-ing (°C)	Growth Temp. (°C)	Film Thick-ness (μm)	Growth Rate (μm/min)	Surface Morphology	Remarks
$CoGa_2O_4$	BFO5	9	981	7.5	0.23		Considerable diffusion at interface.
	BFO9	24	966	N.M.	-		
	BFO17	8	932	3.5	0.35	Some smooth, some terraced areas.	Less interdif-fusion than BFO5 film peeling.
	BFO21	23	959	10	0.5	Structured surface.	Same as BFO19.
Doped-$SrGa_{12}O_{19}$	BFO10	22	968	18	1.2	Mainly smooth with a few terraces.	
	BFO11	21	969	2.8	0.56	Relatively smooth all over.	No interdiffu-sion; film is cracked.
	BFO19	23	959	<1 2-3 10	0.1-0.15 0.5	Corresponds to substrate consisting of three differ-ently orient-ed sections.	Horizontal dip at 50 rpm. Film lattice parameter is adjusted by Al doping.

(Continued)

Table 7 (Continued)

Substrate	Sample Designation	Super Cooling (°C)	Growth Temp. (°C)	Film Thickness (μm)	Growth Rate (μm/min)	Surface Morphology	Remarks
Doped-$SrGa_{12}O_{19}$	BF052	27	911	40	2.8	Hexagonal islands with cracks.	Horizontal dip at 50 rpm.
	BF053	24	914	40	2.8	Dense and adherent without cracks.	Horizontal dip at 50 rpm. $BaFe_{10.7}Al_{1.3}O_{19}$
	BF058	34	1001	40	2.8	Cracks with terraced surface.	Horizontal dip at 50 rpm. $BaFe_{9.3}Al_{2.7}O_{19}$
	BF059	27	1008	10	2	Very smooth with a few cracks.	Same as BF058.
	BF060	27	1008	5	1.6	Very smooth all over.	Same as BF058.
$Ba_3 VO_4 1.2 (TaO_4)_{0.8}$							
	BF057	41	994	120	13	Orthoferrite layer.	Horizontal dip at 50 rpm. Considerable interdiffusion at interface.
	BF062	27	1008	40	8	Structured surface.	Same as BF058.

Table 8

Cell Dimensions of Barium Hexaferrite Films

Film Composition	Cell Dimensions
$BaFe_{12}O_{19}$	a_o = 5.893, c_o = 23.191
$BaFe_{10.7}Al_{1.3}O_{19}$	a_o = 5.845, c_o = 22.988
$BaFe_{9.3}Al_{2.7}O_{19}$	a_o = 5.801, c_o = 22.884

At high magnification, the matte regions were composed of small hexagonal facets (Figure 16), a feature of hexagonal ferrite films well documented in the literature.

Occasional fine cracks were observed which apparently propagated from the substrate. This was attributed to the remaining small mismatch between the substrate and $BaFe_{12}O_{19}$ film. Complete lattice matching was not achieved during this study due to the difficulty in growing In-doped $CoGa_2O_4$.

A characteristic feature of the films we grew on $CoGa_2O_4$ was the formation of an interdiffusion layer between the film and substrate. (see Figure 17). Microprobe measurements indicated that iron had diffused during the film growth process, introducing an iron-rich region in the substrate. This layer apparently weakened the bond at the interface, in some cases leading to film peeling. The interdiffusion layer also led to a broad resonance linewidth in the film.

Spinel layers were also successfully deposited epitaxially on $CoGa_2O_4$. For details, see Appendix I.

4.2.2 Growth on Substituted Barium Vanadate Substrates

Figure 18a and 18b are, respectively, the optical and SEM micrographs taken from the cross section of an LPE film grown on a $Ba_3(VO_4)_{1.2}(TaO_4)_{0.8}$ substrate. These micrographs show that a signifi cant interdiffusion layer was found between the two. Electron micro probe scans of these samples showed that vanadium and tantalum diffused

31
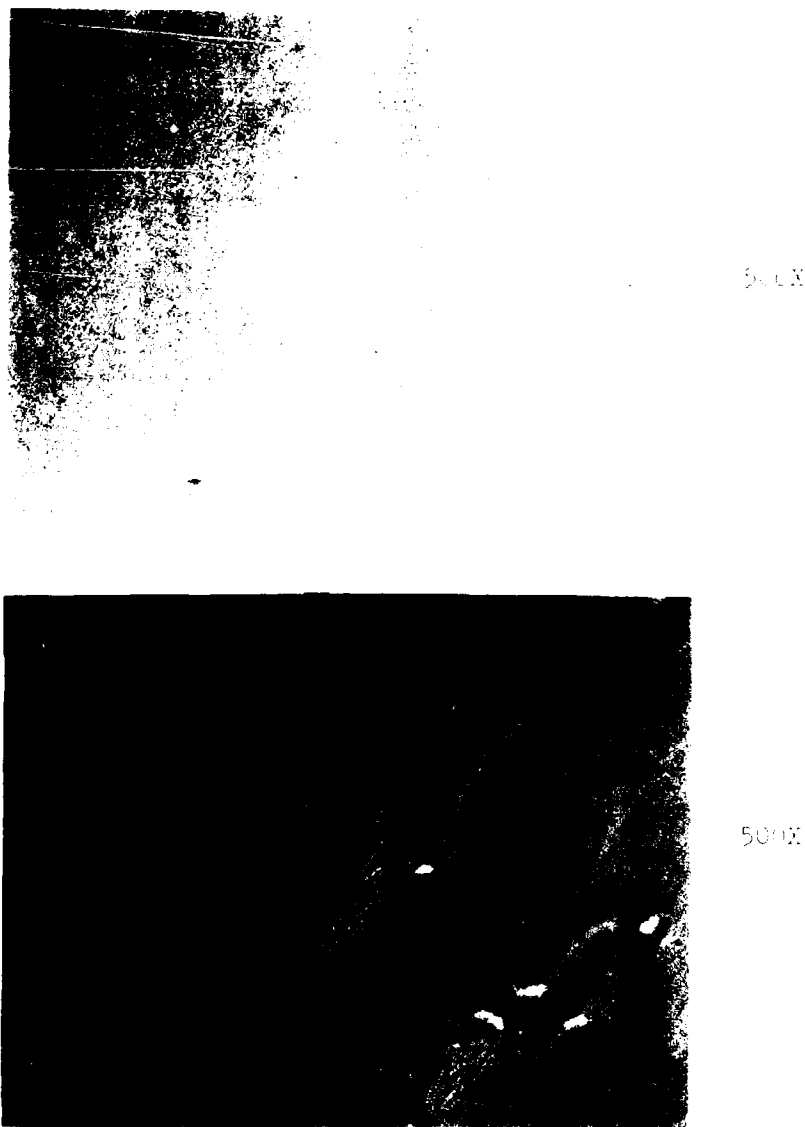
Figure 16 — Photomicrographs of barium hexaferrite LPE layer on $CoGa_2O_4$ substrate. Some areas of the film exhibit a terraced structure.

(a)   500X

(b)   500X
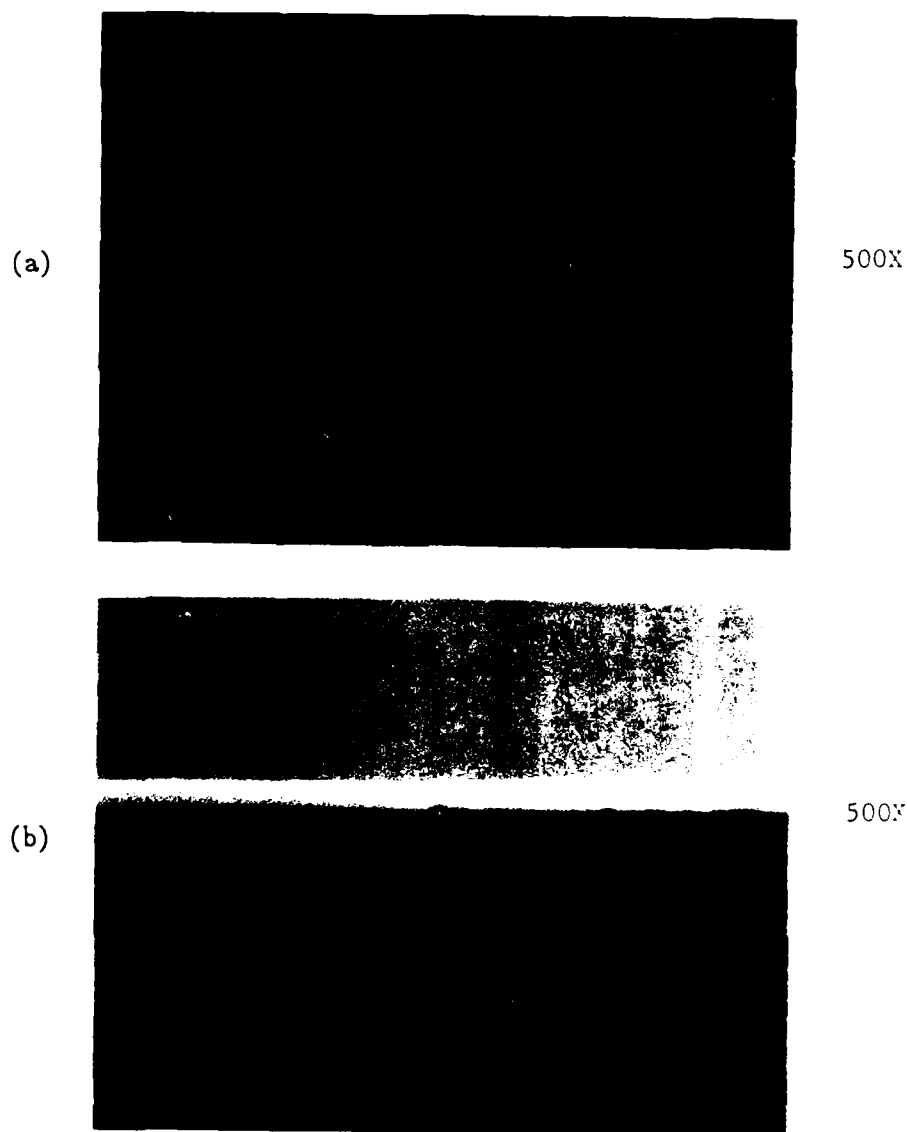
Figure 17 — (a) Layer-substrate interface for $CoGa_2O_4$ substrate.
(b) For comparison, a sharply delineated LPE layer-
$SrGa_{12}O_{19}$ interface is also shown.

33

interdiffusion layer ——↑

(a) Optical Micrograph

↑—— interdiffusion layer

(b) SEM

Figure 18 — Film-substrate interface for $Ba_3(VO_4)_{1.2}(TaO_4)_{0.8}$ substrate taken by (a) optical microscopy and (b) scanning electron microscopy. Film was grown for 15 min at 994°C (Table 7).

to the film from the substrate. This film was grown for 15 min and the film thickness was about 120 μm. In an attempt to minimize the inter-diffusion, a film was grown for 3 min and examined by optical microscopy (Figure 19). As shown in the figure, no significant interdiffusion layer was observed. However, the interface between film and substrate was not smooth, and apparently chemical attack on the substrate had occurred.

Analysis by x-ray diffraction of samples taken from the films indicated that the layers were composed of at least two phases, a bismuth orthoferrite and an unidentified tantalum-rich oxide. Either the substrate nucleated the orthoferrite directly or interdiffusion and chemical reaction with the flux caused the initially nucleated hexaferrite to convert to orthoferrite.

4.2.3 Growth on Substituted Hexagallate Substrate

The best quality barium hexaferrite films were grown on $Sr(Ga,Mg,Zr)_{12}O_{19}$ substrates using compositions in the Bi_2O_3-BaO-B_2O_3 flux system. This combination produced the lowest lattice mismatch between substrate and film in our studies. The detailed results are described in the paper [28] of Appendix IV and summarized here. The control of the lattice mismatch was approached in two different ways—by adjusting the lattice parameter of substrate as well as that of the film. As shown in Table 8, the replacement of Fe by Al in barium hexa-ferrite brings the $Sr(Ga,Mg,Zr)_{12}O_{19}$ substrate and film lattices into better registry.

The film microstructures of five typical samples grown on stron-tium gallate and examined by optical microscopy and x-ray topography are described here. Figure 20a and 20b are Berg-Barrett surface reflection x-ray topographs taken from an unsubstituted $BaFe_{12}O_{19}$ film and a $BaFe_{10.7}Al_{1.3}O_{19}$ film. The x-ray topograph of the unsubstituted barium hexaferrite film exhibits large numbers of white line images. However, the film structure of $BaFe_{10.7}Al_{1.3}O_{19}$ shows none of the line defect images. The line defect images, which are out of x-ray diffraction contrast, are due to the cracks in the film.

FILM

SUBSTRATE

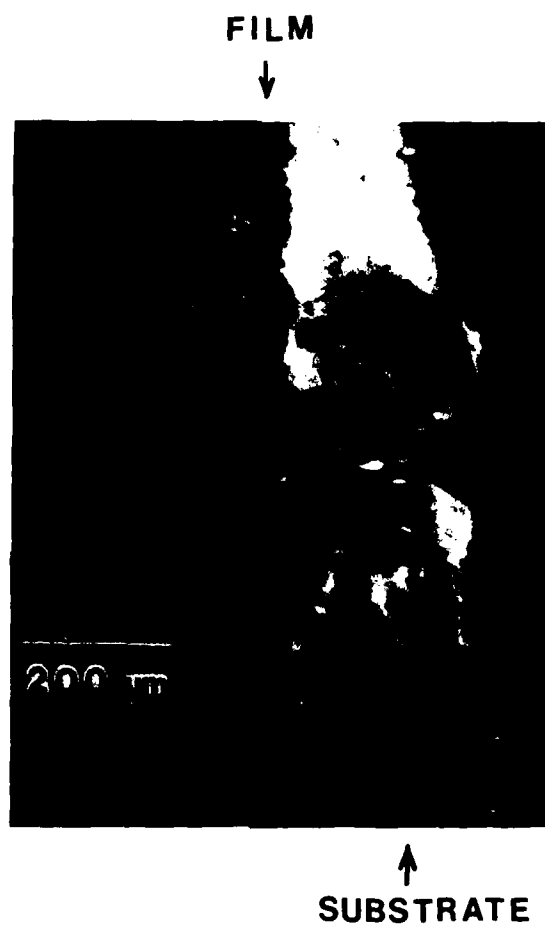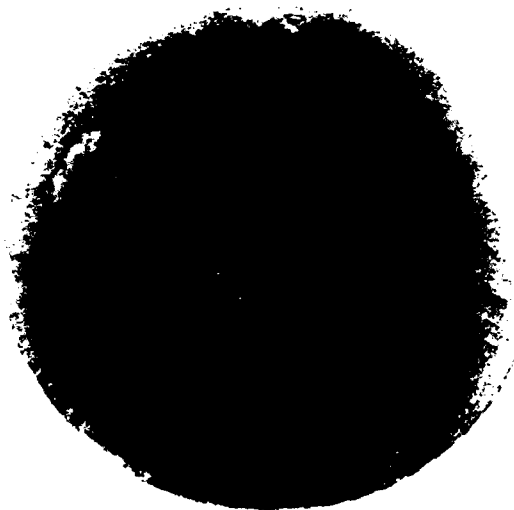Figure 19 — An optical micrograph of film-substrate interface for
$Ba_3(VO_4)_{1.2}(TaO_4)_{0.8}$ substrate. Film was grown for 3 min
at 1008°C (Table 7).

36

(a) $BaFe_{12}O_{19}$ Film

(b) $BaFe_{10.7}Al_{1.3}O_{19}$

Figure 20 — Berg-Barrett surface reflection x-ray topographs taken from (a) $BaFe_{12}O_{19}$ film and (b) $BaFe_{10.7}Al_{1.3}O_{19}$ film on $Sr(Ga,Mg,Zr)_{12}O_{19}$ substrates.

RM-12656

Both x-ray topographs also show one or two areas without x-ray diffraction contrast. These are probably regions where the films did not grow epitaxically, or where the substrate was misoriented with respect to the film matrix. The optical microscopic observation of these films indicated that the unsubstituted barium hexaferrite film exhibited hexagonal island structure in the presence of large numbers of cracks. In contrast, the aluminum-doped $BaFe_{10.7}Al_{1.3}O_{19}$ film appears dense, adherent, and without cracks.

Figure 21a, 21b, and 21c are optical micrographs taken from $BaFe_{9.3}Al_{2.7}O_{19}$ films having film thicknesses of 40 μm, 10 μm, and 5 μm, respectively. The 40 μm thick film exhibits a "roofing shingle" type structure with a large number of cracks. The 10 μm thick film shows fewer cracks, and the surface appears topographically very smooth. The structure of the 5 μm thick film appears very smooth and crack-free.

Collectively, the results indicate that the best films were obtained from the composition $BaFe_{10.7}Al_{1.3}O_{19}$, which has the lowest lattice mismatch among the three film compositions examined. For example, $BaFe_{10.7}Al_{1.3}O_{19}$ and $BaFe_{9.7}Al_{2.3}O_{19}$ films have a very close lattice mismatch to the "a" substrate direction, i.e., $\Delta a/a = 0.37\%$ and 0.38%. However, they make a mismatch in the "c" direction of $\Delta c/c =$ 0.36% for $BaFe_{10.7}Al_{1.3}O_{19}$ and 0.83% for $BaFe_{9.3}Al_{12.7}O_{19}$. As indicated by Rinaldi et al.[29], since the "c" cell dimension is larger than 20 Å in the hexaferrites (corresponding to at least ten atomic layers), this mismatch will not be well compensated by strains or local defects such as dislocations. The large mismatch along "c" in $BaFe_{9.3}Al_{12.7}O_{19}$ films must contribute to form cracks, in contrast to the $BaFe_{10.7}Al_{1.3}O_{19}$ film.

Also, the terraced structure of the $BaFe_{9.7}Al_{2.3}O_{19}$ film shown in Figure 20a is probably caused by the combined effects of the slight misalignment of the substrate surface with respect to the "c" plane and the relatively large lattice mismatch. However, the important observation here is that the microstructure of films also depends on the film thickness as shown in the series of optical micrographs in Figure 20. Very smooth films of $BaFe_{9.7}Al_{12.3}O_{19}$ were grown up to 5 μm thickness even with their particular lattice mismatch.

38

(a) 40 μm thick

(b) 10 μm thick

(c) 5μm thick
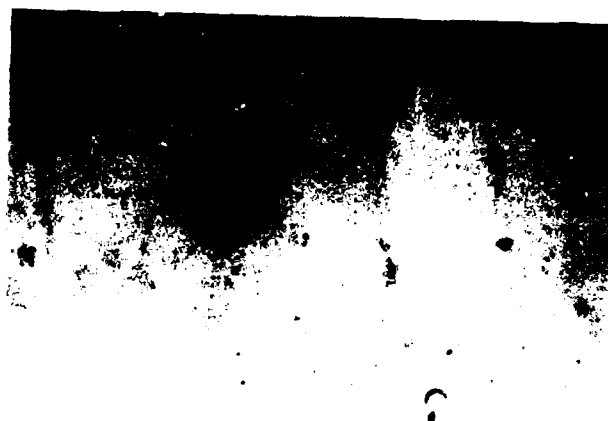
Figure 21 — Optical micrographs of $BaFe_{9.3}Al_{2.7}O_{19}$ films having film thicknesses of (a) 40 μm, (b) 10 μm, and (c) 5 μm.

It has been demonstrated that barium hexaferrite films of good quality can be grown from compositions in the Bi_2O_3-BaO-B_2O_3 flux system under conditions of good lattice mismatch between substrate and film. The lattice mismatch between substrate and film has been reduced by the substitution of Ga by In in cobalt gallate, V by Ta in barium vanadate, and Ga by Mg and Zr in the strontium hexagallate substrates. The substitution of Fe by Al in barium hexaferrite films is also very beneficial. The surface structures of the films grown in this program showed that relatively large lattice mismatches favor formation of large numbers of hexagonal islands and cracks. However, the Al-doped barium hexaferrite films of the best quality having topographically very smooth surfaces without cracks were grown by reducing the lattice matches to $\Delta a/a = 0.37\%$ and $\Delta c/c = 0.36\%$.

5. MAGNETIC MEASUREMENTS

The measurements reported on in this section fall into two to classes: those pertaining to the substrate materials and those used to evaluate the ferrite films per se. Although some results are reported in other sections of this final report, they will be included here also for the sake of completeness.

5.1 SUBSTRATE MEASUREMENTS

The measurements done on the substrate materials were primarily to assess two factors: (a) their possible magnetic influence on the epitaxial barium-ferrite due to a high magnetic moment or anisotropy field; (b) their suitability as substrate materials from a microwave point of view, specifically loss tangent and dielectric constant. The magnetization data were taken on approximately 1 mm square samples using the Faraday balance technique with a standard nickel value of 6083 gauss used as a reference value. The values of $4\pi M$ shown in Table 9 are the averages from two or three samples. All values are substantially less than the nominal 5000 gauss value for barium-ferrite and therefore should have little influence on the magnetic properties of the epitaxial films. In fact, all three substrate materials have magnetizations less than that of gadolinium gallium garnet, the conventional substrate material for yttrium iron garnet.

The dielectric constant and loss tangent data were measured with samples in the form of needles about 1 mm in cross section inserted into a microwave cavity resonant at 9 GHz. They were placed at electric field maxima positions in the cavity and thus the loss tangent data does not include any magnetic contributions. The values shown in Table 9 are again averages from two or three samples. The dielectric constant values are comparable to alumina and thus would pose no particular

problems in any microwave applications. Loss tangent values are about 20 times higher than that for alumina (tan δ = 0.0001) but are not felt to be excessive. The values would not preclude the materials being used at microwave or mm-wave frequencies.

Table 9

Electric and Magnetic Measurements of Three Substrates Studied

Material	Dielectric constant	Los tangent	Magnetization
	Er	tan δ	$4\pi M$
Sr-gallate	9.6	0.0019	-0.1
Co-gallate	9.2	0.023	+18.0
Ba-vanadate	12.0	0.0016	+3.8

5.2 BARIUM-FERRITE FERROMAGNETIC RESONANCE (FMR) MEASUREMENTS

FMR in barium-ferrite is complicated by the presence of a large uniaxial anisotropy field, and the "safest" way to get equations for the resonance data is from the free-energy expression. This avoids having to create heuristic anisotropy fields both ac and dc to analyze the experimental situation. Internal magnetic fields synthesized to account for crystal anisotropy appear naturally in the free-energy approach. Referring to Figure 22a, the free energy may be expressed as:

$$F = 1/2 \ (4\pi M^2 \cos^2\theta) - K_1 \sin^2\theta - H_0 M \ (\sin\theta \cos\varphi \sin\alpha + \cos\theta \cos\alpha),$$

where F is the free energy and K_1 the first order anisotropy constant.

The terms in the above equation from left to right are: the demagnetizing energy, the first order anisotropy energy, and the polar energy. We regard the magnetic field as fixed at some angle α to the z axis and obtain the equilibrium orientation of the magnetization M by equating the derivatives $dF/d\theta$ and $dF/d\varphi$ to zero. From these two

42
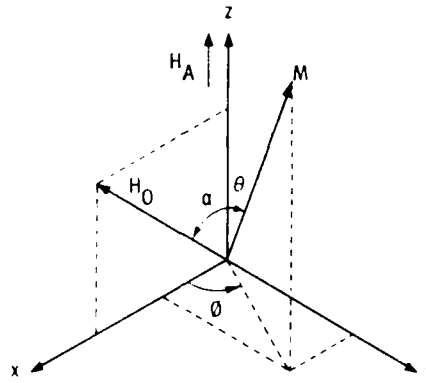
Figure 22a — Coordinate system for a thin platelet of Ba-ferrite
showing the static magnetization vector, M, under the
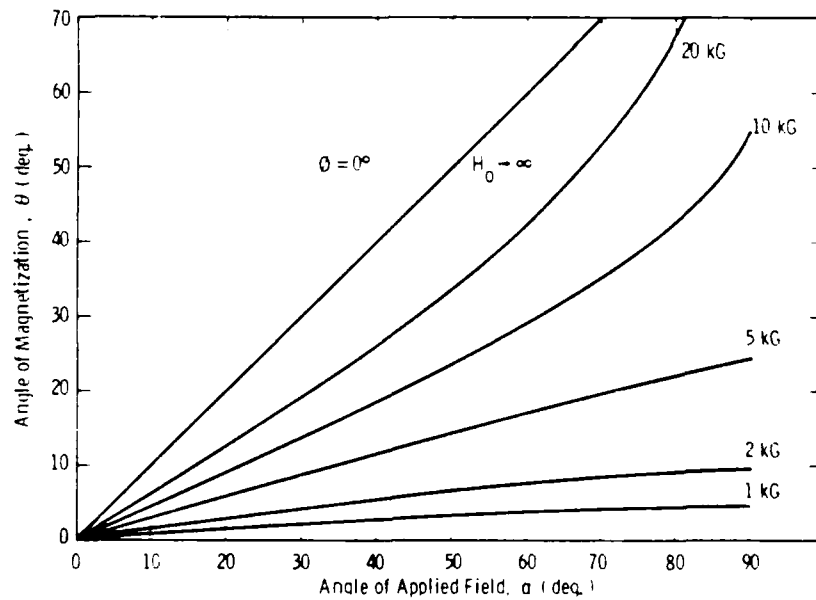influence of an external field, Ho, and a crystal
anisotropy field, Ha.

Figure 22b — The equilibrium orientation, θ, of the magnetization, M,
as a function of the applied field angle, α, with the
applied field strength as a parameter.

56

conditions we obtain (a) $\phi=0$, and (b) an equation for the equilibrium value of θ given below.

$$\sin\theta \cos\theta \ (2k_1/M - 4\pi M) \cdot Ho \ (\sin\theta \cos a - \cos\theta \sin a) = 0,$$

where Ha $2K_1/M$.

Figure 22b plots the equilibrium value of θ as a function of the applied magnetic field angle a. A number of facts emerge from the discussion so far. M, Ho, and Ha are always coplanar; however, they are only colinear for $a=0$. For $a=90°$, M and Ho are not colinear unless Ho equals or exceeds Ha-4πM.

FMR frequencies are given by the small angle precession frequencies of M about its equilibrium value of θ. This precession angle is obtained from the second derivatives of F with respect to θ and ϕ. In general there is no explicit expression for the FMR frequency, f, at a particular θ, a, and Ho and the equations below must be solved simultaneously.

$$Ha' \sin\theta \cos\theta \cdot Ho \sin (\theta - a) = 0$$

$$(f \ \gamma)^2 = (Ha' \cos 2\theta \cdot Ho \cos (\theta - a)) \ Ho \sin a \ \sin\theta,$$

where Ha$'$ = Ha 4πM and γ = 2.8 MHz/Oe.

Particular cases are of experimental interest:

(a) $a=0$, $f=\gamma$ (Ha-4πM-Ho);

(b) $a=90°$, Ho<Ha-4πM, $f=\gamma \ \sqrt{(Ha-4\pi M-Ho)(Ha-4\pi M-Ho)}$

(c) $a=90°$, Ho>Ha-4πM, $f=\gamma \ \sqrt{Ho(Ho-Ha-4\pi M)}$.

Figure 2a plots the applied field Ho as a function of its angle a for an FMR frequency of $f=50$ GHz, where for barium ferrite we put Ha 17 kOe and $4\pi M$ 4.8 kG. Figure 2b is a plot in plane ($a-90°$) and perpendicular resonance as a function of Ho.
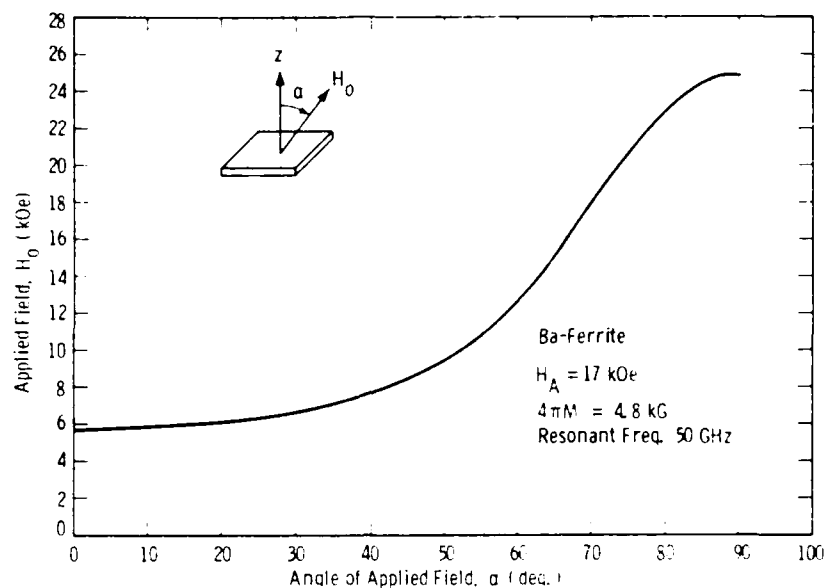
44

Figure 23a — The applied field strength as a function of its angle with respect to the z axis for FMR at 50 GHz. Bulk crystal values of Ha=17 kOe and 4πM=4.8 kG have been assumed.
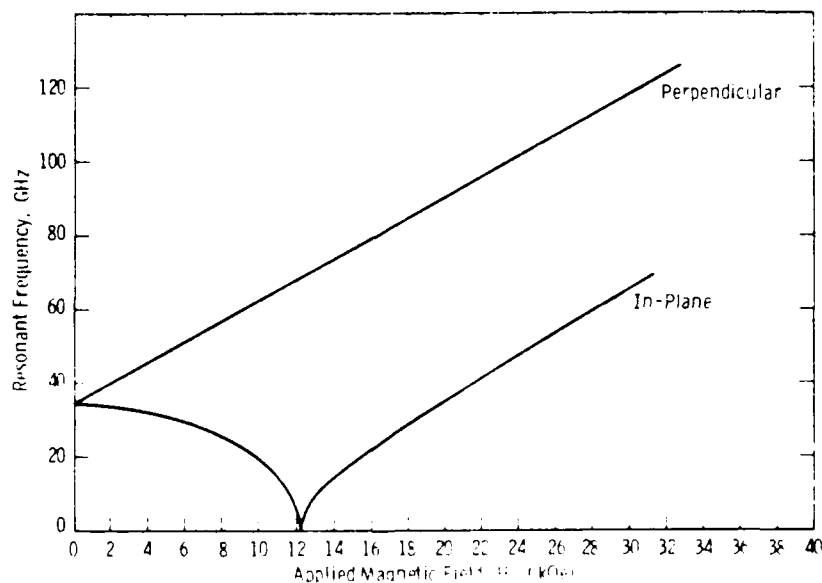

Figure 23b — The resonant frequency for FMR as a function of the applied field for Ho in the basal plane and perpendicular to it.

At the start of this program the FMR equipment consisted of a 9 GHz facility with an electromagnet capable of fields up to 10 kOe. From Figure 23b it is evident that no resonance would be observable in barium ferrite for any orientation of Ho. The first improvement to the test facility was to add tapered pole pieces to the electromagnet, leaving a central uniform field region in the air gap of the magnet. This enabled fields up to 13.8 kOe to be achieved before the magnet power supply capacity was exceeded. Hence, from Figure 23b, in-plane resonance should have been observable although not at an ideal part of the graph. Unfortunately, none of the samples examined showed an FMR response at this 9 GHz frequency. In fact, no resonance was observed even in a test sample kindly given to us by Bill Wilber (Department of the Army, Ft. Monmouth). This sample was known to be a high-quality, single-crystal platelet of barium-ferrite.

A second improvement in measurement was a move to a higher frequency; here two options were available. Samples were sent to Prof. Joe Artman at Carnegie-Mellon University (CMU), who kindly agreed to examine them in his resonant cavity FMR equipment at 33 GHz. As it turned out, this equipment was probably the most sensitive available to us and could detect FMR lines with widths in excess of 2 kOe. The second option was to use a recently modified Hewlett Packard 8409 network analyzer. The analyzer could provide waveguide transmission and reflection data from 26.5 to 40 GHz. A resonant cavity was constructed at 36 GHZ and its transmission parameter S21 observed with a small (1 mm square) sample placed at an rf H-field maxima in the cavity. The cavity was placed in a WR-28 waveguide structure with small holes or irises drilled at its end walls to provide weak coupling to the waveguide. Both in-plane and perpendicular resonance was looked for, although Figure 23b would suggest that only the perpendicular geometry was appropriate (albeit at a rather low applied field, which would most likely not magnetically saturate the sample). Whether this was true or whether the cavity had too low a Q value is unknown, but again no resonance was ever seen. Also, the test sample (barium ferrite sample C

batch #1) gave no results either. Thus all data reported below at Ka band were obtained from CMU at 33 GHz.

A final decision was made to concentrate on perpendicular resonance only and to establish an FMR facility at 50 GHz. This allowed us to use the fields obtainable from the existing electromagnet — up to 13.8 kOe. WR-19 waveguide, a 50 GHz Gunn diode oscillator, directional coupler, attenuator, circulator, and diode detector were all purchased from MA/COM of Burlington, Mass. The assembled pieces are shown in Figure 24 with the older 9 GHz equipment in the background. Samples glued on the end of a quartz rod were placed at an rf H-field maxima 5/2 wavelengths from the end of a shorted waveguide section. Using the field modulation technique and phase sensitive detection system of the 9 GHz rig, measurements were possible on samples with linewidths up to 500 Oesteds.

Figure 25a and 25b shows the results of measurements on the Ft. Monmouth test sample, Sample G Batch #1, where Figure 25a is a reproduction of the data kindly supplied by Bill Wilber. His results gave a linewidth of 17 Oe, whereas our value from Figure 25b was 20 Oe. We regard this as satisfactory agreement, particularly since our sample was broken during the mounting process and this damage may have broadened the linewidth. The main value of Figure 25 is that it confirmed the preparation of the 50 GHz equipment.

Figures 26, 27, 28, and 29 illustrate FMR results for several epitaxial films. Table 10 summarizes the data. Magnetically, great variability was found in the films; many films gave no resonance data. Those that did (Table 10) exhibited linewidths from over 2000 Oe wide to below 100 Oe.

The lowest main resonance linewidth measured was that for sample BFO 56, with a value of 94 Oe. However, an examination of Figure 29 shows evidence of line broadening due to multiple resonance, which we associate with the presence of large stresses due to lattice mismatch. In Figure 29 the linewidth of a secondary resonance marked by arrows is

47
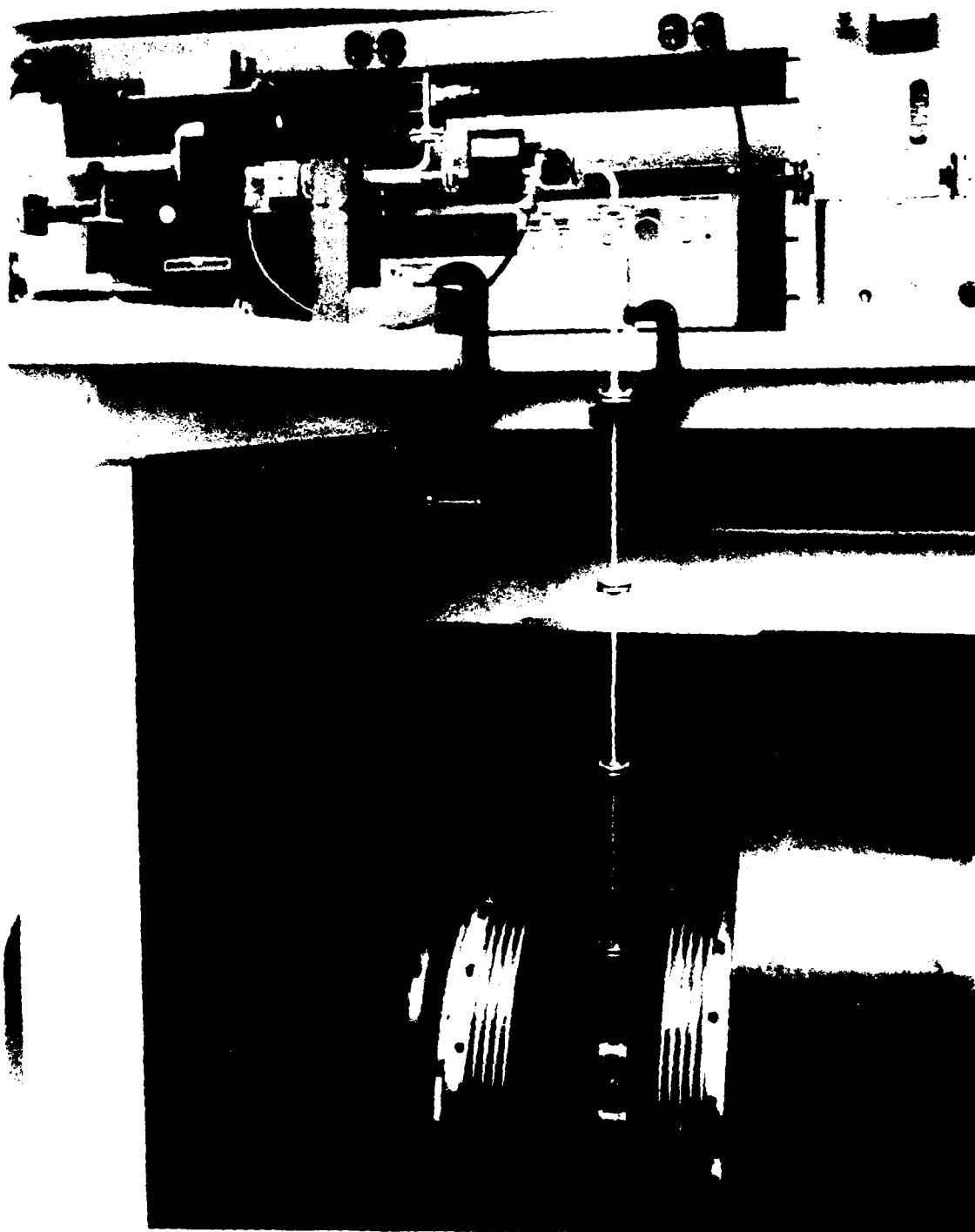
Figure 24 — A photograph of the equipment for the FMR measurements at
50 GHz. Some waveguide from the 9 GHz equipment is also
visible.
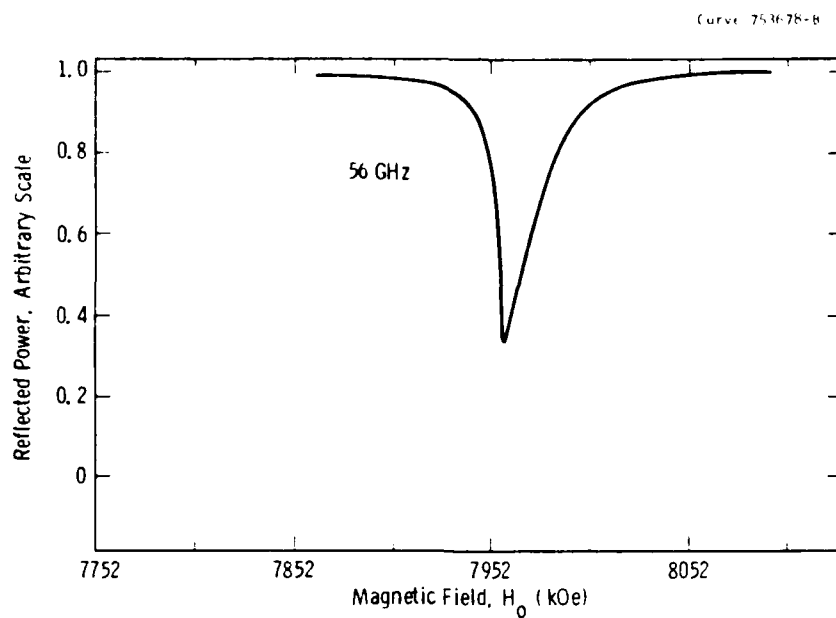
Figure 25a — Ft. Monmouth FMR data on the test sample Ba-ferrite sample
G batch #1.
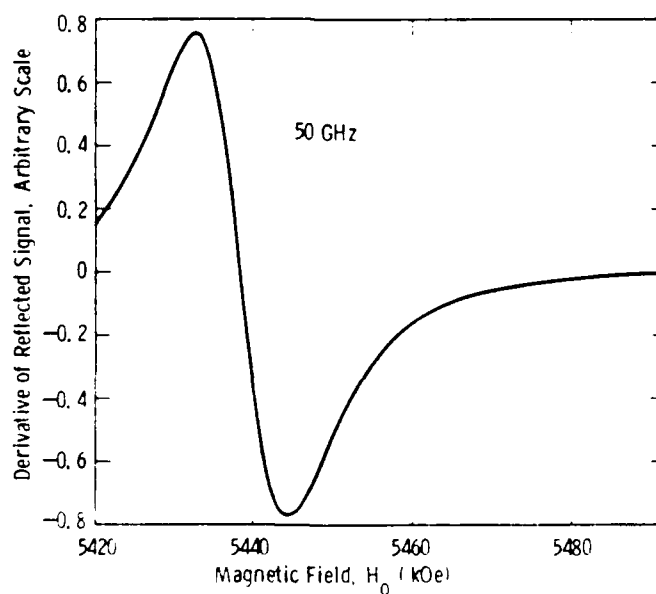
Figure 25b — Westinghouse data on the same sample but taken with a
field modulation technique which gives the derivative of
the FMR signal.
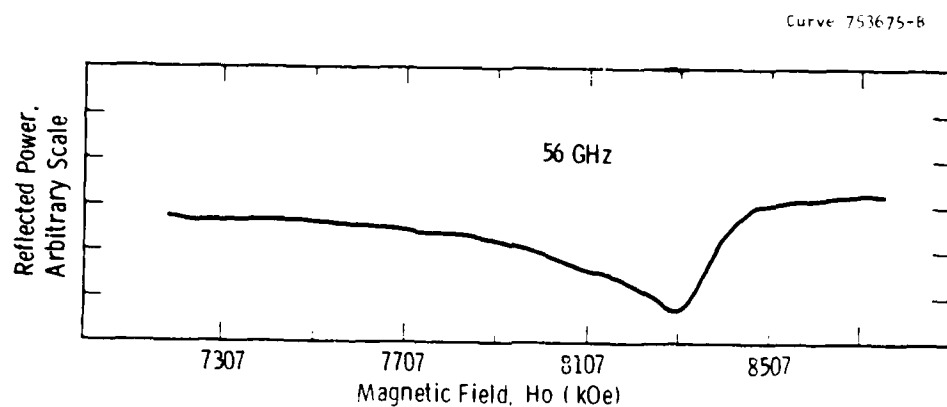
Figure 26a — Ft. Monmouth FMR data on sample BFO-5 with a Co-gallate substrate.
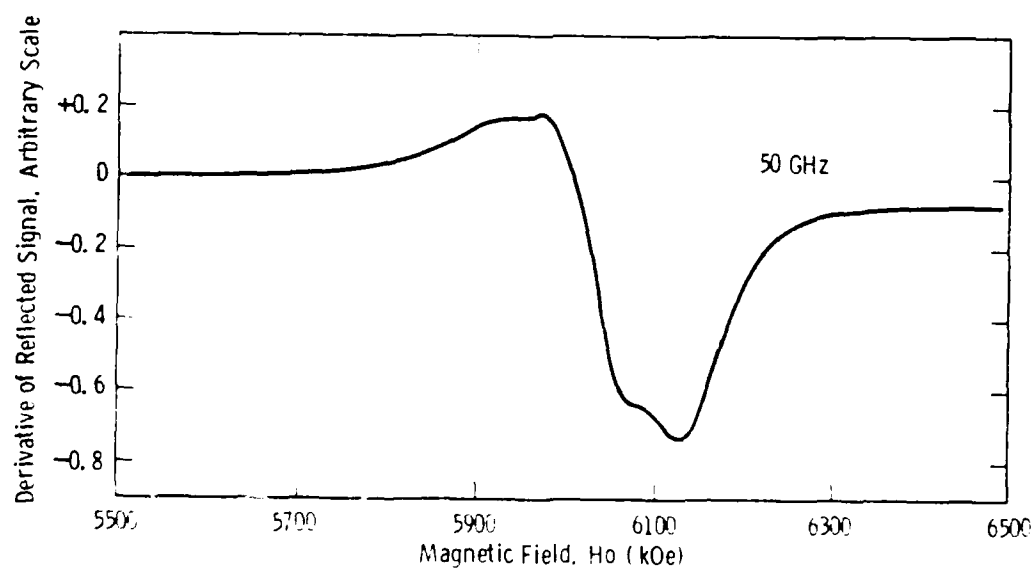
Figure 26b — Westinghouse data on the same sample.

56 GHz

Reflected Power, Arbitrary Scale

7487   7737   7987   8237   8487   8737

Magnetic Field, H_0 (kOe)
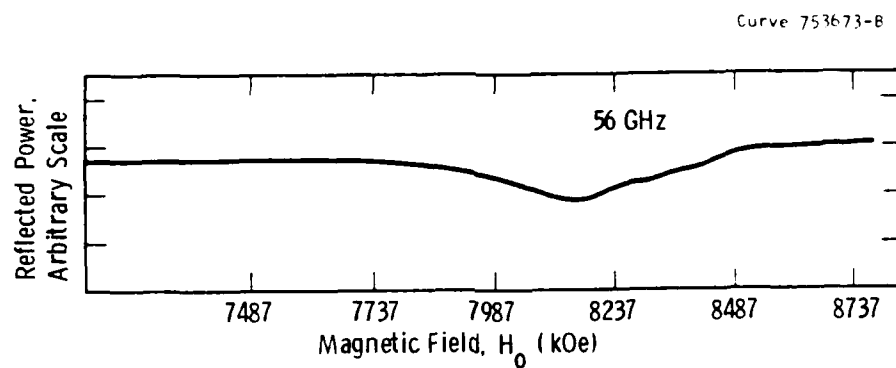
Figure 27a — Ft. Monmouth data on sample BFO-17 with a Co-gallate
substrate.

Derivative of Reflected Signal, Arbitrary Scale

50 GHz

0.4

0.2

0

−0.2

−0.4

5300   5500   5700   5900   6100   6300

Magnetic Field, H_0 (kOe)
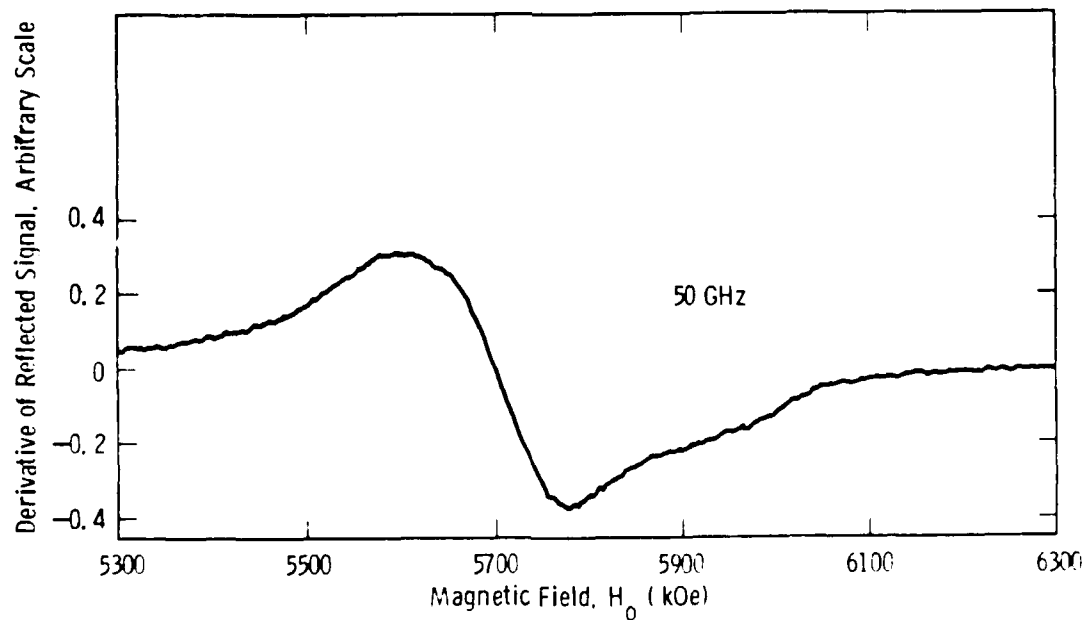
Figure 27b — Westinghouse data on the same sample.
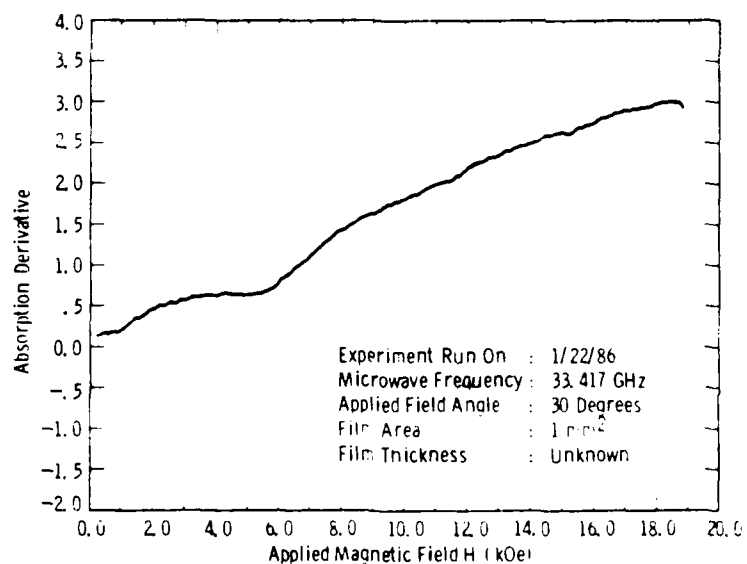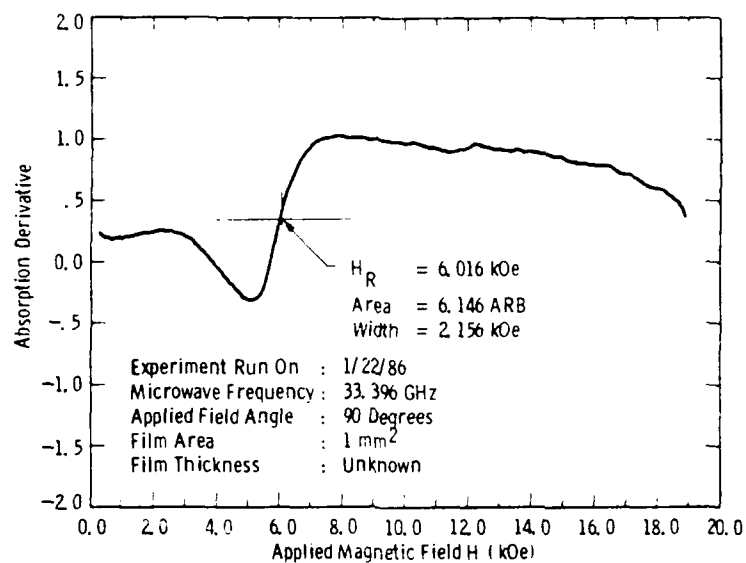
Figure 28 — Carnegie-Mellon data on sample BFO 19 with a doped Sr-gallate substrate, upper curve a light-colored sample and lower curve a dark-colored sample.

52
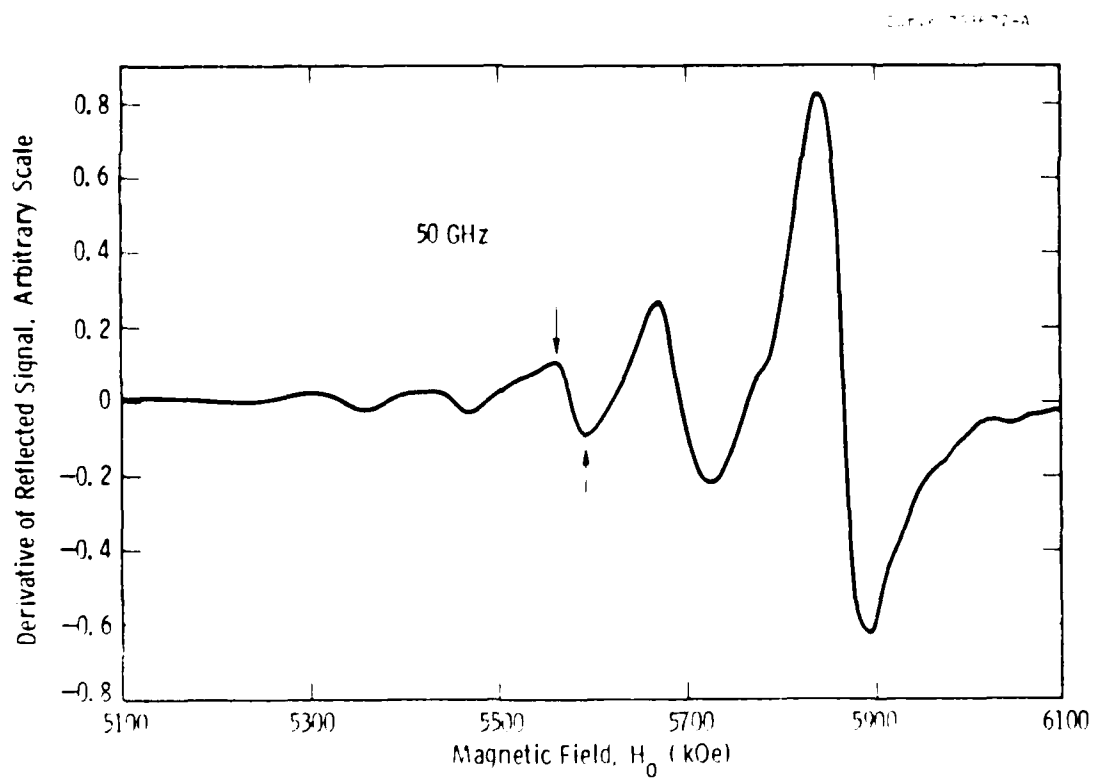
Figure 29 — Westinghouse data on sample BFO 56 with a doped Sr gallate substrate.

55 Oe, suggesting that the intrinsic quality of the barium ferrite is quite promising, but that lattice mismatch is sufficiently large to substantially degrade the overall film quality. This at a minimum substantially broadens the FMR linewidths and in some cases renders the films incapable of showing a measurable resonance.

In addition, the Al-doped films which had the lowest measured lattice mismatch would produce resonances out of the range of our current measuring capability. The conclusion here, therefore, is that barium-ferrite can be grown epitaxially on Co and Sr gallate substrates in a way which offers the promise of providing magnetically useful films. The presently used substrates, however, have too large a lattice mismatch, and this degrades the magnetic qualities of the films; further work is needed before the promise can be realized.

Table 10

Sample Substrate   Linewidth, Oe (Frequency, GHz & Field, Oe)

		CMU	Ft. Monmouth	W
BFO-5	Co-gallate	–	–	~280 (50 ~6000)
BFO-17	"	–	–	310 (50 5700)
BFO-19	Sr-gallate	>2000 (33.3 6000)	>1000 (99 10670)	–
BFO-56	"	–	–	94 (50 5780)
				35

6. SUMMARY AND RECOMMENDATIONS

Over 30 candidate compounds were surveyed to develop new substrates for ferrite epitaxial film growth. The goal was to identify materials with superior lattice match to the hexaferrite film, and which could be grown as large single crystals by the standard Czochralski crystal-pulling technique required ultimately to provide large wafer areas.

Two new substrate materials, cobalt gallate and barium vanadate, were identified, successfully grown as good-quality single crystals, and demonstrated to lattice match barium hexaferrite (with appropriate solid solution doping). Key physical properties of these materials, thermal expansion, cell dimension, dielectric constant, loss tangent, and optical transmittance, were measured and were found consistent both with epitaxial growth requirements, and with microwave and mm-wave application requirements. Studies of various compositions from which Mg, Zr-doped strontium hexagallate crystals could be grown were also carried out. This substrate, while not capable of lattice matching to pure barium hexaferrite, served as a baseline for the exploration of improved epitaxial flux systems.

All substrates were characterized in detail by optical and electron metallography, x-ray topography, x-ray diffraction analysis and electron microprobe analysis to assess chemical and structural homogeniety. Polished and characterized substrates were used to grow epitaxial hexaferrite films from a variety of flux systems by liquid phase epitaxy. The object of the studies was to identify flux systems that were chemically and thermally compatible with the substrates, and to define the range of growth conditions — temperature, undercooling, time and flux composition — for which good quality films could be formed. Flux systems tested included a new ternary flux, $BaO\cdot B_2O_3$ as

well as others previously described in the literature: PbO PbF$_2$, BaO B$_2$O$_3$, BaO BaF$_2$-B$_2$O$_3$, Bi$_2$O$_3$-B$_2$O$_3$BaO-V$_2$O$_5$, and Na$_2$O B$_2$O$_3$.

The best-quality films, those free from cracks, exhibiting smooth surface textures, and with low defect densities in x ray topographs, were produced under conditions of minimal substrate-film lattice mismatch. These were Al-substituted barium hexaferrite films grown on strontium hexagallate which yielded lattice mismatchs of about 0.4%. Slightly textured films were grown on cobalt gallate, but flux-substrate reaction and film interdiffusion limited epitaxy on the Ta-substituted barium vanadate substrates. The best film growth was obtained using Bi$_2$O$_3$-based fluxes, in particular the newly developed BaO-Bi$_2$O$_3$-B$_2$O$_3$ flux.

A system to measure ferromagnetic resonance (FMR) at frequencies up to 50 GHz was assembled and used to characterize the magnetic properties of the epitaxial films. This system was calibrated with a high-quality piece of bulk barium ferrite kindly supplied by W. Wilber of Fort. Monmouth. In addition to our tests, supplementary measurements of films were carried out at Ft. Monmouth and by Prof. J. Artman at Carnegie Mellon University.

The best FMR linewidth values were 55 Oe for films on strontium gallate, and 280 Oe for films on cobalt gallate. In general, however, the FMR linewidths of the films were broadened ranging from ~ 2000 Oe to values below 100 Oe. The broadened linewidths are attributed to the difficulty in growing truly lattice-matched films and, in the case of ferrite on cobalt gallate, to some interdiffusion between the film and the substrate (Appendix I) (we could not measure the linewidth of the Al-substrated films with our equipment).

Significant improvements in both substrate materials and epitaxial techniques have been made during this study. However, to take full advantage of the new substrate materials requires either an alternative to liquid phase epitaxy or lower temperature, less reactive fluxes to eliminate the film substrate interactions we observed.

Alternative approaches include: 1) compositional modifications of current LPE fluxes to lower the growth temperature; 2) further development of new fluxes to reduce substrate-flux reactivity; 3) the use of buffer layers to reduce flux attack of the substrate; or 4) the application of other film deposition techniques, such as sputtering or ferrite plating, which avoid fluxes.

Films with linewidths as low as 55 Oe were grown on strontium gallate despite some degree of lattice mismatch. Further improvements in linewidth could be gained by refinements to better match strontium gallate to barium ferrite. For example, other dopants, such as scandium, might be employed to further increase the cell dimension of strontium gallate. Alternatively, the growth of intermediate layers of higher cell dimension on strontium gallate could be used as a transition structure to bring the gallate and ferrite lattices into registry.

Our studies indicate that ferrite epitaxy is still very promising for mm-wave device applications, and that focused research can bring clear improvements in the substrate and film technology. We have defined directions for further studies which should lead to improved resonance linewidths required for eventual systems applications. We believe such studies are warranted and should be carried out.

7. ACKNOWLEDGEMENTS

8. REFERENCES

1. W. H. von Aulock, ed., Handbook of Microwave Ferrite Materials, Academic Press, NY.

2. R. O. Savage et al., J. Appl. Phys., 36: 873 (1965).

3. R. O. Savage and A. Tauber, J. Am. Ceram. Soc., 47: 13 (1964).

4. A. Tauber et al., J. Appl. Phys., 41: 1353 (1970).

5. S. Dixon et al., J. Appl. Phys., 41: 1357 (1970).

6. S. Dison et al., J. Appl. Phys., 42: 1732 (1971).

7. A. J. Kevecman et al., J. Appl. Phys., 40: 1416 (1969).

8. H. L. Glass and J. H. W. Liaw, J. Appl. Phys., 49: 1578 (1978)

9. F. S. Stearns and H. L. Glass, Mat. Res. Bull., 10: 1255 (1975).

10. F. S. Stearns and H. L. Glass, Mat. Res. Bull., 11: 1319 (1976).

11. H. L. Glass and F. S. Stearns, IEEE Trans. Mag., MAG 13: 1241 (1977).

12. H. L. Glass, "Epitaxial Hexagonal Ferrites for MM Wave Tunable Filters," Final Report ARO Contract DAAG 29-80-C-0150, December 1982.

13. F. Haberey et al., Naturwissenschaften, 66: 617 (1979).

14. F. Haberey et al., Mat. Res. Bull., 15: 493 (1980).

15. F. Haberey et al., J. Crystal Growth, 52: 734 (1981).

16. F. Haberey et al., J. Crystal Growth, 61: 284 (1983).

17. F. Haberey et al., IEEE Trans. Mag., MAG 16: 681 (1980).

18. G. Bartels et al., J. Crystal Growth, 47: 414 (1979).

19. P. J. M. Van Der Straten and R. Metselaar, J. Crystal Growth, 48: 114 (1980).

20. J. A. Kohn et al., _Science_, 172: 514 (1971).

21. D. Mateika and R. Laurien, _J. Crystal Growth_, 52: 566 (1981).

22. D. Mateika and H. Laudan, _J. Crystal Growth_, 46: 85 (1979).

23. Ibid., pp. 85-90 (1979).

24. D. Mateika and R. Laurien, ibid., pp. 566-575 (1981).

25. V. P. Kobzarera, L. M. Korba, L. M. Lopato, L. N. Lykora, and V. Sheuchcuko, _Russian J. of Inorganic Chemistry_ 21(6) (1976).

26. W. E. Kramer, A. M. Stewart, and R. H. Hopkins, _J. Crystal Growth_, 73: 329-336 (1985).

27. W. E. Kramer, A. M. Stewart, and R. H. Hopkins, "The Growth of $Ba_3(VO_4)_2$ Simple Crystals as Substrates for the Epitaxial Growth of Ferrites," to be published.

28. K. C. Yoo, R. P. Storrick, W. E. Kramer, A. M. Stewart, and R. H. Hopkins, "Investigation of Growth Conditions for Liquid Phase Epitaxy Hexaferrite Films using Bi_2O_3-BaO-B_2O_3 Flux," to be published.

29. S. Rinaldi and F. Licci, _IEEE Trans. on Mag._, MAG-20(5): 1267 (1984).

Appendix I

THE GROWTH OF CoGa$_2$O$_4$ SINGLE CRYSTALS AS SUBSTRATES FOR THE EPITAXIAL GROWTH OF FERRITES

W.E. KRAMER, A.M. STEWART and R.H. HOPKINS

Westinghouse R&D Center, Pittsburgh, Pennsylvania 15235, USA

We report here initial studies to develop a lattice-matched substrate material for epitaxial ferrite growth. Single crystals of CoGa$_2$O$_4$ have successfully been grown by Czochralski pulling and characterized with respect to lattice dimension, thermal expansion, dielectric constant and loss tangent. Epitaxial lithium ferrite films have been grown to demonstrate the potential for epitaxy.

1. Introduction

In today's military systems, single and poly-crystalline garnet or spinel ferrites find widespread use as tunable microwave filters and resonators in applications ranging from test equipment to radar and ECM systems. They are also used as nonlinear devices and are employed extensively in microwave systems as circulators, isolators, and phase shifters.

For these applications, systems operating at higher frequency offer wider bandwidths, narrower beamwidths for a given antenna size, smaller size and lighter weight than their microwave counterparts. However to operate magnetic devices close to resonance at such high frequencies requires large magnetic bias fields when materials with small internal anisotropy fields like garnets are used. These bias fields are not easily attainable with compact permanent magnets or electromagnets.

In contrast, hexagonal ferrites with large anisotropy fields (e.g. 17 kg for BaFe$_{12}$O$_{19}$) can operate close to resonance at mm-wave frequencies with small fields of 1-5 kg. spinel ferrites can be used at lower frequencies. Thus, devices based on films of these materials may match future needs for small, low-cost mm-wave ferrite crystal components, tunable filters, and oscillators.

This paper reports on CoGa$_2$O$_4$, a congruently melting spinel compound which appears attractive for the epitaxial growth of both lithium ferrite and the hexagonal ferrites. We have successfully grown 111-oriented single crystals of CoGa$_2$O$_4$ by Czochralski pulling and have demonstrated the epitaxial growth of lithium ferrite layers on it.

2. Experimental

2.1. Synthesis

CoGa$_2$O$_4$ is reported [1] to have a spinel structure $a = 8.32$ Å. The material was synthesized by blending powders of the oxide constituents weighed to stoichiometric proportions and reacting them at high temperatures. The product was tested by X-ray powder diffraction analysis (monochromatic Cu K$_\alpha$ radiation, Philips APD 3600 System). The material was melted in an iridium crucible and crystallized. The temperature was monitored pyrometrically and a freezing point of 1825 ± 5 °C was measured. A portion of the melt was removed for X-ray powder diffraction and a lattice parameter of 8.32 ± 0.004 Å was determined.

2.2. Float zone growth

CoGa$_2$O$_4$ is deep blue in color indicating the presence of strong optical absorption bands in the
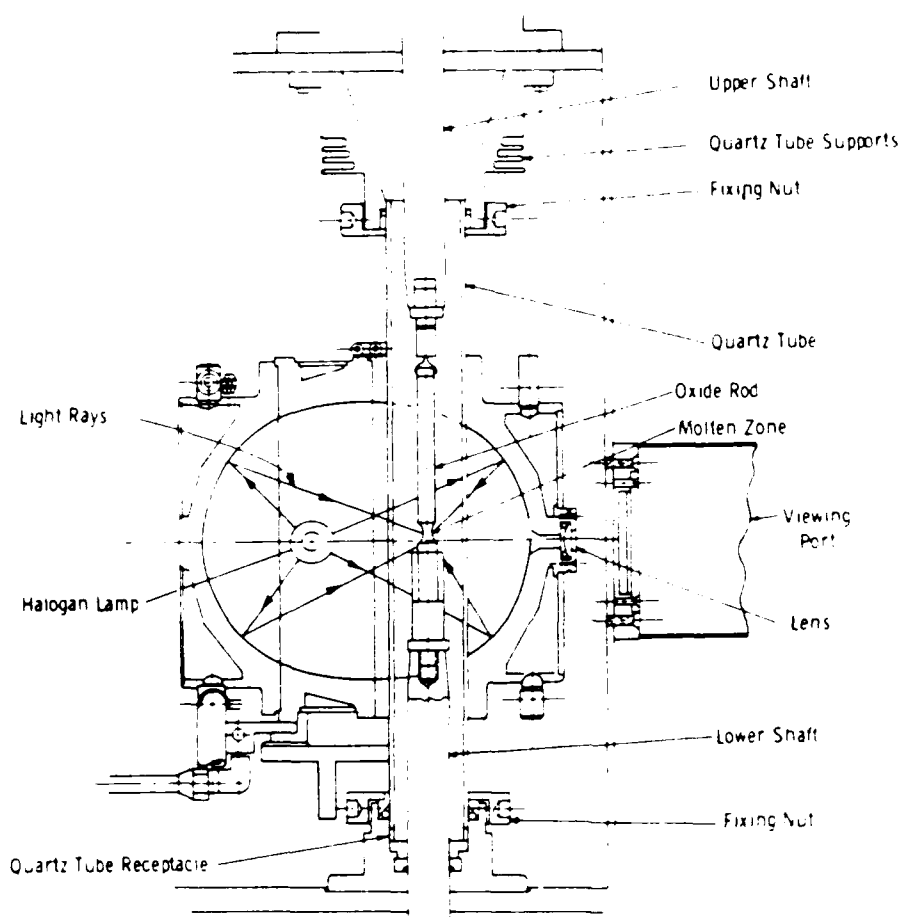
Fig. 1. Focussed light float-zone crystal growth system. Crystals can be grown for evaluation without crucible contamination and under a controlled atmosphere.

visible and near infrared spectral region. This property was used to advantage in exploratory growth studies using a focussed light float-zone crystal grower, pictured schematically in fig. 1, to produce crystals.

CoGa₂O₄ powder pressed and sintered into a cylindrical feed rod was melted by imaging on it the energy from a tungsten-iodine lamp. The polycrystalline feed rod was recrystallized by moving the molten zone upward along it (lowering the rod). When a single-crystal seed was used to initiate freezing, small centimeter-diameter crystals of CoGa₂O₄ were produced.

The advantages of this approach are the small amount of material required (a feature which facilitates survey work), the freedom from crucible contamination, and the ability to control carefully the furnace atmosphere if necessary to maintain oxide stoichiometry or valence state. Crystals are, however, limited in size because it is difficult to maintain a large stable molten zone of dense liquid oxide.

The results of the float-zone studies verified that single-phase CoGa₂O₄ single crystals could be grown and that the cell dimension of the crystal was close to that of the polycrystalline feedstock

Growth rates in the range 1 to 5 mm h were employed and a gas ambient containing a few percent of oxygen appeared necessary to suppress the formation of volatile suboxides of gallium These crystals are, however, too small in diameter for direct device application.

2.3. Czochralski crystal growth

Crystal growth from the melt by the Czochralski process is the preferred technique for the production of large-diameter, low defect density crystals Crystal growth is achieved by dipping an oriented crystal seed into a container of the melted oxide compound Cobalt gallate crystals were grown at 1 to 6 mm h and rotated at 20 to 50 rpm to assure thermal symmetry.

Cobalt gallate melts at 1825°C so that iridium metal crucibles (MP 2450°C) are used to hold the molten oxide during crystal growth The crucible-refractory geometry is illustrated in fig. 2 The crucible, insulated by crushed zirconia ceramic, is surrounded by a zirconia crucible A ceramic lid rests on top of the zirconia crucible To adjust the system thermal gradient, the height l of the lid above the melt is varied by inserting sleeves of different thicknesses between it and the crucible Not shown in the sketch is a water-cooled induction coil which surrounds the crucible and refractory and provides power for melting the oxide by coupling energy from a 10 kHz generator directly into the crucible. Two types of furnaces, conventional and pressurized, as well as different refractory crucible configurations, were employed to identify appropriate growth conditions for cobalt gallate The main differences between the conventional and the pressurized furnace is that in the latter, the melt, crucible, and refractories are maintained in a stainless steel enclosure operated at internal pressures up to 20 atm (300 psi) We found that overpressure significantly reduced the evaporation rate of cobalt gallate from the melt

2.4. Crystal growth results

Initial studies in the conventional puller, which employed a ceramic pull rod and ceramic lid located close to the melt surface, were hampered
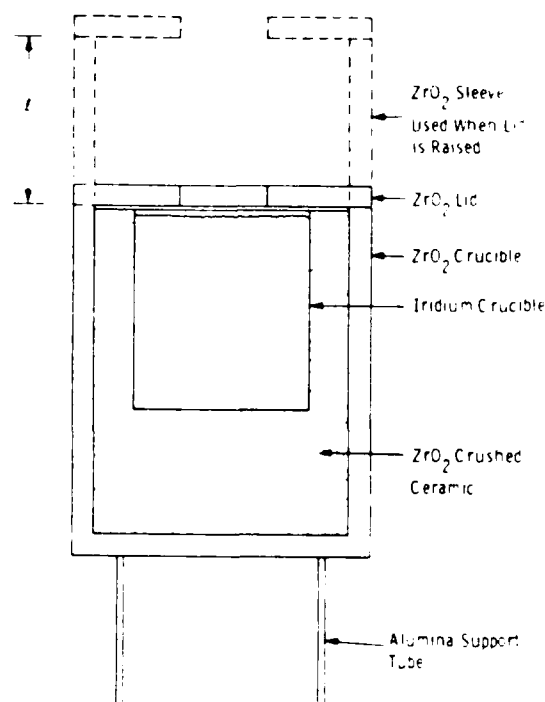
Fig. 2. Details of crucible refractory and support system for CoGa₂O₄ growth This assembly was inserted inside conventional or pressurized growth furnaces

by two difficulties. The solid-liquid interface was concave under most conditions of pull and rotation rate, and a significant loss of cobalt gallate from the melt by evaporation was noted. The former condition made diameter control difficult, so that crystals tended to grow suddenly outward or terminate by abrupt melting off. Because the evaporated oxide made deposits on the under surface of the lid, gallate particles often fell back into the melt, causing new crystallites to grow on the melt surface which interrupted crystal growth.

To minimize melt evaporation further studies were transferred to an ADL Model MP pressure puller. It was found that overpressures of 50 psi significantly reduced the loss of cobalt gallate from the melt during growth. In general, under these conditions we found empirically that slow growth and rotation rates coupled with the use of a water-cooled pull rod and the positioning of the top lid 2 to 3 inches from the melt surface led to

crystal–liquid interfaces that were flat to convex and to improved diameter stability. Crystals up to 2.5 cm long by 1 cm in diameter were grown.

Samples from these crystals were employed to characterize the lattice parameter, thermal expansion coefficient, optical transmittance, and dielectric properties of cobalt gallate. Slices from these crystals were used to carry out liquid-phase epitaxial growth studies.

3. Physical properties

Several of the crystal properties of $CoGa_2O_4$ were measured to characterize the suitability of the material as a substrate for the epitaxial growth of cubic lithium ferrite or the hexaferrites.
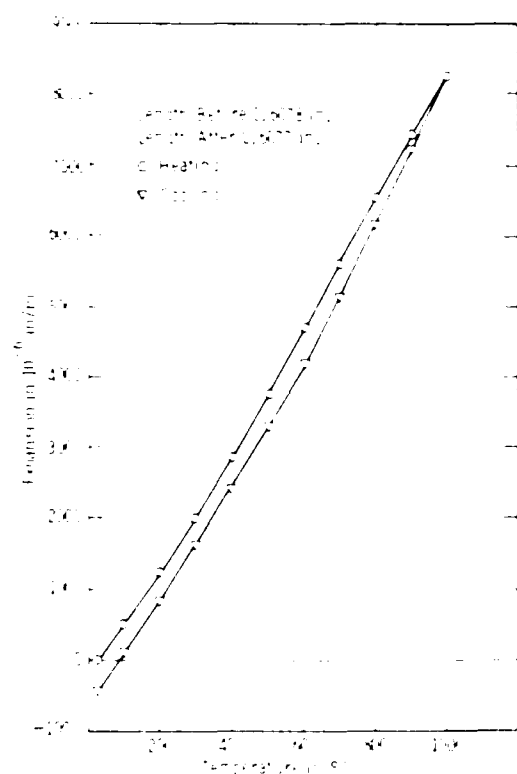
3.1. Cell dimension

For epitaxy the substrate and film lattice dimensions should be closely matched. The cell dimension or lattice constant of a powdered $CoGa_2O_4$ crystal was measured using Cu Kα radiation on a Philips APD 3600 automated powder diffractometer. The data from reflections were indexed automatically and a least squares refinement was completed using the software package associated with the diffractometer. We found a value of $a = 8.323 \pm 0.005$ Å in fair agreement with the value for the melted polycrystalline material. This value falls below the ideal 8.336 Å value required to match lithium ferrite or the hexaferrites.

3.2. Thermal expansion constant

To minimize thermally induced strains during cooling of the film–substrate composite from the film growth temperature, the thermal expansion difference between the two components should be small. Fig. 3 illustrates the thermal expansion of a cylindrical $CoGa_2O_4$ single-crystal test piece 15 mm long × 7.6 mm in diameter. The data representing the temperature interval from 20 to 1000°C were collected with a quartz tube dilatometer.

The measured average thermal expansion coefficient for $CoGa_2O_4$, about 9×10^{-6} °C⁻¹ depending on the temperature, is comparable to that for gadolinium gallium garnet and smaller than the value of 12×10^{-6} °C⁻¹ for lithium ferrite between 0 and 700°C. The hysteresis exhibited in fig. 3 may be an artifact of the measurement or could indicate that some cracking developed in the sample during testing.
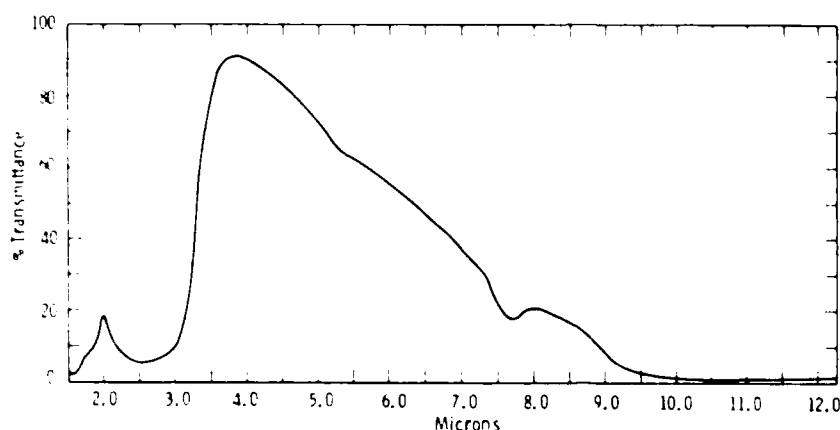
Fig. 4. Optical transmittance of CoGa₂O₄ crystal from 1.5 to 12 μm.

3.3. Dielectric constant

Rectangular rods of CoGa₂O₄ approximately $1.15 \times 0.7 \times 14.1$ mm in size were attached to alumina rods using Duco cement. Their dielectric constant and loss tangent were measured using the ASTM method "Complex Dielectric Constant of Non-Metallic Materials (C525)", which is a microwave cavity perturbation technique. Results obtained for three different samples are shown in table 1.

The relative permittivity value of about 9.2 is comparable to values for other nonmagnetic insulators like alumina or gadolinium garnet. The tan δ_e values of 0.0015 to 0.003 are significantly above the goal of < 0.001 desired for a millimeter-wave ferrite in order to minimize device losses. Further improvement in crystal quality is expected to lower the current tan δ values into the acceptable range.

3.4. Optical transmittance

At high temperatures radiation is a dominant heat loss mechanism during crystal growth, so that the optical properties of a material can strongly influence the control of the crystal growth process. To gain insight into the causes for erratic diameter control and the concave solid-liquid interface shape observed in many of our initial experiments, we measured the optical transmittance of a 0.425 mm thick CoGa₂O₄ crystal slice. The slice was

optically polished prior to the measurements, which were taken in a Perkin-Elmer 330 spectrometer.

The transmission spectrum between 0.3 and 1.5 μm is virtually featureless, showing almost no transmission at any wavelength except between 0.7

Substrate and epitaxial layer
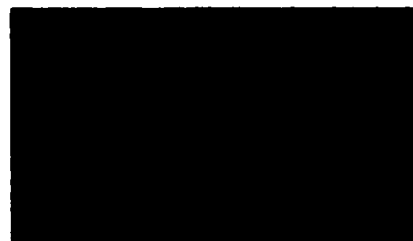
Fig. 5. Lithium ferrite epitaxial films grown from PbO-B₂O₃ flux on CoGa₂O₄ single-crystal substrates. Large marks on substrate peripheries are from the Pt fingers which hold the wafer during dipping.
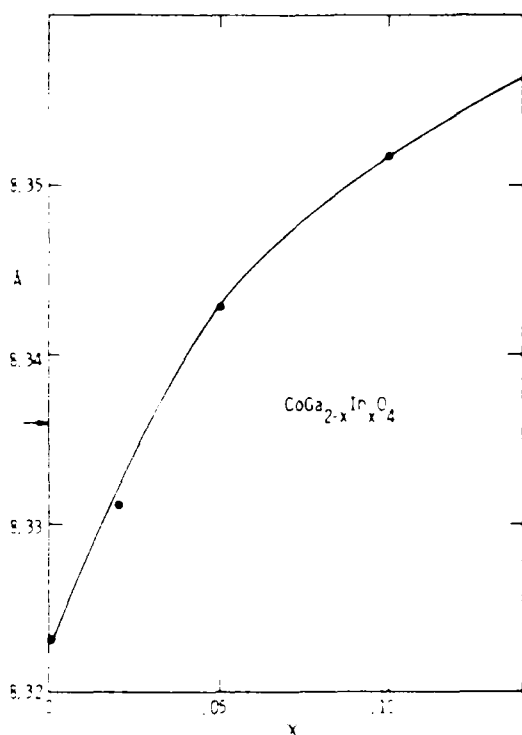
Fig. 6. Lattice parameter versus composition for $CoGa_{2-x}In_xO_4$. Arrow denotes cell size for matching to lithium ferrite.

perature and the substrate is inserted below the melt surface. The substrate, while being rotated in a horizontal plane, is held in the melt for a fixed time period during which the film grows. Our films are typically 5 to 20 μm thick for growth times in the range 25 to 100 min.

Lithium ferrite layers (fig. 5) up to 15 μm thick, grown on $CoGa_2O_4$, are relatively smooth and terrace-free. Although some cracking in the sub-state near the film-substrate interface took place in the first runs, no film flaking was observed. Cracking in these first films depends on one or more factors: (1) the cell dimension of undoped $CoGa_2O_4$ is slightly smaller than that of lithium ferrite, (2) there is a slight thermal expansion mismatch between the ferrite and gallate, and (3) the epitaxial growth conditions are as yet unoptimized.

An ideal lattice match for lithium ferrite would require an increase of the $CoGa_2O_4$ lattice from 8.323 A. This can be accomplished by solid solution doping. A study of the lattice parameter as a function of indium substitution in the system $CoGa_{2-x}In_xO_4$ was made by powder synthesis. At $x = 0.03$ a good lattice match for lithium ferrite is obtained (fig. 6). Future growth experiments will assess the growth of solid solution crystals.

and 0.9 μm, where the transmission rises to 50% (0.8 μm) and then falls back to zero. The spectrum between 1.5 and 12 μm is illustrated in fig. 4. Again, the material transmits relatively poorly except for a window between about 3 and 5 μm.

3.5. Liquid phase epitaxy

The degree of substrate to film matching required for good epitaxy is comparable for lithium ferrite and barium ferrite. Because lithium ferrite film growth is currently more advanced, the potential of the $CoGa_2O_4$ substrates was tested by growing lithium ferrite films on them.

The lithium ferrite is dissolved in a flux composed of PbO and B_2O, until saturation is achieved for temperatures in the range 750 to 850 C (depending on the melt composition) [3]. The melt is undercooled about 30 C below the saturation tem-

4. Discussion

Some of the difficulties in growing $CoGa_2O_4$ can be understood in the context of system heat flow. During growth, heat is carried to the crystal by conduction from the melt in which it grows, from the latent heat of crystallization, and also by radiation from hot surroundings such as the melt or crucible. Heat is dissipated through the crystal by conduction and lost from the crystal surface and top by radiation and by convection to the gas phase. At steady state, these flows are in balance and the crystal grows with a constant diameter.

At slow growth rates (common for oxide materials) the Biot number H, roughly the ratio of heat dissipated from the crystal surface to that conducted axially through the crystal, characterizes the heat transfer in the crystal. Metals with their low emissivities and high thermal con-

ductivity typify low Biot number materials, while oxides exhibiting low thermal conduction might be expected to exhibit high Biot numbers.

Both mathematical simulation and empirical results suggest that high Biot number materials will exhibit concave solid liquid interfaces [4] and unstable diameter control due to radiative interaction with the surroundings.

In fact, most transparent oxide crystals grow with convex interfaces unless very high crystal rotation rates are applied. The reason is that heat transport is dominated by radiation through these transparent high melting point materials (sapphire, yttrium aluminum garnet, gadolinium gallium garnet, etc.), giving them a very high effective thermal conductivity. The ratio of lateral to axial heat loss is low and the effective Biot number is correspondingly small. However the addition of a strongly absorbing species to the crystal reduces its transparency (lower effective conductivity) and raises its emissivity, resulting in the behavior expected for a high Biot number material.

This is the situation for $CoGa_2O_4$, where the transmittance of the material over all but a narrow window between 3 and 8 μm is nearly zero. At the melting point of $CoGa_2O_4$, 1825°C, the peak of the black body spectrum is 1.35 μm and 80% of the radiation energy falls at wavelengths below 3 μm. Thus, we expect that a substantial portion of the radiation reaching the crystal will be absorbed and reradiated rather than transmitted. (A similar situation exists for Dy doping in yttrium aluminum garnet [5].)

Modification of the gallate optical properties thus explain its tendency to form a concave interface and to exhibit diameter instabilities. The latter occur when small protrusions form on the crystal surface which enhance radiative heat loss. Since the crystal is a poor thermal conductor, attempts to control its rapid diametral expansion by raising the melt temperature often cause the sudden melt-off of the crystal.

The concavity of the interface can be reduced by:

(1) employing an after heater or radiation shield,
(2) using a larger crucible,
(3) decreasing the growth rate,
(4) reducing the rotation rate.

Items 1 and 2 lead to improved diameter stability by favorably modifying the radiative view factor for the crystal surface. Utilizing these methods, we have improved the stability of growth leading to the crystals described in this paper.

The preliminary experiments in the liquid phase-epitaxial growth of lithium ferrite on $CoGa_2O_4$ indicate that aside from lattice mismatch, the gallate is a good substrate for ferrite epitaxy. Layers of controlled thickness could be grown with negligible attack of the substrate. However, a better lattice parameter match is required.

5. Conclusion

$CoGa_2O_4$ is a promising substrate for the liquid-phase epitaxial growth of ferrites for future mm-wave devices. Liquid-phase epitaxy of 15 μm thick lithium ferrite films has been demonstrated.

The crystal growth of $CoGa_2O_4$ is complicated by the strong visible and near infrared absorption bands attributable to Co doping in the gallate lattice. Modifications to the growth system coupled with slow growth and rotation rates have produced crystals up to a centimeter in diameter and 2.5 cm long, and further optimization of growth conditions should lead to larger crystals.

The lattice parameter and thermal expansion coefficients of $CoGa_2O_4$ are in a range compatible with epitaxial growth. Some doping of $CoGa_2O_4$ to increase its cell dimension is required to improve lattice matching to lithium ferrite. Indium is a suitable dopant for this modification.

Although the permittivity of $CoGa_2O_4$ is suitable for mm-wave devices, further reductions in loss tangent will be required to make low-loss devices. These are expected to be obtained from improvements in crystal quality.

References

[1] A. Tauber, J.S. Merth and J.R. Shappirio, J. Appl. Phys. 41 (1970) 1383.

[2] H.L. Glass, Final Report, ARO Contract DAAG-29-80-C-0180, Dec. 1982.

[3] H.L. Glass and H.W. Liaw, J. Appl. Phys. 49 (1978) 1578.

[4] N. Kobayashi, in: Preparation and Properties of Solid State Materials, Vol. 6, Ed. W.R. Wilcox (Dekker, New York, 1981) p. 126.

[5] B. Cockayne, M. Chesswas and D.B. Gasson, J. Mater. Sci. 4 (1969) 450.

Appendix II

The Growth of $Ba_3(VO_4)_2$ Single Crystals as Substrates for the Epitaxial Growth of Ferrites

W. E. Kramer, A. M. Stewart, and R. H. Hopkins
Westinghouse R&D Center, 1310 Beulah Road, Pittsburgh, PA   15235

ABSTRACT

A novel substrate material for the epitaxial growth of ferrite layers is presented. Single crystals of barium vanadate $(Ba_3(VO_4)_2)$ and tantalum-substituted $Ba_3(VO_4)_2$ have been grown by the Czochralski growth technique. The crystals were characterized with respect to lattice constant, thermal expansion, hardness, dielectric constant, and loss tangent.

1. INTRODUCTION

Hexagonal ferrites with large anisotropy fields can operate close to resonance at mm-wave frequencies. Since these materials are difficult to grow as high-quality single crystals and then to shape for devices, thin-film ferrite growth on a lattice-matched substrate provides an attractive approach for mm-wave applications. Devices based on these films can be used as the crystal components in tunable filters and oscillators.

A number of substrates have been reported for epitaxial ferrite growth, among them Mg- and Zr-substituted $SrGa_{12}O_{19}$.[1] In many cases, film quality had been restricted by imperfect lattice matching or chemical incompatibility with these substrates.

We report the growth of a new material, $Ba_3(VO_4)_2$, a congruent compound that can be lattice-matched to barium hexaferrite by replacing vanadium with tantalum.

2. EXPERIMENTAL

2.1 SYNTHESIS

Barium vanadate $(Ba_3(VO_4)_2)$ was synthesized by weighing stoi-
chiometric portions of barium carbonate and vanadium oxide, blending in
a mechanical mixer, and firing the powders at 600°C for 12 hours. The
product was tested for completeness of reaction by x-ray powder diffrac-
tion analysis using a Philips APD 3600 system. The fully reacted
material was then melted in an iridium crucible and crystallized. The
freezing point measured with an uncorrected optical pyrometer was 1625 ±
10°C.

2.2 CRYSTAL GROWTH

The sharply defined melting point and lattice parameter data
suggested that the compound melted congruently and was suitable for
crystal growth from the melt by the Czochralski technique,[2] a pre-
ferred method to produce large-diameter, low defect density crystals.
Crystal growth with this method is achieved by dipping an oriented seed
into a crucible containing the molten compound; the seed is then simul-
taneously rotated and withdrawn to form a crystal. Barium vanadate may
be grown at withdrawal rates of 1 to 6 mm/hr with 20 to 60 rpm rotation
rates.

Figure 1 illustrates the furnace configuration used for crystal
growth. It consists of the iridium crucible surrounded by crushed zir-
conia ceramic contained in a zirconia crucible resting on an alumina
pedestal. A protective argon atmosphere prevents oxidation of the
crucible. A zirconia cylinder and lid form the upper chamber, which is
used to generate the necessary temperature gradient for growth and slow
post-growth cooling.
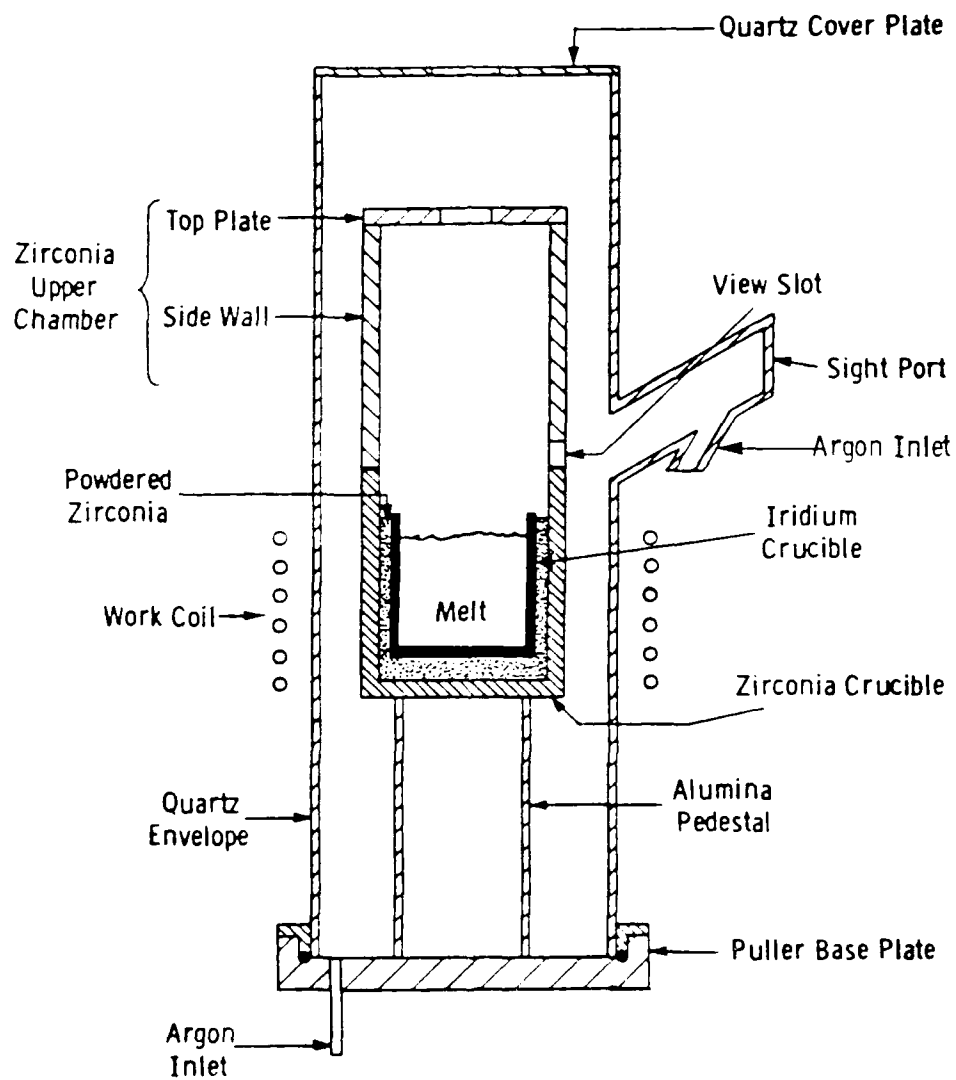
Figure 1 — Section view of crystal-growing furnace (schematic)

A quartz tube with built-in sight port envelopes the ceramic
assembly and contains the argon atmosphere. A water-cooled induction
coil surrounding the quartz tube provides power for melting the oxide by
coupling energy from a 10 kHz generator directly into the crucible.
Output from an Ircon automatic optical pyrometer focused at the crystal
periphery generates a signal for controlling the crystal diameter via
automatic adjustment of the generator output.

3. PHYSICAL PROPERTIES

A number of physical properties of $Ba_3(VO_4)_2$ was measured to characterize the crystals and to determine their suitability for epitaxial growth of hexaferrite films.

3.1 LATTICE PARAMETER

Matching of the crystal cell size between substrate and film is one of the most important parameters for epitaxy. Poor lattice matching may limit film growth completely or cause cracking of the film and substrate. The cell size of $Ba_3(VO_4)_2$ was measured using CuKα radiation on a Philips APD 3600 automated power diffractometer. The data from individual reflections were indexed automatically, and least squares refinement was completed using software provided with the diffractometer.

The cell size (a = 5.790 $\pm$ .001 Å and c = 21.340 $\pm$ 0.008 Å) for the pure compound was found to be a relatively poor match for barium hexaferrite, for which the reported cell dimensions are a = 5.893 Å and c = 23.194 Å. We found that a partial replacement of vanadium with tantalum in the compound increases its "a" dimension (see Table 1). The table indicates the variation in cell dimensions with the parameter "x" in $Ba_3(VO_4)_{2-x}(TaO_4)_x$.

Examination of the data indicates that the reported "a" parameter of barium hexaferrite and that of the substituted vanadate are essentially matched at a composition of $Ba_3(VO_4)_{1.2}(TaO_4)_{0.8}$.

3.2 THERMAL EXPANSION

To minimize thermally induced strains during cooling from the film growth temperature, the substrate and film should have similar

Table 1

Measured Cell Dimensions of
Ta-Substituted Barium Vanadate

$$Ba_3(VO_4)_{2-x}(TaO_4)_x$$
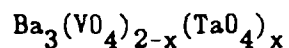
x	a	c
0	5.790	21.340
.2	5.810	21.320
.4	5.838	21.315
.6	5.865	21.306
.8	5.893	21.303
1.0	5.920	21.302*
1.2		*

*Presence of extra lines on the x-ray
pattern indicating phase transforma-
tion had taken place.

thermal expansion behavior. Figure 2 shows the thermal expansion
plotted from room temperature to 1000°C for a sample 1-1/2" x 1/4" x
1/4" cut parallel to the "c" direction. Figure 3 is the thermal
expansion from room temperature to 1000°C for a similar sample cut
perpendicular to the "c" axis. The data were collected with a quartz
tube dilatometer.

The average thermal expansion for barium vanadate parallel to
"c" is $10 \times 10^{-6} \cdot C^{-1}$, and perpendicular to "c" is $19 \times 10^{-6} \cdot C^{-1}$. The
exact values depend on the temperature and are comparable to those of
the hexaferrites.

3.3 DIELECTRIC CONSTANT AND MAGNETIZATION

Samples of $Ba_3(VO_4)_2$ 1.15 x 0.7 x 14.1 mm in size were attached
to alumina rods using Duco cement. Their dielectric constants and loss

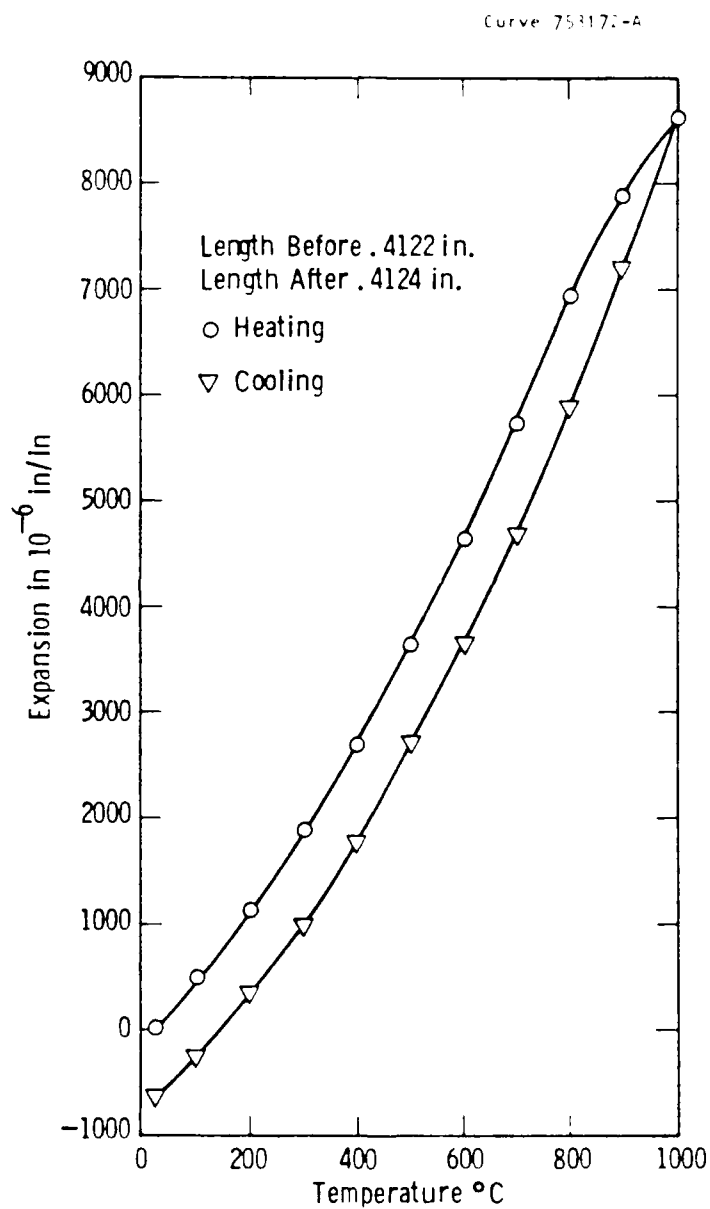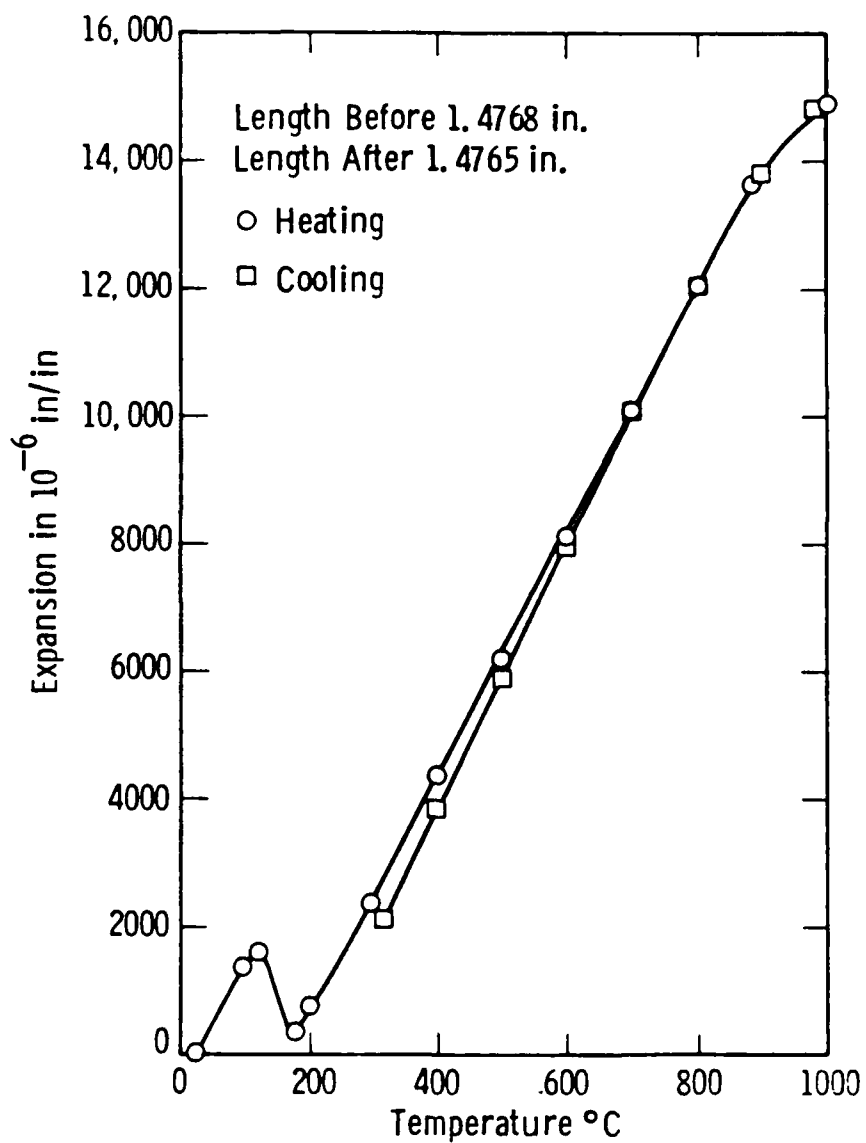Figure 2 — Thermal expansion of $Ba_3(VO_4)_2$ parallel to "c" direction cycled from RT to 1000°C to RT in air.

Figure 3 — Thermal expansion of $Ba_3(VO_4)_2$ perpendicular to "c" direction cycled from RT to 1000°C to RT in air.

tangents were measured using the ASTM Method, "Complex Dielectric Constant of Non-Metallic Materials (C525)," which is a microwave cavity perturbation technique. Magnetization samples 1 mm square were measured using the static Faraday balance technique and referenced to a standard nickel value of 6083 gauss. Table 2 shows the result of these measurements.

Table 2

Dielectric and Magnetic Properties
of Barium Vanadate

Dielectric Constant E_r	Loss Tangent $\tan \delta$	Magnetization $4 \pi M$ (G)
12.0	0.0016	+ 3.8

It should be noted that the magnetization is lower than that of gadolinium gallium garnet (+49 G), which is the standard substrate for yttrium iron garnet film growth. However, the dielectric constant is slightly higher than standard insulators such as alumina (about 9), and the loss tangent is also higher than that of low-loss alumina (.0001).

3.4 OPTICAL TRANSMITTANCE

A color variation was found for crystals of the same nominal melt composition--some were a smoky quartz gray, some were rose in color. To gain insight into this phenomena, optical transmission measurements were made on polished slices of crystal. Slices were cut and polished to 1 mm thickness, and measurements were made with a Perkin-Elmer 330 spectrometer.

The transmission spectrum between 0.3 to 1.5 μm is featureless with transmission uncorrected for reflection of about 80%. Figure 4 is a tracing of the spectra between 2.5 and 10 μm. Spectra of other crystals were similar, and the origin of the color variation was not clearly resolved.

3.5 HARDNESS

While hardness is not necessarily a major qualification for a good substrate material, knowledge of that property is important to optimize surface polishing before epitaxial growth. A Tukon microhardness tester was used on a 2 cm^2 polished sample of $Ba_3(VO_4)_2$. Several indentations were made over the surface of the sample, the measurement of which relates to the sample's hardness.

The average hardness measured in five tests was 307 Knoop, or between 4-5 on the Mohs scale. The material is harder than CaF_2 (163 Knoop), but softer than MgO (370 Knoop).
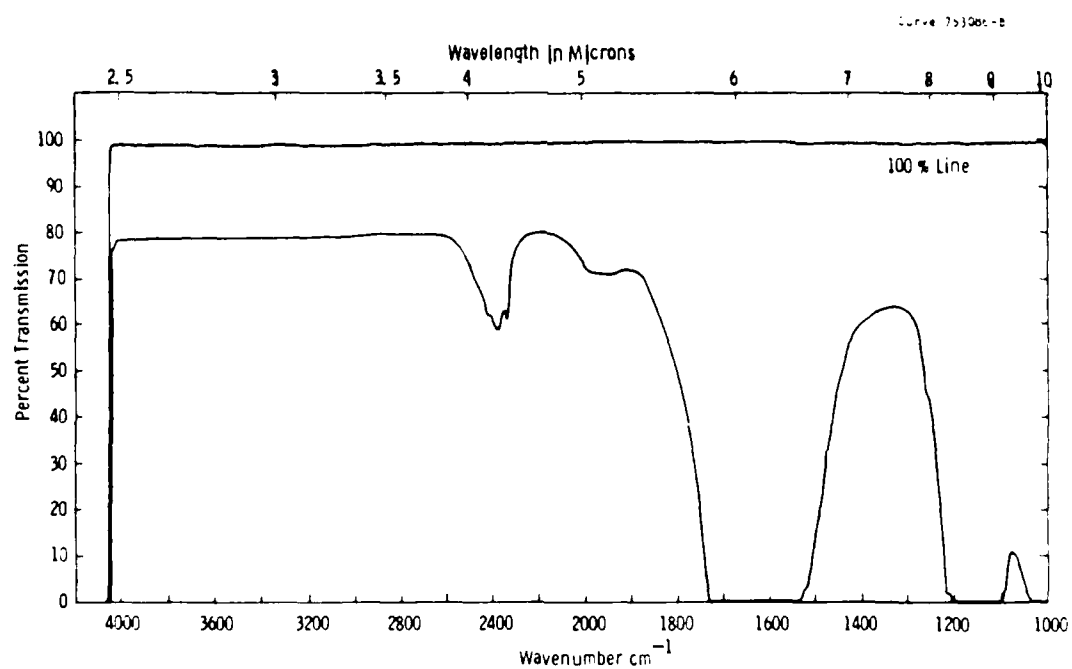
Figure 4 — Optical transmittance of $Ba_3(VO_4)_2$ crystal, 2.5-10 μm.

4. DISCUSSION

Unsubstituted barium vanadate is not an ideal substrate for epitaxy of barium ferrite. The lattice match of the stoichiometric composition is too small to match barium hexaferrite. However, substitution of up to 40% tantalum for vanadium in barium vanadate by solid solution raises the cell dimension linearly to match the "a" parameter of barium ferrite. The "c" parameter decreases slightly. (Since we grow films on the "c" face of the substrate, the "a" dimension substrate-film match is most critical for epitaxy.) Additions of larger amounts of tantalum cause x-ray line splitting, indicating a phase change or phase separation. Figure 5 is a plot of the oxide cell dimension variation as a function of tantalum concentration.

Besides the relatively good lattice matching to the ferrites, the Ta-substituted barium vanadate remains relatively homogeneous during growth. For example, only a slight deviation in lattice parameter is observed along the length of a 12.5 cm crystal: a = 5.891 and c = 21.306 at the crystal top; and a = 5.894 and c = 21.303 at the crystal bottom. These values suggest that the distribution coefficient of tantalum in $Ba_3(VO_4)_2$ is near unity. Figure 6 illustrates a crack-free barium vanadate crystal with 40% tantalum substitution.
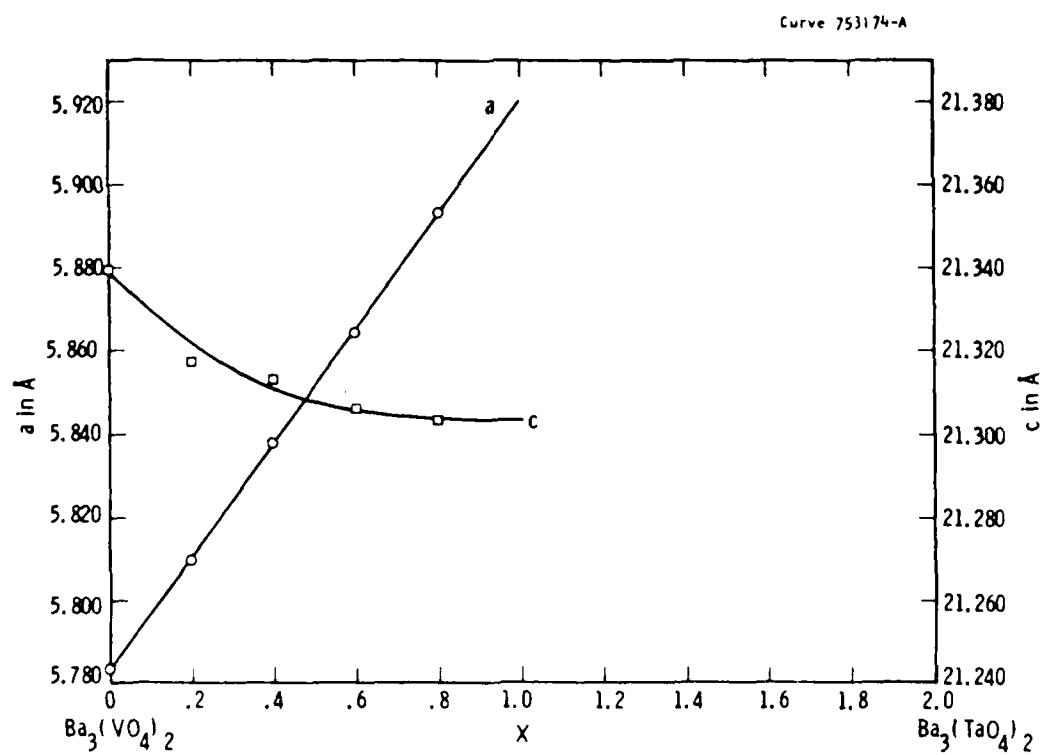
Figure 5 — Lattice parameters versus composition of $Ba_3(VO_4)_{2-x}(TaO_4)_x$.

$$Ba_3(VO_4)_{1.2}(TaO_4)_{.8}$$
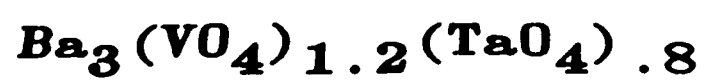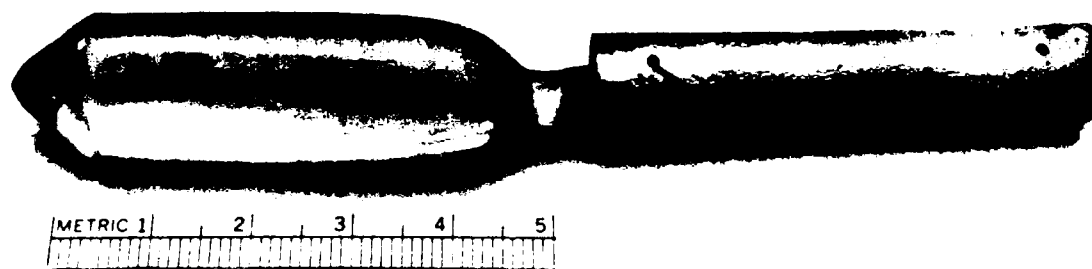
Figure 6 — Czochralski crystal.

5. CONCLUSIONS

$Ba_3(VO_4)_2$ is a promising substrate material for liquid phase epitaxy of ferrites for mm-wave devices. It can be doped with tantalum to adjust the cell dimension to match that of barium hexaferrite films.

Czochralski crystal growth of barium vanadate-tantalate is favored because the unsubstituted compound is congruent and the composition change of the Ta-substituted crystal is small along its length.

The dielectric constant is in the range for mm-wave devices, but the loss tangent of current crystals may need to be reduced for low-loss devices. Improved crystal quality may resolve that problem.

6. REFERENCES

1. D. Mateika and R. Laurien, <u>J. of Crystal Growth</u>, 52, 566 (1981).
2. K. Nassau and A. M. Broyer, <u>J. Amer. Cer. Soc.</u>, 45, 474 (1962).
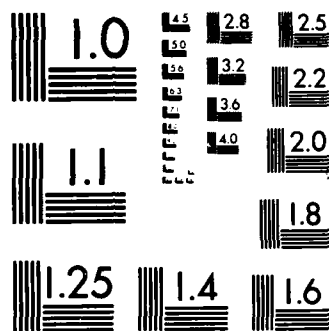
MICROCOPY RESOLUTION TEST CHART

NATIONAL BUREAU OF STANDARDS-1963-A

7. ACKNOWLEDGMENTS

Appendix III

INVESTIGATION OF HEXAGONAL FERRITE SUBSTRATE AND FILM GROWTH

W. E. Kramer, A. M. Stewart, R. H. Hopkins, Z. K. Kun, R. P. Storrick, and M. R. Daniel
Westinghouse R&D Center
Pittsburgh, PA 15235

Abstract – Hexagonal ferrites with large anisotropy fields can operate close to resonance at mm-wave frequencies. The growth of device-quality hexagonal ferrite films depends on the availability of lattice-matched substrates and optimized film deposition methods. Several potential substrate candidates were identified and characterized. Two promising materials, $Ba_3(VO_4)_2$ and $CoGa_2O_4$ were chosen for detailed study by LPE growth of hexaferrite films. Under the LPE growth conditions so far investigated, either no film nucleated on the $Ba_3(VO_4)_2$ or the substrates reacted with the melts. LPE layers were successfully grown on $CoGa_2O_4$ substrates. There was an interdiffused layer at the interface of the hexaferrite film and $CoGa_2O_4$ substrate. To obtain device-quality films on $SrGa_{12}O_{19}$ substrates (used for comparison), both film and substrate lattice parameters had to be adjusted by chemical substitution.

INTRODUCTION

Hexagonal ferrites with large anisotropy fields can operate close to resonance at mm-wave frequencies. Thus, devices based on films of these materials may match future needs for small, low-cost, mm-wave ferrite crystal components, tunable filters, and oscillators. This paper reports on the search for and growth of suitable substrates for both spinel and hexagonal ferrites and their behavior in LPE growth. A requirement for device-quality film growth is the availability of lattice-matched substrates which are chemically and thermally compatible. Selection criteria for substrate materials are as follows:

- lattice parameter and thermal expansion coefficient matching those of the ferrite film

- phase behavior: phase diagram containing sections where large, homogeneous, high-quality single crystals can be grown

- good mechanical strength (for slicing and polishing) and chemical and thermal compatibility with melt constituents: no dissolution, no diffusion

- good electrical insulator and paramagnetic or diamagnetic behavior

- low dielectric loss at microwave frequencies

For lattice matching the candidate substrate materials need not belong to the same material class as the film to be grown. For example, nonmagnetic spinels can serve as substrates both for magnetic spinels or for magnetic hexaferrites if the appropriate lattice matching between the cube face diagonal and hexagonal a dimension exists; i.e., if $a / \sqrt{2}$ spinel = a hexagonal. For barium hexaferrite, a = 5.89 Å so that a spinel substrate with a cube edge of 8.33 Å is suitable. Alternatively, a nonmagnetic material with the hexaferrite crystal structure and a = 5.89 Å is also suitable. The currently used substrate material reported in the literature is $SrGa_{12}O_{19}$,[1] lattice adjusted by Mg and Zr substitution.

SUBSTRATE CRYSTAL GROWTH

Lattice parameter was used as the first criterion for potential substrate material selection. Table 1

contains a list of compounds we synthesized in which the lattice dimensions are sufficiently close to those of the ferrite that modest alloying of either the film or the substrate could produce lattice registry.

TABLE 1

Some Cubic (Spinel) and Hexagonal Compounds Surveyed for Epitaxial Substrates

Cubic		Hexagonal
Co_2GeO_4	Mg_2VO_4	$KGa_{11}O_{17}$
Co_2SnO_4	Mg_2GeO_4	$Ba_3(VO_4)_2$
Co_2TiO_4	Mg_2SnO_4	
Co_2VO_4	Mg_2TiO_4	
Mn_2VO_4		

X-ray diffractograms indicated that the cubic compounds are all spinels with a values ranging from 8.326 Å to 8.60 Å. The lattice parameters for the hexagonal compounds were as follows:

	a	c
$KGa_{11}O_{17}$	5.80 Å	23.5 Å
$Ba_3(VO_4)_2$	5.79 Å	21.34 Å

The next selection criteria were compound melting point and phase behavior. The melting points ranged from 1600°C for Co_2GeO_4, Co_2SnO_4, and $Ba_3(VO_4)_2$, to 1800°C for Mg_2GeO_4, 1900°C for $KGa_{11}O_{17}$, and over 2000°C for Mg_2SnO_4. These melting points place most of the potential substrate candidates within the practical range of the Czochralski crystal growth process.

Czochralski pulling from the melt is the preferred crystal growth technique when large, homogeneous, high-quality crystals are needed. For survey purposes, however, we also used float zone and flux growth techniques. Table 2 lists the melting behavior, crystal quality, and lattice size of the most attractive candidate substrates. For comparison, Mg,Zr-substituted $SnGa_{12}O_{19}$ crystals were also grown.[1] Instead of Czochralski pulling, $ZnGa_2O_4$ was grown from the flux to minimize its decomposition by reducing the partial pressure of ZnO over the melt.

TABLE 2

C–U–B–I–C

Crystals	Melting Behavior	Crystal Quality	Lattice Size	Growth Method
$ZnGa_2O_4$	Incongruent	Low defect	8.33 Å	Flux
$CoGa_2O_4$	Congruent	Low defect	8.32 Å	CZ

H–E–X–A–G–O–N–A–L

Crystals	Melting Behavior	Crystal Quality	Lattice Size	Growth Method
$SrGa_{12}O_{19}$	Incongruent	Core Structure	a 5.82 c 23.06	CZ
$Ba_3(VO_4)_2$	Congruent	Low defect	a 5.78 c 21.34	CZ

$$\frac{a_{spinel}}{\sqrt{2}} \approx \frac{8.33 \text{ Å}}{\sqrt{2}} \approx a_{Hexaferrite}$$

A publication on the crystal growth of $Ba_3(VO_4)_2$ crystals (Figure 1) is planned and a paper on the growth of $CoGa_2O_4$ crystals has been published elsewhere.[2]
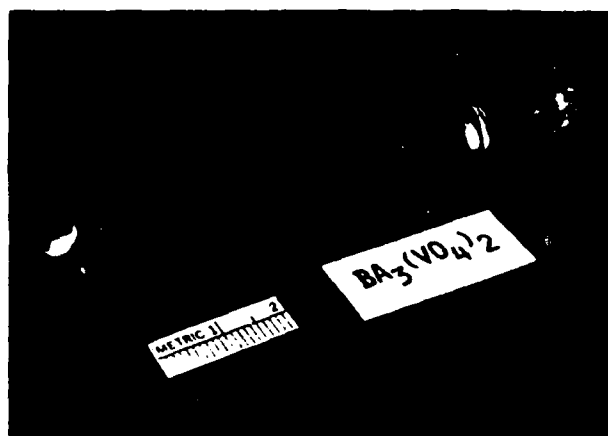
Figure 1. Czochralski pulled $Ba_3(VO_4)_2$ boule.

Figure 3. LPE layer on $CoGa_2O_4$. (BF05)

LPE layers were analyzed chemically by electron micro-probe to verify their composition as compared to bulk hexaferrite, and to detect residual impurities originating from the flux and platinum ware. Laue photography was used to verify that epitaxial growth had occurred.

LPE Growth of Films and Substrate Characterization.

Substrates were prepared by orienting the single crystals, cutting wafers from them, and then lapping and polishing them (Figure 2). The substrate materials were evaluated using various epitaxial growth conditions. Four different fluxes were chosen based on literature data. They were PbO-PbF_2, BaO-B_2O_3,[3] BaO-BaF_2-B_2O_3,[4] and Bi_2O_3-B_2O_3.[5]

Microscopic examination of the LPE layer–$CoGa_2O_4$ interface showed that there there the flux reacted with the substrate (Figure 4). Electron microprobe scans showed an interdiffused layer of flux and substrate consti-tuents at the interface (Figure 5) in which the thickness was time and temperature dependent. The interdiffused layer was ~ 10 µm thick in sample BF05 (Table 4) and 5 µm thick in sample BF017. As a result of the interdiffusion, the hexaferrite layers tended to peel off the $CoGa_2O_4$ substrate, apparently by crack formation.

Co Ga₂ O₄   Sr Ga₁₂ O₁₉

Figure 2. Two substrates prepared for LPE growth.

Quantitative electron microprobe analysis of cation concentration, normalized to iron, gave a film composition of $Ba_{0.88}Bi_{0.085}Fe_{12}$ with only traces of platinum in sample BF011, which was grown on $SrGa_{12}O_{19}$ substrate. Since bismuth increases the lattice parameter of the LPE layer, we expected to find cracks in BF011 due to increased film-substrate mismatch. Measurements confirmed that the lattice parameters of the LPE layer were a = 5.8933 Å, c = 23.1909 Å, and those of the hexagallate substrate were a = 5.8245 Å and c = 23.081 Å.

To reduce the influence of bismuth, Aℓ was substi-tuted in the LPE layer (BF019 and 21). At the rela-tively low growth temperature of 959°C, the substituted aluminum concentration was higher than required. Preliminary measurements of H_A - 4πM of Aℓ-substituted films indicated this. It is expected that an LPE layer grown at higher temperatures will contain more nearly the required Aℓ concentration.[6]

The substrate materials were measured for magneti-zation and dielectric losses. Table 5 lists the measurements made at room temperature on the candidate substrate materials. The dielectric and loss tangent data were measured with samples in a microwave cavity resonant at 9 GHz. They were performed at a microwave electric field maximum in the cavity and hence do not include any magnetic contributions to tan δ. The numerical values are averages of measurements on two or three samples.

Most of the LPE growths were attempted in the vertical dip configuration, either under isothermal conditions or by cooling over a temperature interval. Aℓ-doped (lattice parameter adjusted) film samples were grown on horizontally dipped substrates, rotating at 50 rpm. Table 3 gives a summary of substrate behavior during the LPE growth of barium hexaferrite films. Under the growth conditions tried, there was either no nucleation on the $Ba_3(VO_4)_2$ substrates or the substrate dissolved. LPE growth was accomplished on $CoGa_2O_4$ and on $Sr(Ga, Mg, Zr)_{12}O_{19}$ substrates. Table 4 summarizes the LPE growth conditions.

A typical appearance of the LPE layer on a $CoGa_2O_4$ substrate is shown in Figure 3 (BF05). The surface morphology of the LPE layers was examined by optical microscope. Layers on both kinds of substrates contained smooth and terraced areas suggesting small orientation variations across the substrate faces. The
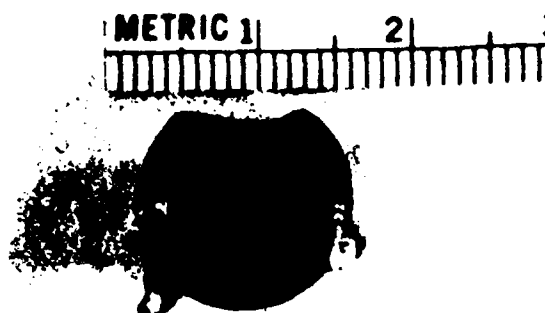
The magnetization data were taken on small (approx. 1 mm square) samples using the static Faraday balance technique and references to a standard nickel value of 6083 gauss. Again, the quoted numbers in Table 5 are averages of results on two or three samples. It is interesting to note that all of the magnetization values are below the value for gadolinium

Table 3

Substrate Behavior During the LPE Growth of Barium Hexaferrite Films

Flux Constituents	Mole% Solute	Temperature (Range) of LPE Growth	Substrate Behavior in LPE Growth		
			$CoGa_2O_4$	$SrGa_{12}O_{19}$	$Ba_3(VO_4)_2$
PbO PbF$_2$	13.5	928°C			No film
BaCO$_3$(Ba$_2$O)	23.2	1007°C			
		971°C			No film
BaF$_2$ B$_2$O$_3$	24.8	1025°C	Film Grown,		
		1000°C	Matt Surface		No film
	29.5	922-932°C	Film Grown (BFO17)		
Bi$_2$O$_3$ B$_2$O$_3$	32.2	967-989°C	Film Grown (BFO 5) (BFO 9) (BFO 21)	Film Grown (BFO 11) (BFO 19)	Substrate Dissolved

Table 4

LPE Growth Conditions and Characteristics of Barium Hexaferrite Films

The flux used was Bi_2O_3-B_2O_3

Substrate	Sample Design- ation	Super- cooling (°C)	Growth Temp. (°C)	Film Thickness (μm)	Growth Rate (μm/min.)	Surface Morphology
CoGa$_2$O$_4$	BFO5	9	981	7.5	0.23	
	BFO9	24	966	N.R.	-	
	BFO17	8	932	3.5	0.35	Some smooth and some terraced areas
	BFO21 Same as BFO19	23	959	10	0.5	Structured surface
SrGa$_{12}$O$_{19}$	BFO10	22	968	18	1.2	Mainly smooth with a few terraces
	BFO11	21	969	2.8	0.56	Relatively smooth all over
	BFO19 Horizontal dip. at 50 rpm. Film lattice parameter is adjusted by Al doping.	23	959	<1 2-3 10	0.1-0.15 0.5	Corresponds to substrate consis- ting of three different oriented sections.

gallium garnet (+49G), which is the substrate material employed for the epitaxial yttrium iron garnet. Additionally, the loss tangent data are about 20 times larger than that for the microwave ultra low-loss material alumina (tan δ = 0.0001).

CONCLUSIONS

Among the potential substrate materials surveyed for ferrite epitaxy, large single crystals of $Ba_3(VO_4)_2$ and $CoGa_2O_4$ were grown. For comparison, Mg,Zr-substituted $SrGa_{12}O_{19}$ was also grown. All substrates were employed in the LPE growth of barium hexaferrite films. Of the fluxes so far studied, $Ba_3(VO_4)_2$ has either dissolved or no film nucleation occurred. LPE layers were successfully grown on $CoGa_2O_4$ substrates. However, there was an interdiffused layer in which the thickness depended on the time and temperature of the LPE growth. For good-quality layer growth on (Mg,Zr) $SrGa_{12}O_{19}$ substrates, Al was substituted to compensate the size effect of Bi incorporating from the flux. Magnetization and loss measurements showed that the studied substrate materials are suitable for use at mm-wave frequencies.
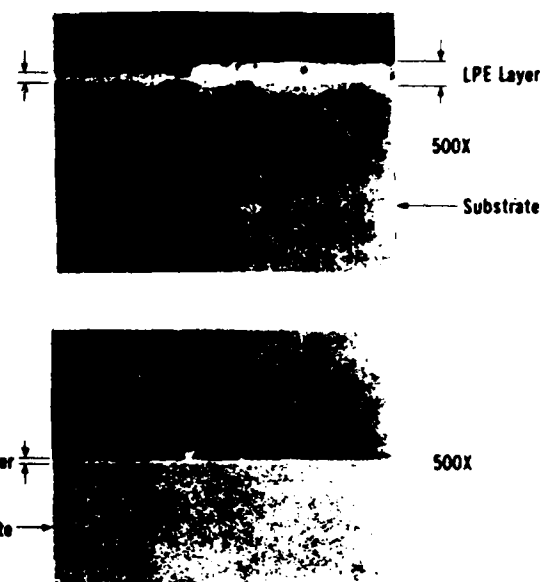

Figure 4. Layer-substrate interface for $CoGa_2O_4$ (top) substrate. For comparison, a sharply delineated LPE layer-$SrGa_{12}O_{19}$ interface is also shown (bottom).

TABLE 5

Material	Dielectric Constant Er	Loss Tangent tan δ	Magnetization 4 πM (G)
Strontium gallate	9.6	0.0019	− 0.10
Cobalt gallate	9.2	0.0023	+18.0
Barium vanadate	12.0	0.0016	+ 3.8

REFERENCES

[1] P. Mateika and R. Laurien, J. Crystal Growth 52, 566 (1981).

[2] W. E. Kramer, A. M. Stewart and R. H. Hopkins, J. Cryst. Growth 73, 329 (1985).

[3] R. C. Linares, J. Am. Ceramic Soc. 45, 307 (1962).

[4] R. Hiskes, T. L. Felmke and B. A. Burmeister, Paper presented at Tech. Conf. on Recent Advances in Electronic, Optical & Magnetic Materials, Sept. 1971, San Francisco.

[5] H. Dötsch et al., Mat. Res. Bull. 18, 1209 (1983).

[6] J. M. Coutellier et al., Digest of papers presented at the International Conf. on Magnetism, San Francisco, 1985, p. 56.

ACKNOWLEDGEMENTS

Appendix IV

Investigation of Growth Conditions for the Liquid Phase Epitaxy of Hexaferrite Films Using a Bi_2O_3-BaO-B_2O_3 Flux

K. C. Yoo, R. P. Storrick, W. E. Kramer,
A. M. Stewart, and R. H. Hopkins
Crystal Science Technology

ABSTRACT

Conditions favoring the liquid phase epitaxy (LPE) growth of barium hexaferrite films have been investigated using the Bi_2O_3-BaO-B_2O_3 flux system. The barium hexaferrite-saturated solutions based on this flux system exhibit relatively large degrees of supercooling (up to 65°C). However, the $BaFe_{12}O_{19}$ phase field occupies a limited region of the Bi_2O_3-BaO-B_2O_3 pseudo ternary phase diagram. LPE films of pure barium hexaferrite and aluminum-substituted hexaferrite were successfully grown on $Sr(Ga,Mg,Zr)_{12}O_{19}$ substrates using this flux system. Microstructural evaluation of the films by x-ray topography and optical microscopy indicates that smooth, uncracked barium hexaferrite films can be grown on strontium hexagallate substrates from selected compositions in the ternary system under conditions which minimize lattice mismatch between film and substrate.

1. INTRODUCTION

Hexagonal ferrites exhibit a large anisotropy field and magnetization and thus can operate close to resonance at mm-wave frequencies with a small field. For this reason, hexaferrite films have been attractive candidates for mm-wave device applications.

The first attempt to grow hexaferrite films by LPE was reported by Sterns and Glass in 1975 [1]. Since then numerous efforts have been made to grow hexaferrite films using a variety of substrates including $MgAl_2O_4$, $MgGa_2O_4$, $Mg(In,Ga)_2O_4$ [2,3], $SrGa_{12}O_{19}$ [4,5], $Sr(Ga,Mg,Zr)_{12}O_{19}$ [6,7], $Sr(Ga,Mn,Zr)_{12}O_{19}$ [7], $CoGa_2O_4$ [8], and $Ba_3(VO_4)_{1.2}(TaO_4)_{.8}$ [9]. The results of these studies suggest that difficulties in growing good-quality films can be attributed both to the lack of suitable, lattice-matched substrate materials, and to unoptimized solvent systems (fluxes) for hexaferrite depositions.

Recently we evaluated potential substrate materials for the LPE growth of hexaferrites under various epitaxial growth conditions [8,9]. Among those candidate substrate materials, large, low defect density single crystals of $CoGa_2O_4$, $Ba_3(VO_4)_2$, and the solid solution $Ba_3(VO_4)_{1.2}(TaO_4)_{.8}$ having relatively small lattice-mismatch with $BaFe_{12}O_{19}$ were successfully grown. LPE experiments on these substrates indicated that they are chemically and thermally unstable in conventional flux melts such as $Bi_2O_3-B_2O_3$ and $PbO-B_2O_3$; they dissolve during the LPE film growth process or form interdiffusion layers. On the other hand, the use of Mg,Zr-substituted $SrGa_{12}O_{19}$ crystals which are chemically and thermally stable often result in highly facetted films of poor morphological quality [6].

Because of these difficulties, development of new flux systems which avoid structural deterioration in some potential substrate materials, operate at temperatures where thermal instability is minimized, and can produce good-quality LPE films was undertaken. Thus, in the present investigation, emphasis has been placed on a systematic study of the new Bi_2O_3-BaO-B_2O_3 flux system for the growth of hexagonal ferrite films. The structural quality of the films produced using this new flux system was examined by x-ray topography and optical microscopy.

2. Bi_2O_3-BaO-B_2O_3 FLUX

The general requirements for choosing a flux system for LPE film growth are that the solution must exhibit: (1) a large degree of super-cooling to drive film deposition without spontaneous crystallization, (2) a low melting point, and (3) a low viscosity at the growth tempera-ture. During our preliminary studies of several other solvents, includ-ing BaO-B_2O_3, BaO-V_2O_5, Na_2O-B_2O_3, and BaO-BaF_2-B_2O_3, Bi_2O_3-BaO-B_2O_3 proved to be the most successful solvent for the LPE growth of barium hexaferrite film.

Development of the ternary flux was initiated with studies of melting relations along the binary join, Bi_2O_3-BaO. To minimize the growth temperature during LPE, emphasis was placed on identifying the lowest liquidus temperature of the solvent. The liquidus temperatures at the different BaO compositions for the Bi_2O_3-BaO system were measured as shown in Figure 1. Based on these measurements, the composition with the lowest liquidus temperature (764°C at 15 mole% BaO) was selected to make the initial barium hexaferrite saturated solutions.

The solutions were prepared from the 15 mole% BaO-Bi_2O_3 solvent by adding hexaferrite (BaO + 6Fe_2O_3) to form a series of compositions in which the mole ratio of ferrite to the solvent was varied. The liquidus temperature of the ferrite-flux solution was measured for each ferrite composition. The measurements indicate that the liquidus temperature increases nearly linearly with the ferrite composition as shown in Figure 2.

Qualitative measurements of the degree of supercooling of the ferrite solutions were performed by observing the appearance and disap-pearance of spontaneously nucleated crystallites in each melt during repeated slow-cooling and heating cycles. Crystallites were collected from each melt using a platinum basket in order to determine composition
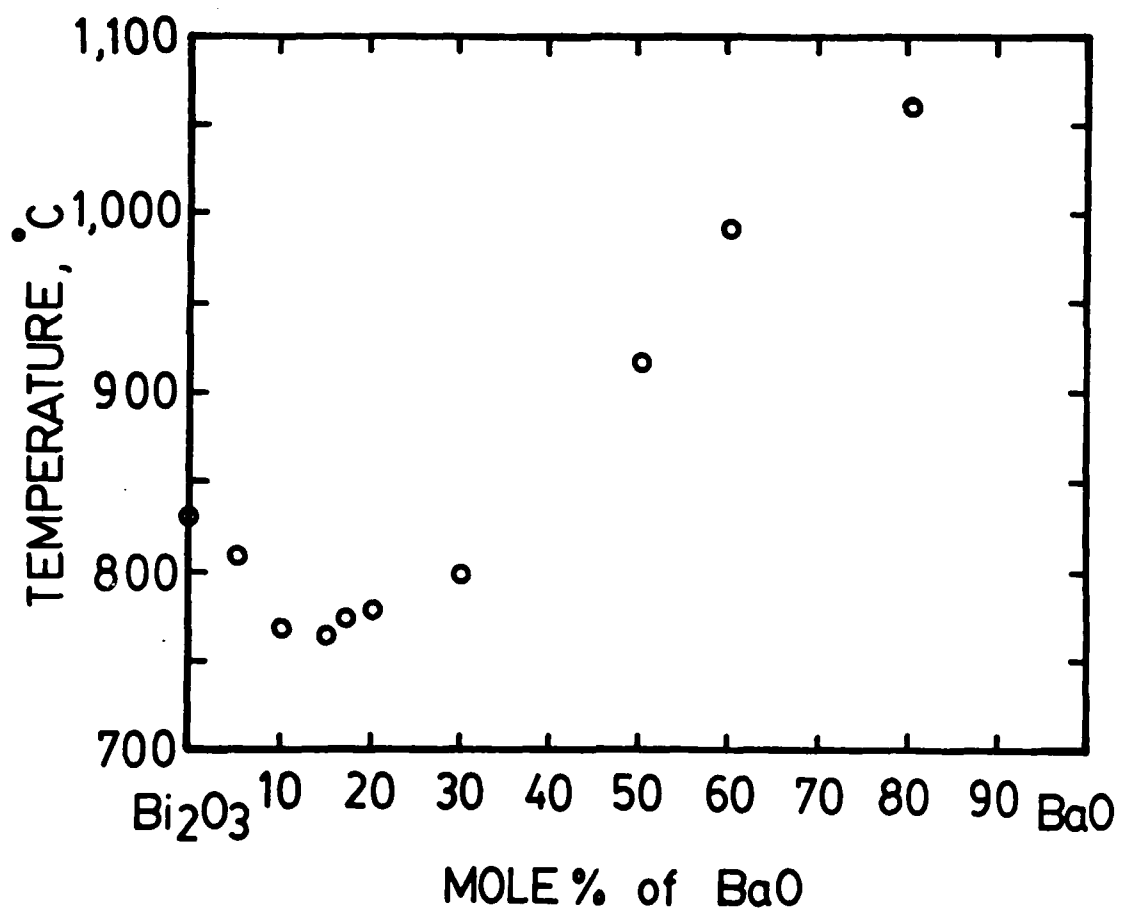
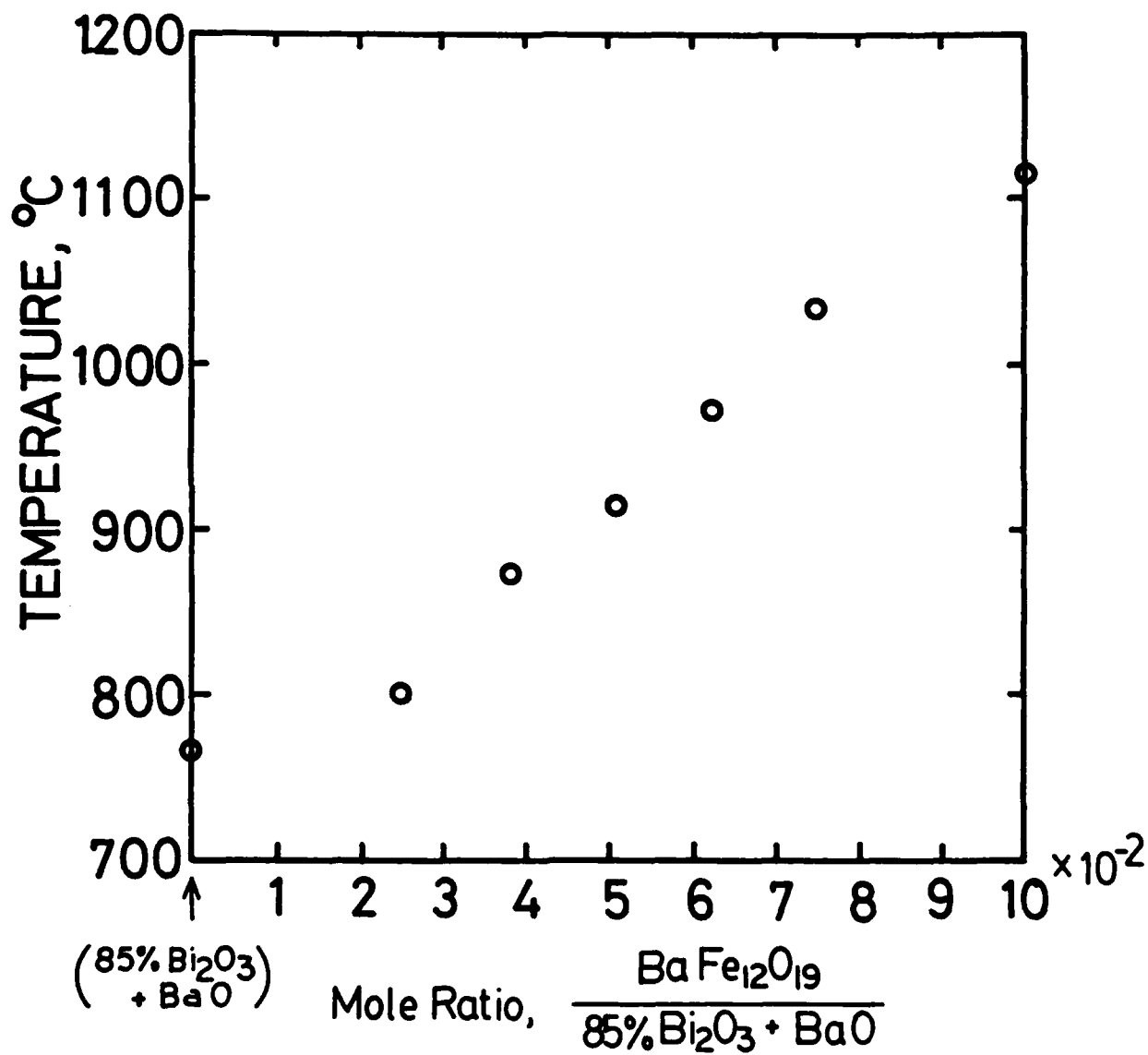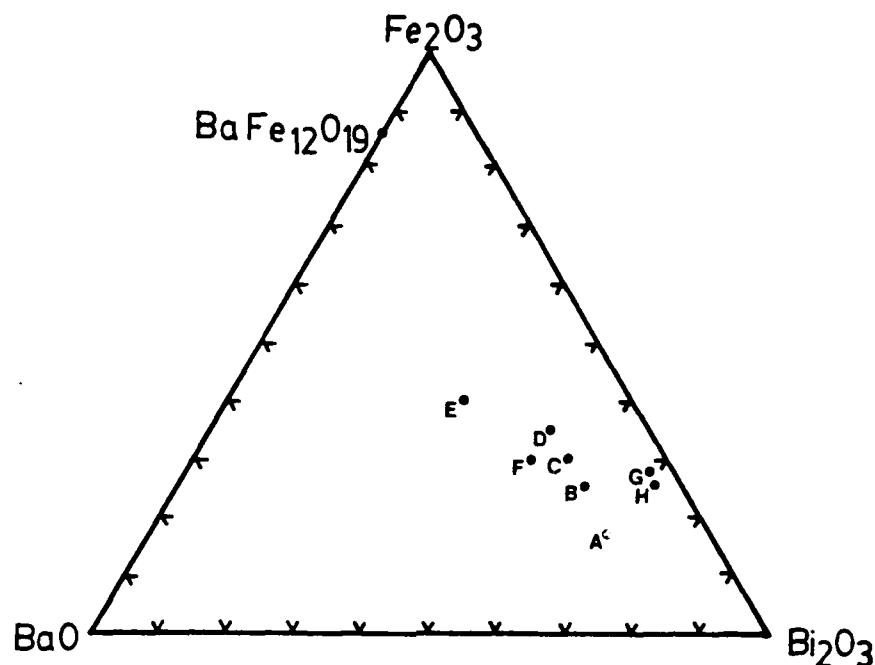Figure 1 — Liquidus temperatures as a function of BaO composition in the Bi_2O_3-BaO system.

Figure 2 — Liquidus temperatures as a function of $BaFe_{12}O_{19}$ in the 85% Bi_2O_3-BaO solution.

of the precipitating phase(s) by x-ray diffraction measurements. Figure 3 shows the crystallite phases identified, the liquidus temperature, and the degree of supercooling for each solution composition.

The data indicate that the barium hexaferrite field in the pseudo-ternary phase diagram is quite limited to liquidus temperatures near 1000°C. Because high degrees of supercooling are observed in these solutions, it has been possible to choose actual growth temperatures below 1000°C without any spontaneous nucleation. The addition of B_2O_3 (5 mole%) to the Bi_2O_3-BaO system also appears to enhance the capability for supercooling by about 5°C.

Fe$_2$O$_3$

BaFe$_{12}$O$_{19}$

E•

D•
F• C•
B•   G•
H•
A<

BaO

Bi$_2$O$_3$

	COMPOSITION (MOLE %)			L.T. (°C)	ΔT (°C)	CRYSTALLITE
	Bi$_2$O$_3$	BaO	Fe$_2$O$_3$			
A	67.3	14.9	17.8	874	36	BaFeO$_{2.8}$
B	60	15	25	973	58	BaFeO2.8
C	55	15	30	1035	65	BaFe$_{12}$O$_{19}$, BaFeO$_{2.8}$
D	50	15	35	1113	58	BaFe$_{12}$O$_{19}$
E	35	25	40	1136	27	BaFe$_{12}$O$_{19}$, Fe$_3$O$_4$
F	50	20	30	1010	38	BaFe$_{12}$O$_{19}$
G	68.5	4.5	27	960	45	BaFe$_{12}$O$_{19}$, BiFeO$_3$
H	69.7	4.3	26	938	50	BaFe$_{12}$O$_{19}$, BiFeO$_3$

L.T. : Liquidus Temperature

ΔT : Degree of Supercooling

Figure 3 — Fe$_2$O$_3$-BaO-Bi$_2$O$_3$ pseudo-ternary phase diagram. Liquidus temperatures, degree of supercooling, and phase analysis of crystallites at different compositions are shown.

97

3. GROWTH AND CHARACTERIZATION OF FILMS

The solutions having compositions C, D, F, and H of Figure 2 with the addition of 5 mole% B_2O_3 were chosen to perform the LPE film growth of barium hexaferrite. A $Sr(Ga,Mg,Zr)_{12}O_{19}$ substrate was mounted horizontally and slowly lowered into a furnace after thermal equilibrium had been established in the solution. The solution was contained in a platinum crucible in a controlled constant temperature zone with the furnace set at a growth temperature.

The substrate was held for 2 min just above the surface of the solution, then immersed horizontally with axial rotation (50 rpm). The deposition time was varied from 3 min to 15 min. The thickness of the films was measured by microscopic examination of the cleaved interface between the film and the substrate.

In the present investigation, three different film compositions, $BaFe_{12}O_{19}$, $BaFe_{10.7}Al_{1.3}O_{19}$, and $BaFe_{9.3}Al_{2.7}O_{19}$, were chosen for growth. Although spontaneous precipitation of two different types of crystallites was observed in solutions C and H when no substrate was present, only barium hexaferrite films grew on the strontium hexagallate substrates.

In LPE, minimizing the lattice mismatch between substrate and film is crucial to grow good-quality film growth. The control of this particular parameter has been approached in two different ways--by adjusting the lattice parameter of the substrate as well as that of the film. Considering the strontium hexagallate a promising substrate material, Mateika and Laurien [10] studied Czochralski growth of strontium gallate solid solutions in which partial substitution of the cations in the host composition was employed to match the substrate and film parameters.

98

Based on this study, $Sr(Ga,Mg,Zr)_{12}O_{19}$ crystals were grown by Czochralski crystal pulling using weight control of the crystal diameter. The lattice parameters of typical samples grown by us and analyzed by x-ray diffraction measurements were close to a = 5.823 Å and c = 23.073 Å. Since the lattice parameters of stoichiometric $BaFe_{12}O_{19}$ are a = 5.892 Å and c = 23.198 Å, the expected lattice mismatches are Δa/a = 1.17% and Δc/c = 0.54%. Further decrease in the lattice mismatch by substrate composition adjustment proved difficult due to phase separation in the crystals.

Replacement of Fe by Al in barium hexaferrite, however, can bring the substrate and film lattices into better registry. Aluminum-substituted film compositions were adopted from the work done by Coutellier et al. [7]. Lattice parameters of $BaFe_{10.7}Al_{1.3}O_{19}$ and $BaFe_{9.3}Al_{2.7}O_{19}$ films grown here and measured by x-ray diffraction were, respectively: a = 5.845 Å, c = 22.988 Å, and a = 5.801 Å, c = 22.884 Å. The lattice mismatches of $BaFe_{10.7}Al_{1.3}O_{19}$ and $BaFe_{9.3}Al_{2.7}O_{19}$ films with $Sr(Ga,Mg,Zr)_{12}O_{19}$ substrates are, respectively: Δa/a = 0.37%, Δc/c = 0.36%, and Δa/a = 0.38%, Δc/c = 0.83%. Thus, the composition $BaFe_{10.7}Al_{1.3}O_{19}$ has the best lattice match with $Sr(Ga,Mg,Zr)_{12}O_{19}$ in both the "a" and "c" directions.

The film structures of five typical samples were examined by optical microscopy and surface reflection x-ray topography. The growth conditions of these samples are shown in Table 1. Figures 4a and 4b are, respectively, optical micrographs taken from a barium hexaferrite film of stoichiometric composition and a $BaFe_{10.7}Al_{1.3}O_{19}$ film grown on $Sr(Ga,Mg,Zr)_{12}O_{19}$ substrates. These films were grown from the same solution at the composition H of Figure 2 (with the addition of 5 mole% ratio of B_2O_3 to the Bi_2O_3-BaO solvent).

The unsubstituted barium hexaferrite film shows hexagonal islands in the presence of large numbers of cracks. In contrast, the aluminum-doped $BaFe_{10.7}Al_{1.3}O_{19}$ film appears dense and adherent without cracks. Figures 5a, 5b, and 5c are optical micrographs taken from $BaFe_{9.3}Al_{2.7}O_{19}$ films having different film thicknesses: 40 μm, 10 μm, and 5 μm, respectively. As shown in these figures, the 40 μm thick film

(a) $BaFe_{12}O_{19}$ Film

200 μm

(b) $BaFe_{10.7}Al_{1.3}O_{19}$ Film

Figure 4 — Optical micrographs of (a) $BaFe_{12}O_{19}$ film and
(b) $BaFe_{10.7}Al_{1.3}O_{19}$ film. Growth conditions of these
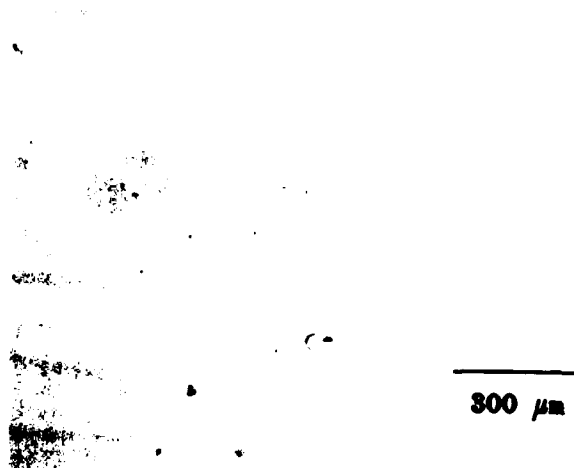films are shown in Table 1.

100

(a)

(b)

(c)

300 μm

Figure 5 — Optical micrographs of $BaFe_{9.7}Al_{2.3}O_{19}$ films having
different thicknesses: (a) 40 μm, (b) 10 μm, and (c) 5 μm.

101

Table 1

Growth Conditions of Five Typical Samples

Film Composition	Flux Composition	Growth Temperature	Growth Time	Thickness
$BaFe_{12}O_{19}$	H	911°C	15 min	40 μm
$BaFe_{10.7}Al_{1.3}O_{19}$	H	914°C	15 min	40 μm
$BaFe_{9.3}Al_{2.7}O_{19}$	C	1001°C	15 min	40 μm
$BaFe_{9.3}Al_{2.7}O_{19}$	C	1008°C	5 min	10 μm
$BaFe_{9.3}Al_{2.7}O_{19}$	C	1008°C	3 min	5 μm

exhibits a "roof shingle" type structure with large numbers of cracks. The 10 μm thick film also shows a number of cracks; however, the surface appears topographically very smooth. The structure of 5 μm thick film appears very smooth and without cracks.

These results indicate that the best films are obtained from the composition $BaFe_{10.7}Al_{1.3}O_{19}$, that with the lowest lattice mismatch among the three film compositions examined. For example, the $BaFe_{10.7}Al_{1.3}O_{19}$ and $BaFe_{9.3}Al_{2.7}O_{19}$ films have a very similar lattice mismatch in the "a" direction, i.e., $\Delta a/a = 0.37\%$ and 0.38%. However, they have larger mismatch in the "c" direction: $\Delta c/c = 0.36\%$ for $BaFe_{10.7}Al_{1.3}O_{19}$ and 0.83% for $BaFe_{9.3}Al_{2.7}O_{19}$. As indicated by Rinaldi et al. [11], since "c" is larger than 20 Å in hexaferrites corresponding to at least ten atomic layers, this mismatch is not easily compensated by strains or local defects such as dislocations. This suggests that the larger mismatch along "c" in the $BaFe_{9.3}Al_{2.7}O_{19}$ films contributes to forming cracks (Figure 4) in contrast to the $BaFe_{10.7}Al_{1.3}O_{19}$ film.

The terrace structure of the $BaFe_{9.3}Al_{2.7}O_{19}$ film shown in Figure 5a is probably caused by the combined effects of the slight misalignment of the substrate surface with respect to the "c" plane and the relatively large lattice mismatch. However, the important observation here is that the microstructure of the films also depends on the film thickness. This is illustrated in the series of optical micrographs of Figure 5. Very smooth films of $BaFe_{9.3}Al_{2.7}O_{19}$ are grown up to 5 μm thick even with their particular lattice mismatch.

X-ray topographic techniques can offer very useful information on microdefect distributions in epilayers. Figure 6a and 6b are Berg-Barrett surface reflection x-ray topographs taken from a barium hexaferrite film of stoichiometric composition and a $BaFe_{10.7}Al_{1.3}O_{19}$ film grown on $Sr(Ga,Mg,Zr)_{12}O_{19}$. These are the same films shown in the optical micrographs of Figures 4a and 4b. In contrast to the optical micrographs of Figure 4, the x-ray topographs show the overall microstructure of the films at a low magnification.

The x-ray topograph of the unsubstituted barium hexaferrite film exhibits a large number of white lines in the film. However, the structure of Al-substituted film appears free of line defect images. The detailed structures of the films are compared at a higher magnification in Figures 7a and 7b. These line defect images, which represent areas out of diffraction contrast in the x-ray topograph, are due to the cracks in the film. Also, both x-ray topographs show relatively large areas without diffraction contrast. These are probably regions where the films did not grow epitaxially, or where the substrate is misoriented with respect to the film matrix.

(a)
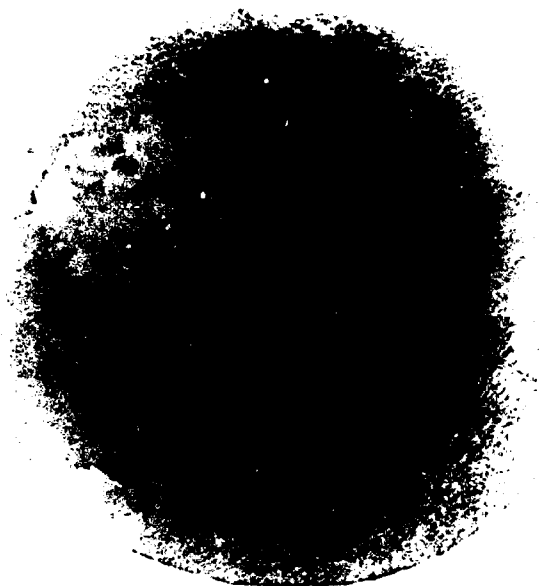
(b)
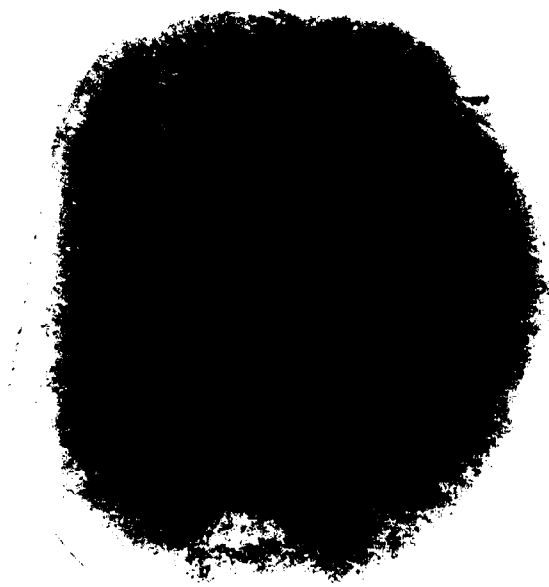
5 mm

Figure 6 — (a) Berg-Barrett x-ray topograph of a $BaFe_{12}O_{19}$ film.
(b) Berg-Barrett x-ray topograph of a $BaFe_{10.7}Al_{1.3}O_{19}$ film.

104

(a)

(b)

2 mm

Figure 7 — The same x-ray topographs that are shown in Figure 6 at a higher magnification.

105

RM-12815

4. CONCLUSIONS

It has been demonstrated that barium hexaferrite films of good quality can be grown from compositions in the Bi_2O_3-BaO-B_2O_3 flux system under conditions producing good lattice match between substrate and film. The Bi_2O_3-BaO-B_2O_3 flux system has the advantage that it facilitates relatively large degrees of supercooling combined with a relatively low growth temperature. In these experiments, the lattice mismatch between substrate and film has been reduced by the substitution of Ga by Mg and Zr in strontium hexagallate and the substitution of Fe by Al in barium hexaferrite. X-ray topographic and optical microscopic observation of the film structures indicated that a relatively large lattice mismatch tends to favor large numbers of hexagonal islands and cracks in the films. Al-substituted barium hexaferrite films produced the best quality films. These exhibit topographically very smooth surface without cracks by reducing the film-substrate lattice mismatch to $\Delta a/a = 0.37\%$ and $\Delta c/c = 0.36\%$.

5. REFERENCES

1. Stearns, F. S., and H. L. Glass, <u>Mat. Res. Bull.</u> <u>10</u>, 1255 (1975).

2. Stearns, F. S., and H. L. Glass, <u>Mat. Res. Bull.</u> <u>11</u>, 1319 (1976).

3. Glass, H. L., and F. S. Stearns, <u>IEEE Trans. Magnetics</u>, <u>MAG-13(5)</u>, 1241 (1977).

4. Haberey, F., R. Leckebusch, M. Rosenberg, and K. Sahl, <u>Mat. Res. Bull.</u> <u>15</u>, 493 (1980).

5. Haberey, F., R. Leckebusch, M. Rosenberg, and K. Sahl, <u>J. Crystal Growth</u> <u>52</u>, 734 (1981).

6. Dosch, H., D. Mateika, P. Roschmann, and W. Tolksololf, <u>Mat. Res. Bull.</u> <u>18</u>, 1209 (1983).

7. Coutellier, J. M., J. Vaval, B. Ferrand, J. C. Gay, Y. Grange, and M. Chamel, <u>IEEE Trans. on Magnetics</u>, <u>MAG-21(5)</u>, 56 (1985).

8. Kramer, W. E., A. M. Stewart, R. H. Hopkins, Z. K. Kun, R. P. Storrick, and M. R. Daniel, <u>IEEE Trans. on Magnetics</u> <u>MAG-22(5)</u>, 981 (1986).

9. Kramer et al., to be published.

10. Mateika, D., and R. Laurien, <u>J. Crystal Growth</u> <u>52</u>, 506 (1981).

11. Rinaldi, S., and F. Licci, <u>IEEE Trans. on Magnetics</u> <u>MAG-20(5)</u>, 1267 (1984).

6. ACKNOWLEDGMENTS

END

10-87

DTIC